Computational Studies on Ring-Opening and Closure: Origins of Selectivity and Catalysis

---

Thesis submitted for the

Degree of Doctor of Philosophy

Department of Chemistry

Trinity 2016

Robert Simion

University College

University of Oxford

Abstract

This thesis describes the application of computational chemistry to understand the origins of the regioselectivity and stereoselectivity in reactions involving the opening and formation of cyclic species. In particular, we have used transition state modeling to gain quantitative insight into an area of organic chemistry where previous understanding has been heavily unfluenced by empirical observations. Our work provides a basis to understand regioselective ring-opening of epoxides in systems controlled by subtrate- or solvent effects. We have also studied enantioselective catalysis using phosphoric acids, which promote enol ether spirocyclizations and the desymmetrization of meso epoxides and aziridines.

In Chapter 2 we investigate the unusual 6-*endo*-*tet* selectivity of epoxide-opening cyclizations, which form a tetrahydropyran motif found in several marine natural products. Through DFT calculations we have established the stereoelectronic effect of neighboring groups in weakening the adjacent C-O bond, which directs the nucleophilic attack at this position. We also discover that the role of a template provides a thermodynamic bias towards the pyran product, but that it also influences charge separation in the competing transition state structures. The 5-*exo*-*tet* pathway suffers from greater charge separation, and entropically unfavorable solvation effects.

In Chapters 3 and 4 we turn to enantioselective catalysis with chiral phosphoric acids. Here we investigated the origins of enantioselective enol ether spiroketalization. We have established that selectivity arises in a concerted, but asynchronous step in which the enol ether is protonated, and the developing oxonium is quickly intercepted. The computations are able to account for the sense and level of enantioselectivity based on this mechanistic model. We then focus on the desymmetrization of meso epoxide and aziridines using the same class of catalyst: again a bifunctional mechanism emerges from our studies in which ring opening and nucleophilic attack are promoted by the phosporic acid in a single step. A model for enantioselectivity has been developed to account for the sense of selectivity for this synthetic transformation.

Contents

Chapter 3: Stereoselective Spiroketalization of Enol Ethers

Chapter 4: Chiral Phosphoric Acid Mediated Desymmetrization of Meso Compounds

Acknowledgements

My first dedication is to my parents and brother who have supported me through all my ups and downs. My second dedication is to Professor David Baker who has supported me professionally and personally from the first day that I stepped in his lab so many years ago.

I would like to thank Professor Robert Paton for his support in returning to Oxford and the mentorship during my D.Phil.

Last but certainty least I would like to thank my colleagues over the years who names may be redacted. You have provided endless enjoyment and I wish you - Kelvin, Wilian, Sami, Peter, Conor, Matt, and Costyl - all the best.

Glossary of abbreviations and acronyms

Å	angstrom(s), 10^{-10} m
Ac	acetyl, $COCH_3$
AcOH	acetic acid, CH_3COOH
ACDC	Asymmetric Counteranion-Directed Catalysis
An	3,3'-Bis(9-anthracenyl)-1-1'-binaphthyl-2,2'-diyl
ANO	Anomeric
AO	Atomic orbital
Ar	aromatic group
Atm	atmospheres (1 atm = 1.01 x 10^5 Pascal)
au	atomic units
B2PLYP	A double hybrid DFT with a Grimme Expansion on B3LYP exchange correlation
B3LYP	hybrid density functional incorporating Becke exchange with Lee-Yang-Parr correlation
BDE	bond dissociation energy
cat.	Catalytic
CF_3	Tri-Fluoromethyl group, $-CF_3$
CH	Curtin-Hammett Postulate
Cl	Chloride Group, -Cl
CPA	Chiral Phosphoric Acid
CPCM	conductor-like polarizable continuum model
CS	Charge Seperation
DFT	density functional theory
DZ	double zeta
equiv.	equivalents

E.E	Enatiomeric Excess
E.S	Enatioselectivity
ESP	electrostatic potential map
GGA	generalised gradient approximation
GS	Ground State (minimized structure)
GTO	Gaussian-type orbital
HCl	Hydro-Chloric Acid
HF	Hartree-Fock
HOMO	Highest Occupied Molecular Orbital
IRC	intrinsic reaction coordinate
K	Kelvin
kcal mol^{-1}	kilocalorie per mole
KIE	kinetic isotope effect
LDA	local density approximation
LFER	Linear Free Energy Relationships
LUMO	Lowest Unoccupied Molecular Orbital
FMO	Frontier Molecular Orbital
M06-2X	Minnesota 06 density functional of Truhlar
MD	Molecular Dynamics
Me	methyl group, $-CH_3$
MM	Molecular Mechanics
MP2	Møller-Plesset second order perturbation theory
NA	Non-anomeric
NAC	Near Attack Conformation
NBO	natural bond orbital

NMR	Nuclear Magnetic Resonance
OMe	methoxy group, -OCH_3
ONIOM	Our own N-layered Integrated molecular Orbital and molecular Mechanics
OBz	Benzoic, $C_6H_5COO^-$
PCM	polarizable continuum model
PES	potential energy surface
Ph	phenyl group, -C_6H_5
QM	Quantum Mechanical
QM/MM	Quantum Mechanical, Molecular Mechanics Hybrid
RDS	Rate determining State
RT	room temperature
SBz	Thiolbenzoic, $C_6H_5COS^-$
SKIE	Solvent Kinetic Isotope Effects
S_Ni	Substitution Nucleophilic Internal
S_n2	Substitution Nucleophilic Substitution
Sub	Substrate
SCRF	self-consistent reaction field polarizable continuum model
STO	Slater-type orbital
TFA	triflouroacetic acid, CF_3COOH
tet.	Tetrahedral
THF	Tetrahydrofuran
THP	Tetrahydropyran
Tol	Toulene, C_7H_8
TRIP	3,3'-Bis(2,4,6-triisopropylphenyl)-1,1'-binaphthyl-2,2'-diyl

TS	transition state (first order saddle point)
TST	transition state theory
TZVP	triple zeta valence polarized
UFF	Universal Force Field
ωB97XD	dispersion corrected density functional of Head-Gordon
ZPE	Zero-point (vibrational) energy

Author's declaration

The thesis is an account of work carried out by the author in the Department of Chemistry, University of Oxford under the supervision of Dr Robert S. Paton. No part of this thesis has previously been submitted for a degree in this University or elsewhere. The work of other authors has been freely drawn and is duly acknowledged in the text. A list of references is given at the end of each chapter.

Doctoral work has been featured externally as follows:

Cortopassi, W. E.; **Simion, R.;** Hornsby, C. E.; Costa Franca, T. C.; Paton, R. S. "Dioxygen binding in the active site of histone demethylase JMJD2A and the role of protein environment*" Chem. Eur. J.* **2015**, *21*, 18983-18992.

Tang, B.; **Simion, R.;** Paton, R. S. "Thermal and Photochemical Mechanisms for Cyclobutane Formation in Bielschowskysin Biosynthesis*" Synlett,* **2015**, *26*, 501-507.

Robert Simion

Chapter 1. Introduction

1.1 Computational Methods

1.1.1 An Introduction

Understanding even the simplest phenomena relies on a mixture of empirical arguments, extrapolating from the conclusions of past observations, and theoretical models. Chemical theories are no different. The majority of our theories, many still in everyday use, have been based on empirical observations made in the laboratory. These experiments are sometimes performed using a small sample size (e.g. of substrates) in a controlled environment, which can limit the application of the resulting interpretation to applications outside of the immediate area for which it has been developed. Computation provides us with the ability to generate theoretical models from a bottom-up understanding that may be applied to make predictions of the results of laboratory experiments.[1] Additionally, the means to preform simulations allows the possibility for researchers to generate predictions on a timescale that is faster than the corresponding experiment. Arguably, the growth of computational chemistry has therefore added to chemists' ability to expand the scope of our predictions, and increasing the reliability of our conclusions.

In summarizing the status of quantum mechanics at the end of the 1920s, Dirac said the following, "*the underlying physical laws necessary for the mathematical theory of a large part of physics and the whole of chemistry are thus completely known, and the difficulty is only that the exact application of these laws leads to equations much too complicated to be soluble.*"[2] The same consideration remains today, since an exact quantum mechanical description of all but the simplest systems remains out of reach and so we must decide upon the optimal, necessarily approximate, approach for the chemical system of interest. Here one must also acknowledge the compromise between accuracy and speed that underlies all computational methods.[3] For example, density functional theory is applicable to the modeling of synthetic catalysts, but this would be too expensive to study the dynamics of lipid membrane movements, requiring more approximate methods such as classical molecular mechanics.[4]

In this thesis I describe studies on the mechanisms and selectivities of catalytic organic reactions. This requires an understanding of transition state structure, since this dictates the stereo-determining event and is essential to developed a model for the origins of selectivity. In order to do so, a quantum chemical treatment of the reacting systems is necessary since classical methods do not describe bond formation or cleavage. Nevertheless, we have incorporated different levels of theory in our studies, including combinations of quantum and classical theories in order to explore these mechanisms computationally on relevant time scales. Our application of computation has been geared towards understanding how the myriad interactions between the intermediates, environment and kinetics influence the observed reaction outcome.

1.1.2 Electronic Structure Theory

The advent of quantum chemistry started with the simple solving of the single electron wave-function but has birthed a revolution in nearly all fields of applied science to date. The computational approaches that we utilize to date are built on approximating work performed in the 1920's. The time-independent, non-relativistic formulation of the Schrödinger equation for the one electron wave function is shown in equation 1.[5]

$$H\psi=E\psi \qquad \textbf{(eqn 1)}$$

In this equation H, represents the Hamiltonian which contains terms for the kinetic energy of the electrons, nucleus, and interactions. The energy of the system is dependent on the probability of the electron density at set distance away.

The first step towards computation of multi-electron systems was in the development of a method to solve a many-body wave function. This work was initiated by D. R. Hartree, who developed a method to solve a many electron state through multiple iterations of the one-electron system.[5] Fortuitously, at the same time the Born-Oppenheimer (BO) approximation was developed. The BO-approximation allows one to assume that the movement of electrons is much faster than that of the nucleus due their difference in mass.[6] On the timescale of electron movement the nucleus is

essentially motionless (often referred to as "clamped"), which enables complete separation of electronic and nuclear wave functions. This approximation allowed Hartree to approximate the energy of the electrons in the environment of classically described nuclei. Even though this was a significant step forward, the early approach failed to take into account electron-electron repulsion, since the individual electron wave functions were assumed to be completely independent. The equation was re-written to include an effective field (V^{eff}) for this electronic repulsion. J. C. Fock realized, however, that the Pauli exclusion principle was not satisfied by the resulting multi-electronic wave function since there was not a change in sign upon the interchange of two electronic coordinates (also referred to as the antisymmetry principle).[6] Formulation of the wave function as a Slater determinant rather than as the product of single-electron wave functions solved this problem and is the approach used today to generate an antisymmetric wavefunction from one-electron orbitals (equation 2).

$$\Psi(x_1, x_2, \ldots x_N) = \frac{1}{\sqrt{N!}} \begin{vmatrix} \chi_1(x_1) & \cdots & \chi_N(x_1) \\ \vdots & \ddots & \vdots \\ \chi_1(x_N) & \cdots & \chi_N(x_N) \end{vmatrix} \quad \textbf{(eqn 2)}$$

Application of the Schrodinger equation is used to obtain the energy associated with a given wave function. For molecules the wave function is constructed from the atomic orbitals centered on each of the constituent atoms. The Hartree-Fock-Roothaan (HFR) procedure developed the concept of a *basis set* which is the set of mathematical functions centered on each of the atoms which add up to create these atomic orbitals, that is now ubiquitous in modern quantum computational approaches. The type of function chosen by HFR to describe the atomic orbitals was a Slater-type orbital (STO). The STO orbital was utilized, as its shape is identical to those one-electron orbitals obtained from application of the Schrödinger equation to the hydrogen atom. This form is e^{-r} ., where r is the distance away from the nucleus. The STO is a faithful representation of the shape of an isolated atomic orbital, however, computationally it imposes significant computational resources associated with integration. A more efficient approach has been found to decrease the computational burden of the calculations, using a *Gaussian*-type orbital (GTO of the form e^{-r^2}. This was developed

by Pople, and although more efficient has the obvious problem that the shape is no longer faithful to the hydrogenic orbitals: the atomic orbitals decay much faster away from the nucleus, and has the wrong shape close to the nucleus.[6] To overcome this, the utilization of multiple Gaussian type orbitals (GTO) to describe an atomic orbital was introduced. The summation of several GTOs results in a basis function which closely resembles the correct shape (**Figure 1**).

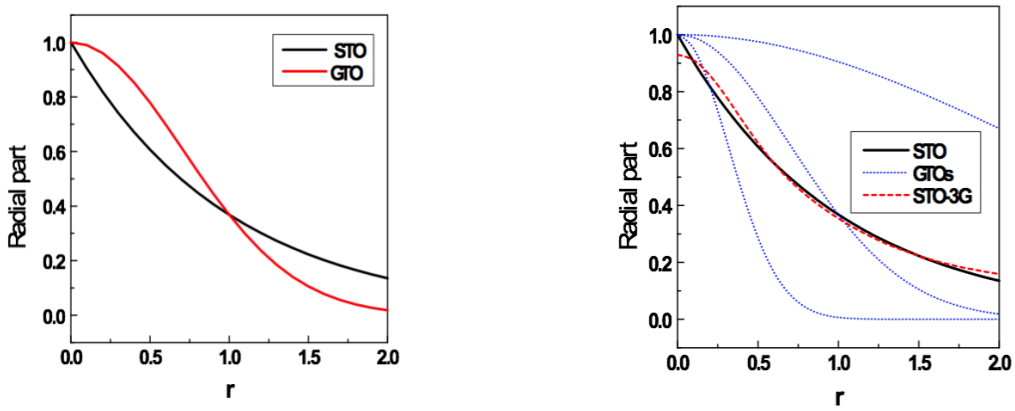

Figure 1. Left-hand side: comparison of the radial parts of Slater (STO) and Gaussian orbitals. Right-hand side: contraction of three GTOs (blue) results in the red dashed curve (STO-3G), which more closely resembles the radial-decay of the STO.

This has been subsequently refined to the split-valence basis sets we use today. Here, several Gaussian exponents are used in the description of the valence orbitals, and the mixture is optimized in the calculation. This enables greater flexibility in the description of the valence shell, which undergoes changes upon chemical bonding. In general more basis functions provide greater flexibility to describe the molecular wave function although at a certain point properties such as geometries and energies are said to "converge" such that the addition of more basis functions has little effect. One advantage of density functional theory is that this point is reached sooner than for alternative quantum chemical methods.

1.1.3 Density Functional Theory

Hartree-Fock (HF) embodies wave function theory (WFT), where the central idea is that the wavefunction gives information about the overall energy. Even with the developments to consider electron-electron interactions, the treatment of correlation remains problematic for HF as the assumption of an average potential falsely implies that there is no dynamic avoidance between electrons. Therefore, considerable attention has been paid to an alternative approach to WFT, in the form of density functional theory (DFT), developed by Kohn, Hohenberg, and Sham (eqn 3)[7]. The Kohn-Sham equation to solve for the Energy of the density interactions of the model. T_e is the kinetic energy, V_{ne} is the nuclear-electronic potential, V_{ee} is the electron-electron potential, and E_{xc} is the electronic correlation. The nuance that they had was that if the compound was not excited out of its ground state then the system could be uniquely described by the distribution of the electron density.

$$E[\rho(r)] = T_e[\rho(r)] + V_{ne}[\rho(r)] + V_{ee}[\rho(r)] + E_{xc}[\rho(r)] \quad \textbf{(eqn 3)}$$

In principle, DFT has reduced the problem of a system of interacting electrons to one that just considers the resulting density. There is, however, an important distinction between DFT and *ab initio* approaches such as HF. The energy associated with a given electronic density is calculated using the equation displayed in equation 3. The last term in equation 3, is the so-called exchange-correlation functional, which contains contributions from the kinetic energy and electron-electron interactions associated with the electron density. Unfortunately, the form of the universal functional is unknown and so many approximate functionals have been developed to account for this energy. This unknown has allowed many researchers over time to introduce their own functional to address this issue, which vary in both functional form and the parameters used. The development of new functionals is performed through comparison with reference data and so could be said to semi-empirical. The hierarchy of this evolution has been more commonly referred to by Perdew as Jacob's Ladder of density functionals (**Figure 2**).[8]

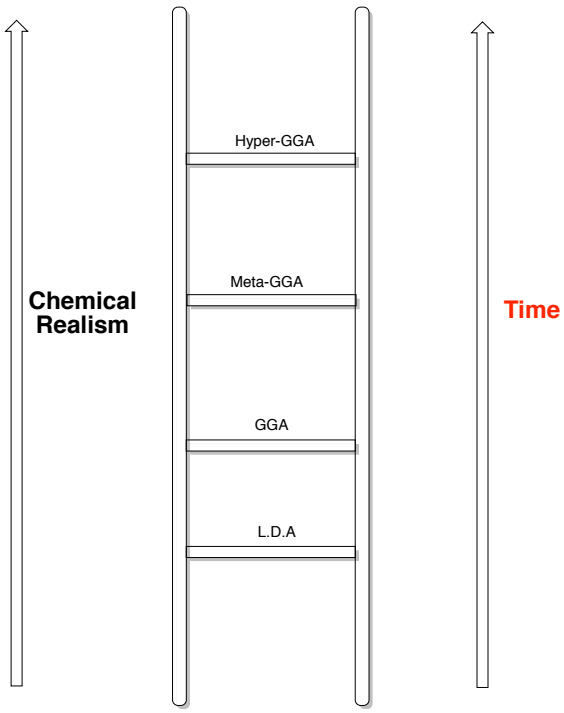

Figure 2: So-called *Jacob's Ladder* as proposed by Perdew describes the proximity of the DFT method to an ideal description of electron correlation (the lowest rung is the furthest away).

The initial descriptions used for exchange-correlation functionals for were based on the local density approximation (LDA) which assumes the exchange-correlation energy could be connected to the value of the density of a uniform electron gas (**equation 4**).[9]

$$E_{xc}[\rho(r)] = E_x[\rho(r)] + E_c[\rho(r)] \quad \text{where} \quad E_{x(LDA)} = -C_x p^{1/3} \qquad \textbf{(eqn 4)}$$

This approach approximates a uniform electronic density, which means an inhomogeneous electronic density (as is the case for molecules!) will result in erroneous conclusions. To overcome this, the generalized gradient approximation (GGA) approach was developed which introduces an enhancement factor to account for changes in electron density and improves the accuracy in the description of molecular systems.[10] More modern techniques, have extended to further corrections due to the changing electron density as in meta-GGA and hyper-GGA functionals.[11] Additionally,

it has been found that incorporation of HF exchange energies improves the results of pure DFT calculations that has led to the development of hybrid functionals. Each of these conceptual developments involves one step up Jacob's ladder towards what Perdew termed the "heaven of chemical accuracy". Typically this is considered to be within 1 kcal/mol of experimental values.

Implementation of the Kohn-Hohenberg equation to molecular systems requires a choice of functional that allows us to calculate the total energy of the system. In this thesis we discuss three main methods (i.e. density functionals). Firstly, the B3LYP functional utilizes the hybrid-GGA approach.[12] The B3LYP functional is perhaps the most utilized functional of all time, and was developed by Axel Becke to incorporate Hartree-Fock exchange (20%) and a mixture of local and non-local DFT approximations to treat exchange and correlation, where the amounts were optimized to reproduce the atomization energies of a range of small organic molecules.

$$E_{xc}^{B3LYP} = (1-a)E_x^{LSDA} + aE_x^{HF} + b\Delta E_x^B + (1-c)E_c^{LSDA} + cE_c^{LYP} \qquad \textbf{(eqn 5)}$$

The electronic correlation is treated in B3LYP using the exchange-correlation functional (**equation 5)** above.[13] As we are able to see, this correlation structure imples a corrective nature most similar to equations found in semi-empirical cases. The values of *a*, *b* and *c* are adjustable parameters, which were set by Becke through comparison with reference data obtained for small organic molecules. This equation highlights the difference between a genuinely *ab initio* (literally, "from the beginning") computational treatment and density functional theory: namely, that many functionals include terms whose value are not deduced from theory but adjusted to reproduce known quantities or parameters. The success of DFT indicates that this approach is flexible enough to describe molecules outside of the reference set initially considered, however, different functionals have used different training data and so can perform better or worse depending upon the chemical application.

The large number of studies utilizing the B3LYP functional are a testament to the success of this approach, however, more recently problems have emerged in the description of "long-range" interactions. This is a problem associated with the description of electron correlation at a distance. This results in inaccuracies while calculating the interaction between, for example, aromatic systems or so-called hydrophobic interactions. To help correct this error many groups have introduced *ad hoc* corrections, based on empirical models for the missing dispersion energy. These modifications can either be introduced implicitly to the functional as is the case for wB97XD, or alternatively as an explicit correction to any functional, as is the case for the D3-correction developed by Grimme.[14,15] In this approach, additive, attractive term is used to compensate for the failure of DFT to adequately treat dispersion interactions. As shown in Figure 3, for systems such as the benzene-benzene dimer this correction is essential to ensure the correct description of a stable energy minimum, which is absent without the D3-correction.

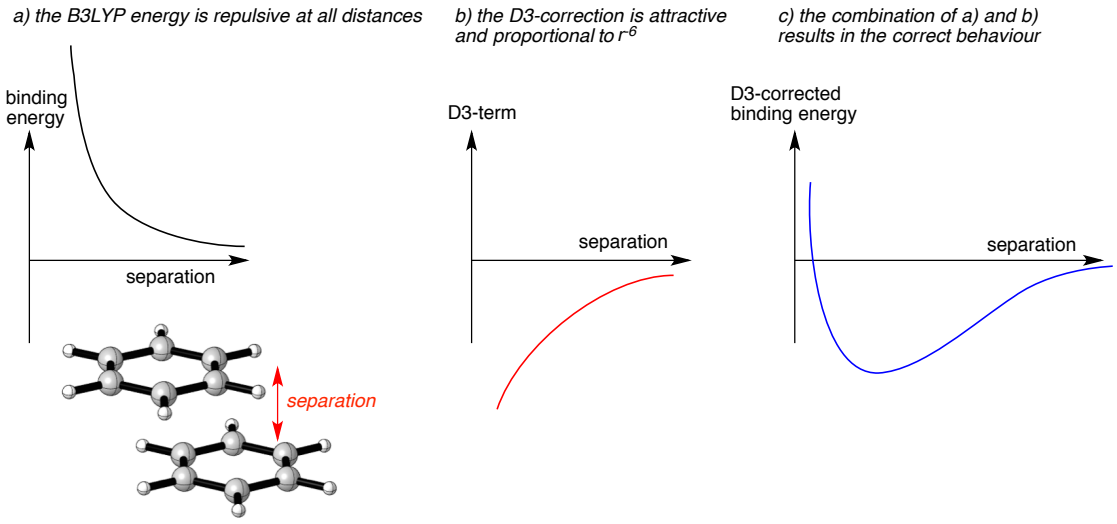

Figure 3. Overview of the D3-correction for dispersion interactions applied to the benzene-benzene dimer.

The most utilized group of density functionals in this thesis are from the Minnesota (M06) family, developed by Truhlar in 2006.[16] These are parameterized functionals that calculate the kinetic energy of the electron density to help correct the exchange

correlation energy. The M06-2X variant includes a mixture of HF exchange energy that has been particularly useful for organic and main-group chemistry. In some cases we utilized the M06-L method, a pure DFT method which does not have any HF correction and increases the speed of the calculations relative to the M06-2X method. While these functionals have shown high accuracies for their training data in the literature, the extensive parameterization is potentially disadvantageous since it may imply poorer performance for chemical scenarios outside of the training data. For the reactions that we investigated we either found literature precedence or performed computational benchmarking studies to verify results.

1.1.4 The QM/MM Approach: ONIOM

A critical problem found with quantum mechanical approaches is the non-linear increase of computational cost (time) with the size of the molecule (Table 1). These scaling factors make calculations for molecules with hundreds of atoms prohibitively expensive. In particular, geometry optimizations require repeated evaluation of the energy and its gradient such that the application of QM approaches is restricted to a final energy calculation after optimization with a more approximate level of theory.

Method	**Scale Factor, N^x**
Molecular Mechanics	N_{atoms}^2
Density Functional Theory	N_{basis}^3
Hartree-Fock	N_{basis}^4
Moller-Plesset Perturbation Theory	N_{basis}^5
Couple Cluster with Singles and Doubles	N_{basis}^6

Table 1. Computational scaling-factors for each method based on system size.

QM approaches are necessary to describe changes in chemical bonding for which classical models fail badly. On the other hand, for regions of molecules that have a predominantly steric role during a reaction it may be possible to use a more

approximate description that significantly reduces the computational cost. For atoms whose bonds are not being significantly distorted away from idealized values, molecular mechanics (MM) or other low-level theories can be applied to describe molecular structures and energies. The combination of a QM treatment of a reacting center, surrounded by an MM treatment of the non-participating functional groups is known as a hybrid QM/MM approach. In particular, a popular implementation of such an approach has been implemented in the Gaussian package, called *ONIOM*, which stands for **O**ur own **N**-layered **I**ntegrated molecular **O**rbital and molecular **M**echanics.[17] This has been developed by Morokuma and co-workers and enables DFT descriptions of transition states, where the outer regions are treated by lower level theories. The ONIOM approach has some restrictions, but has thus far shown to be accurate in our hands as well as others (**Figure 4**)[18]. The examples below have treated bond formation or cleavage with DFT calculations, while the catalyst "backbone" in each case, the region expected to contribute conformational and steric effects, but not explicitly participate in the chemical reaction itself, was described by MM calculations.

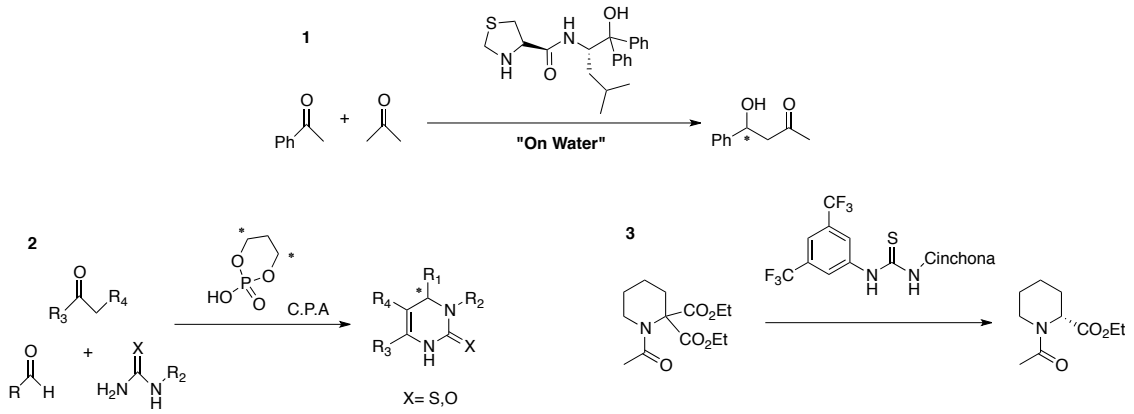

Figure 4. Catalytic reactions that have been successfuly treated using the ONIOM methodology. Reaction 1 is an explicitly-solvated aldol reaction

In the implementation of QM/MM, a classical description is used to describe parts of the molecule. Molecular mechanics is perhaps the most widely applied technique in computational (bio)chemistry since it is used almost exclusively to study biomacromolecules. The central concept is that of chemical bonds as a harmonic

springs linking hard spherical atoms, **Figure 5** and **equation 5**. The lengths and force-constants of these springs are parameterized, and have been developed from experimental X-ray structures, spectroscopic observations of e.g. stretching frequencies and other types of calculation. Many different descriptions are available depending on both the sophistication of the force field and the parameters used.[19]

$$E = \frac{1}{2}k(x - x_0)^2 \qquad \textbf{(eqn 5)}$$

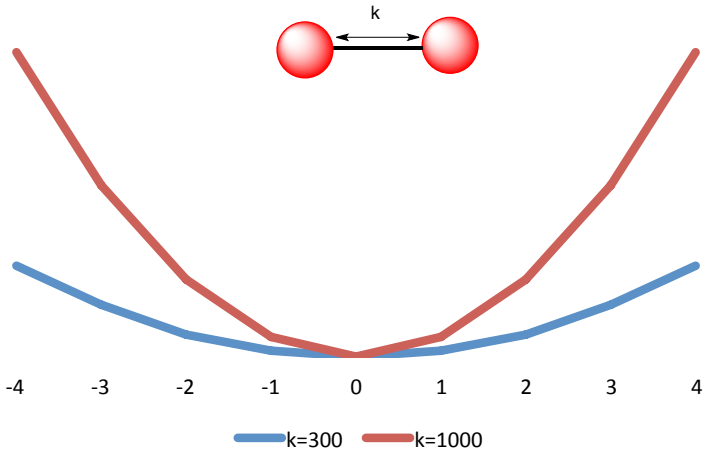

Figure 5. Represenation of a harmonic oscillator used to model covalent bonds in molecular mechanics. The force constant, *k*, affects the stiffness and hence the potential energy surface. Similar expressions are used for angle-bending.

One area of computational chemistry where ONIOM calculations have featured heavily has been in the modeling of catalysis with chiral phosphoric acids (CPAs). These systems are well-suited to such an approach, since the catalytic role associated with hydrogen bond donation or acceptance can be captured well by DFT calculations and the stereochemical and steric role of the chiral BINOL-backbone can be described by force field parameters since there are no changes in bonding for this region of the catalyst. Simón and Goodman have published several investigations using the ONIOM methodology to study such systems, where optimizations employed the B3LYP functional and the United-atom Force Field (UFF) was utilized for the backbone (**Figure 6**).[20] In fact, the torsional potential about the central C-C bond in the BINOL

backbone was found to be described more accurately by UFF than other, more expensive methods making this force field the most suitable for these catalysts. Additionally, force fields include explicit terms to describe steric and Van der Waals interactions so that these methods may be more accurate than uncorrected DFT approaches for the study of intermolecular or intramolecular interactions which play a role in asymmetric catalysis.[21]

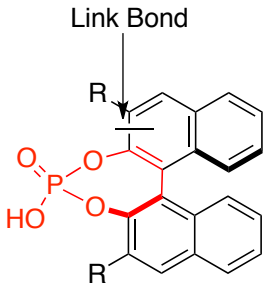

Figure 6: The CPA is treated with a DFT method such as M062x in the Red region while the lower level (Black) is treated with UFF. The Link-Bond is between the sp^2 carbons.

1.2 Translating and Transcribing Computational Data

1.2.1 Kinetic Methods

Most of the data that computational chemists have at their disposal are the "macroscopic" experimental outcomes from reactions. For complex reaction mechanisms, it may not be possible to obtain information about each elementary step directly, if at all. On the other hand, computational models deal with these chemical steps directly. Without a means to translate our computational information into a form that can be compared against these experimental results, such as measured rates or selectivities, a disconnect remains between the two approaches.

Some of the more commonly used ways of comparing computation directly with experiment are kinetic models, and within those schemes the application of concepts such as Curtin-Hammett (CH) and King-Altman (KA). The King-Altman approach is a graphical approach to kinetic analysis where the observed kinetics are a combination of

multiple pathways with one dominating at different time points (**Figure 7**).[22] The KA method allows one to solve the time dependent kinetic representation of e.g. an enzymatic reaction with steady state approaches (Michaelis-Menten).

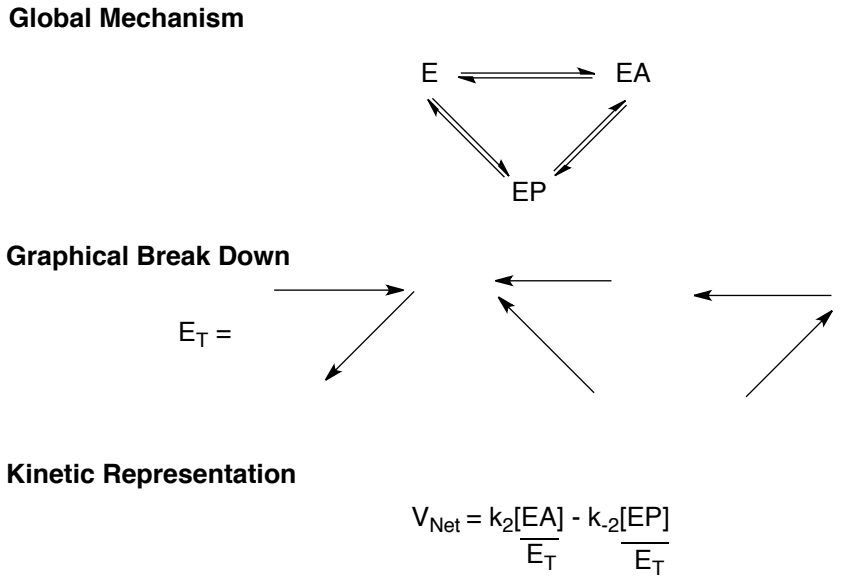

Figure 7. The King-Altman technique applied to a simple catalyst relationship. We highlight how we can go from a mechanism not under-steady state to a kinetic representation.

Shaik and Kozuch (SK) have adapted the KA approach computationally into the so-called activation-span model. This allows the computational chemist to model the non-rapid equilibrium kinetics which may occur during catalysis.[23] In their model only one pathway is considered and the population of an intermediate, at the rate-determining step, is weighted by the previous equilibria. As shown by **Figure 8**, if we are investigating a competitive state then equation would simplify into the un-modified CH equation.

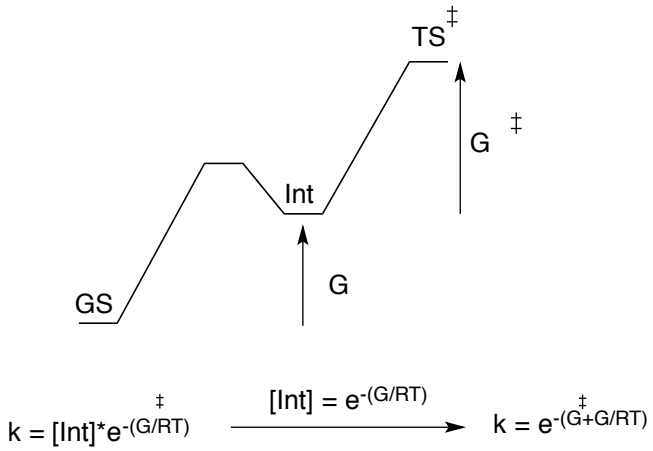

Figure 8. The uptake and modification of the King-Altman technique applied to a simple chemical catalyst analysis. The initial form of the kinetic equation is the transition state theory weighted for the population of the intermediate.

In the bulk of our computational studies of catalysis we have compared the CH and SK (activation-span)-type approach to one another to determine the likely behavior of the catalyst in the experimental work. This approach allows us to investigate the extremes of catalysis to determine which behavior is the most probably. Both require the calculation of rate-constants, which we obtain using Transition State Theory (TST). In TST, there is an assumed quasi-equilibrium between the reactant complex and transition state leading to the Eyring expression in terms of the free energy difference between the two species (**Figure 8**).[24] From a computational perspective the computation of the activation free energy barrier requires the evaluation of the energy difference and the entropy difference, which depends on translational, rotational and vibrational factors. The vibrations are obtained from a computation of the harmonic frequencies.

A transition structure (TS) correspond to saddle points on the potential energy surface (PES), and is computationally characterize by the presence of one imaginary frequency, which corresponds to the reaction coordinate. This arises from the negative force constant in the diagonalized Hessian matrix – i.e. the nature of the stationary point along this direction is a maximum. There can be of course many points scattered across a potential energy surface that would satisfy this requirement, for example associated

with the rotation of small groups. To ensure that the transition state located corresponds to the correct transition point we analyze both real and imaginary force constants so we can visualize the bond stretching. If the bond stretching mimics the reaction trajectory that we expect then we can conclude that the transition state is appropriate (**Figure 9**).

Additionally, energy minimizations in each direction can be carried out to confirm that the TS evolves into the expected reactants and products. This can be done in a relatively quick way simply using geometry optimizations starting from structures displaced along the imaginary frequency, as proposed by Goodman's Quick Reaction Coordinate (QRC) approach. Alternatively, and more formally, the TS can be subjected to an Intrinsic Reaction Coordinate (IRC) calculation which is more demanding, again leading to the reactants and products associated with the input TS structure.[25]

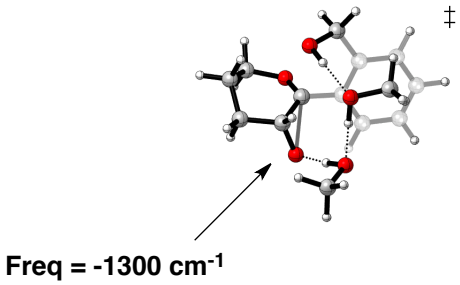

Figure 9. An example of an optimized TS with a single imaginary frequency, often indicated by a negative value, which corresponds to epoxide opening.

1.2.3 Reactivity

The reactions investigated in this thesis are generally considered to be kinetically controlled reactions, as compared to thermodynamic control, which essentially means that they are irreversible. The impact of kinetic control is such that the reaction with the lowest activation barrier will usually lead to the dominant product. Thus factors that preferentially stabilize the transition state for a given pathway will enable a more selective reaction. In turn, an understanding of transition state structure and electronic characteristics enables these effects to be reasoned.

Approaches to understanding reactivity, as outlined above, differ between chemists and biologists. In chemistry, a popular lens through which to understand the favorability of a given transition state is by thinking about the "intrinsic barrier" by Marcus.[26] This originally described the unfavorable reorganization (of reactants and surroundings) involved in electron-transfer, in a way which removed the effect of thermodynamics. In the context of organic reaction mechanisms, the intrinsic barrier could be thought of similiarly as an unfavorable reorganization term, to describe the resistance of a reactant(s) to distort both geometry and electronically to achieve the requirements of the transition state. Catalysts have been argued to promote such stabilization through pre-organization of the environment around the compound.[26] A limitation of Marcus theory is the extensive and controlled data required to calculate the intrinsic barrier for a reaction.[26]

In biology, a wealth of information has come from the X-ray structures of enzymes, nature's catalyst molecules. In the initial days of enzymology one of the prevailing theories of rate enhancement by enzymes was the hypothesis of stabilization of reactants in a near attack conformation. The Near Attack Conformation (NAC) theory was that by stabilizing the compound in a conformation that showed productive frontier orbital overlap the enzyme is able to stabilize the transition state to a greater extent then the ground state. As highlighted in recent years this approach has shown limited success in predicting the activity of catalysts *in silico*. It is the author's belief that a source of error for this approach is the NAC's inability to capture the whole origin of catalysis.[27]

1.2.2 Molecular Dynamics Simulations

As mentioned previously, there are limitations in computational chemistry associated with the standard tools available to us;

- static models are routinely used to interpret the behaviour of dynamic systems, which may not be in steady-state.

- chemical intuiton and other biases may miss relevant features of the system.

The images that we generate are the ideal structures that we can use as a base to make predictions from. In reality small rotations of angles or dihedrals would result in slight alterations of the geometry that could skew the approach trajectory. These geometric changes are thermally accessible in the ground state and can be carried over into the transition state. To probe this many researchers have developed different techniques, but the underlying factor behind the majority is the utilization of Molecular Dynamic (MD) simulations that allow follow the trajectory of a system by numerically solving Newton's equations of motion [28] The purpose of MD is to find the lowest energy conformation for a multi-body system where the energy function for a given state is broken down into intra and intermolecular terms. In Monte-Carlo simulations the simulations pick random conformations and calculate the energy of the structure (**Figure 9**).[29]

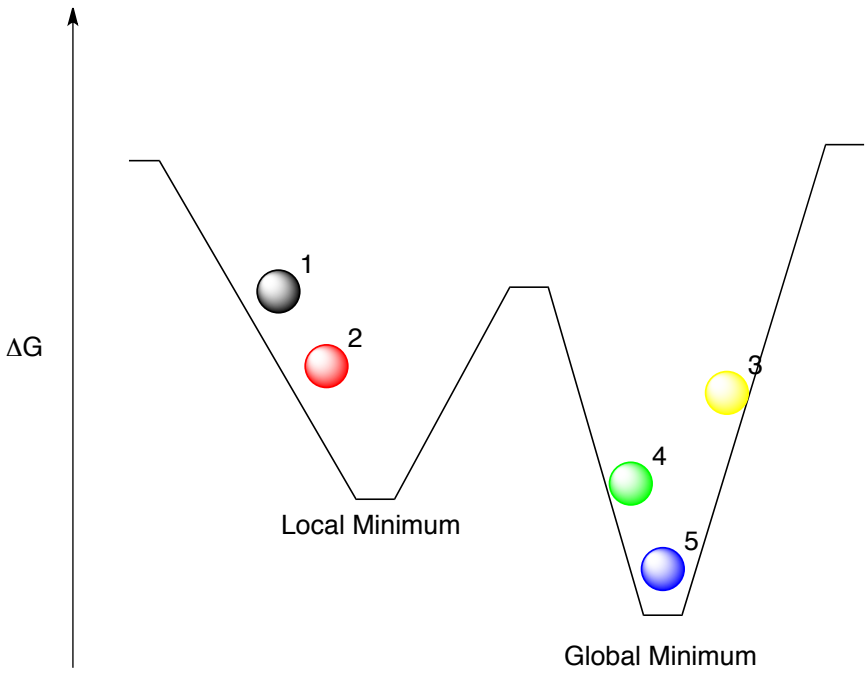

Figure 9. Monte-Carlo approach which each discrete ball represents a novel conformation of the compound of interest. The simulation would terminate when it reaches position 5.

This is then compared to the states prior to estimate the relative change in stability. This process is repeated until a global minimum is found. An inherent problem of this approach is that structures can be trapped in local minimum. To force the simulation out of the local minimum, steered molecular dynamics can be integrated in which will apply extensive force to the simulation to force the structure out of the local minimum (**Figure 10**).

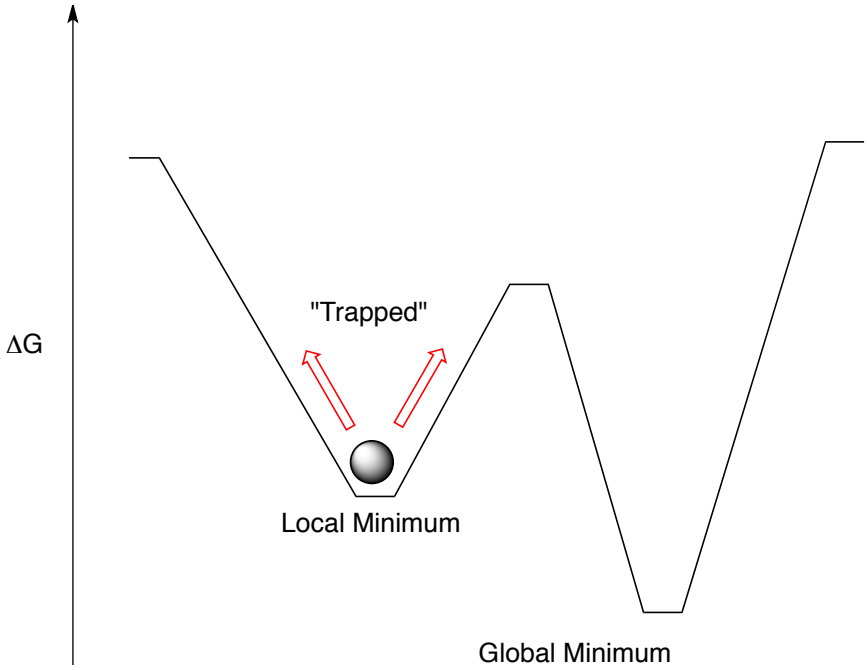

Figure 10. Energy Profile showing how a molecule (circle) can be trapped in a local minimum if the step-size is to small.

Traditional MD is often utilized for compounds that have real vibrational frequencies, which has prevented its application to transition states which display one imaginary frequency. In essence, the pathway to a TS is a "rare event", which in the absence of a baising force would occur almost never in the MD simulation of a single molecule. Several methods have been developed though to get around this problem by forcing the system to adopt non-natural bonding distances. The most utilized technique is so-called *umbrella sampling*. The umbrella simulation takes its name from the method by which the compound is pulled in an interactive fashion to the transition state allowing the system to come to equilibrium before it is moved again (**Figure 11**).[30] Due to the

computational demands of such calculations, it is still necessary to adopt a fairly "low-level" description of the chemical system. So while sampling is considered, the quality of the underlying QM description of the reacting system also suffers to the extent that activation barriers can be several tens of kcal/mol in error with respect to experiment.

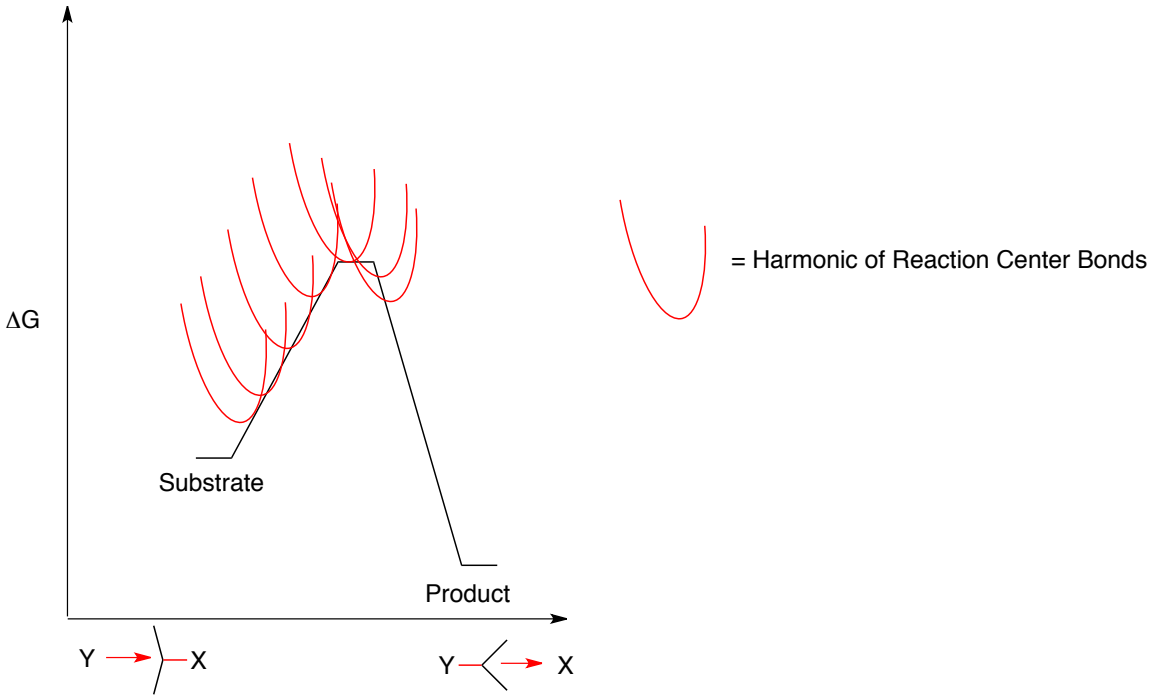

Figure 11. The representation of the Umbrella technique where the reaction coordinate is pulled along the reaction profile to help find and simulate the transition state barrier.

As the Umbrella sampling method is in its infancy the true impact that it will have on higher-level calculations is not yet fully understood. As technology changes though we may find that MD simulations will improve the accuracy and robustness of the computational methods that have been developed over the last 60 years. In our work we investigated how solvent influences the potential energy surface to help modulate the inherent properties of the reaction to produce the observed outcome. With this knowledge we then applied this information to the catalytic reactions investigate the mechanism of the catalyst and subsequently determine how kinetics modulates the modulation of the chemistry to produce the observed outcome.

1.3 Outline of the thesis chapters

In this thesis I focus on the nucleophilic attack of reactive intermediates: chapter 2 concerns the trajectory and regioselectivity of epoxide-opening cyclizations, while chapters 3 and 4 study the mechanism and enantioselectivity of spiroacetalization and of meso-epoxide opening. The reactions that we selected to investigate all show an unusal relationship with their environment. In the case of Chapter 2 the impact of the solvation shell has some investigation experimentally but very limited conclusions have been drawn to help explain the shifting in selectivity as the template is altered. In Chapter 3 and 4 the CPA mechanism is not fully understood nor how the catalyst interacts with the substrates strong stereo-electronic effects to help control the reaction.

In Chapter 2 we utilize DFT calculations to investigate experimental observations made upon the regioselectivity of epoxide-opening cyclizations. It has been shown that water can promote the formal 6-*endo*-tet opening, also referred to as the *fused* pathway, to form a tetrahydropyran. This is in contrast to results obtained in organic solvents (Figure 12). We have been able to create explicit solvent models (also known as cluster models) to understand the impact of water on the reaction course. By generating this model information we are able to explore the reaction trajectory which we utilized to explain the observed behavior of the 6-*endo*-tet reaction. We have extended these investigations of the importance of nucleophilic trajectory to consider classical examples of chemical approaches for regioselective epoxide-opening reactions.

In Chapter 3 we utilized DFT, ONIOM, and MD simulation to investigate the C.P.A promoted enantioselective spiroketalization. The chiral phosphate can classically act as either a general or specific acid catalyst. Since there has been no kinetic investigation performed on this reaction we investigated the mechanism by understanding how the two classic methods, acid and solvent, controlled the spiroketalization. From these studies we were able to predict the mechanism by which the C.P.A would reacted and explore the impact of this mechanism on the enantioselective synthesis of the spiroketals (Figure 13).

In Chapter 4 we again utilized the ONIOM computational technique to be able to investigate the desymmerization of meso-epoxides and azidiners by C.P.A with different acids. As our study of the system progressed we found that the conformations that the acids could adopt resulted in significant deviations from what our models would have initial suggested. With this study we are able to highlight the impact the limited specific interactions the C.P.A makes with the substrate and the subsequent result on the number of binding modes of the activated complex can adopt. (Figure 13).

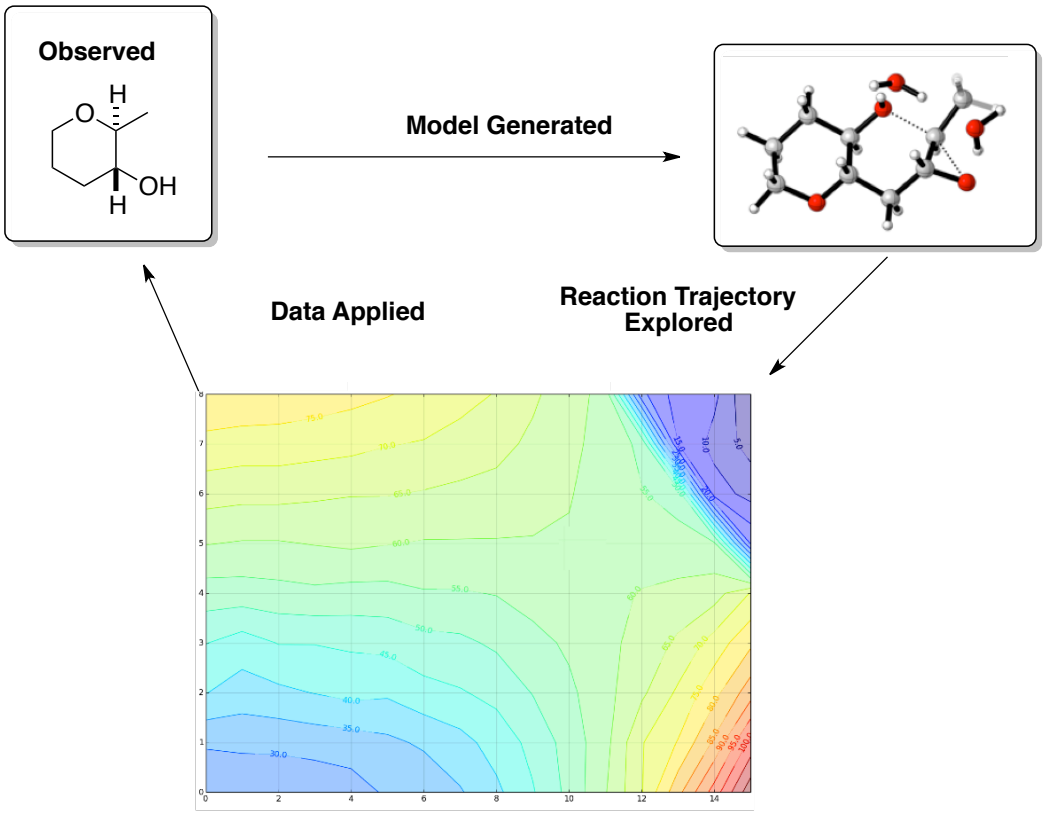

Figure 12. Outline of our method to investigate the 6-*endo*-tet promoted reaction by aqueous solvent.

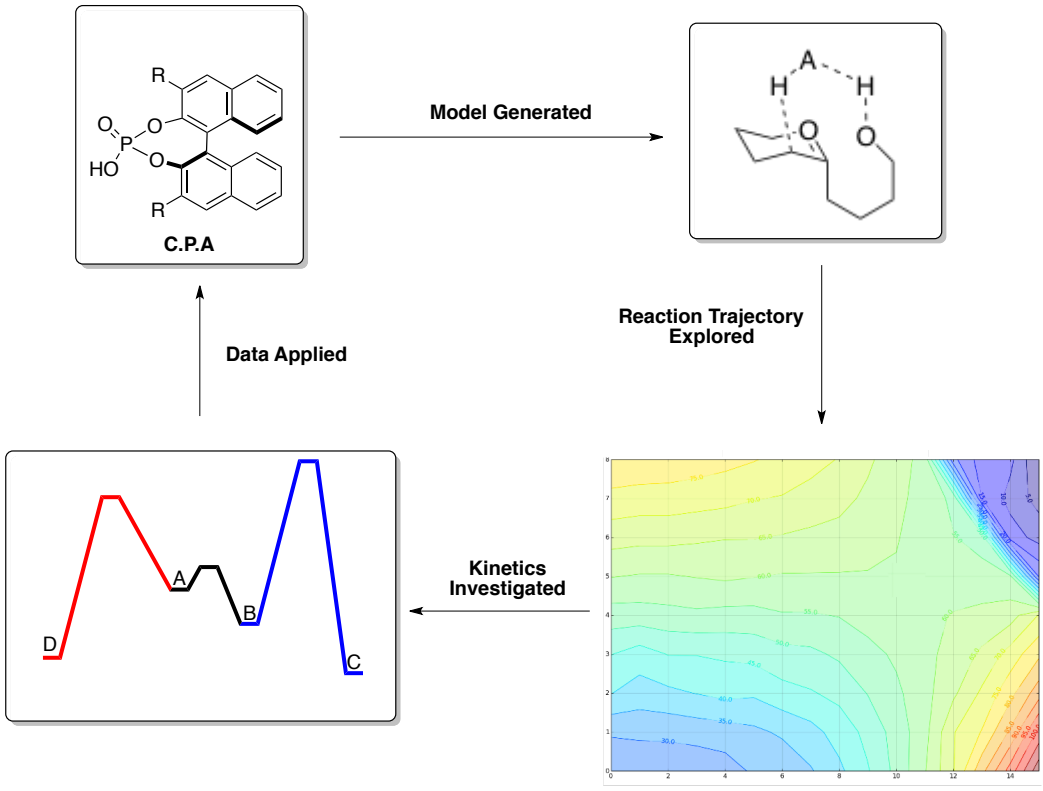

Figure 13. Outline of method used for the computational investigations in Chapter 3 and Chapter 4.

1.3 References

1. Cheong, P.; Houk, K. N. *Nature*, **2008**, 455, 309.
2. http://www.brainyquote.com/quotes/quotes/p/pauldirac279318.html Accessed 3rd March 2016.
3. (a) Donoghue, P.; Helquist, P.; Norrby, P.; Wiest, O. *J. Chem. Theory Comput.,* **2008**, 4, 1313; (b) Augado-Ullate, S.; Urbano-Cuadrado, M.; Villalbe, I.; Pires, E.; Garcia, J.; Bo, C.; Carbo, J. *Chem. Eur. J.,* **2012**, 18, 14026; (c) Ras, E.; Rothenberg, G. RSC Adv., **2014**, 4, 5963.
4. Hong, C.; Tieleman, P.; Wang, Y. *Langmuir,* **2014**, 30, 11993.
5. Schrodinger, E. *Phy. Rev.*, **1926**, 28, 1049.
6. Bachrach, S.M. *Computational Organic Chemistry*. John Wiley and Sons. Hoboken (2007)
7. Kohn, W.; Sham, L. *Phys. Rev.* **1965**, 140, A1133.
8. Perdew, J.; Schmidt, K. *Den. Func. Theo. App. Mater.,* **2001**, 1, 577.
9. (a) Langreth, D.; Mehl, M. *Phys. Rev. Lett.* **1981**, 47, 446; (b) Lanreth, D.; Mehl, M. *Phys. Rev. B.,* **1983**, 28, 1809.
10. Perdew, J.; Burke, K.; Wang, Y. *Phys. Rev. B.,* **1996**, 54, 16533.
11. Tao, J.; Perdew, J. *Phys. Rev. Lett.,* **2003**, 91, 146401.
12. Becke, A. *J. Chem. Phys., **1993***, 98, 5648
13. Lee,C.; Yang, W.; Parr, R. *Phys. Rev. B,* **1988**, 37, 785.
14. Chai, J.; Head-Gordon, M. *Phys. Chem. Chem. Phys.,* **2008**, 10, 6615.
15. Grimme, S.; Ehrlich, S.; Goerigk, L. *J. Comp. Chem.,* **2011**, 32, 1456
16. Zhao, Y.; Truhlar, D. *J. Chem. Phys.,* **2006**, 125, 161103
17. (a) Chung, L.; Sameera, W.; Ramozzi, R.; Page, A.; Hatanaka, M.; Petrova, G.; Harris, T.; Li, X.; Ke, Z.; Liu, F.; Li, H.; Ding L.; Morokuma, K. *Chem. Rev.,* **2015**, 115, 5678; (b) Lundberg, M.; Sasakura, Y.; Zheng, G.; Morokuma, K. *J. Chem. Theory Comput.,* **2010**, 6, 1413.
18. (a) Armacost, K.; Acevedo, O. *J. Am. Chem. Soc.*, **2014**, 136, 147; (b) Li, N.; Chen, X.; Song, J.; Luo, S.; Fan, W.; Gong, L. *J. Am. Chem. Soc.* **2009**, 131, 15301; (c) Sengupta, A.; Sunoj, R. *J. Org. Chem.,* **2012**, 77, 10525.
19. Jensen, J. H. *Molecular Modeling Basics*. CRC Press. Boca Raton (2010)
20. (a) Simon, L. ; Goodman, J.M. *J. Am. Chem. Soc*., **2008**, 4070; (b) Simón, L.; Goodman, J.M.; *J. Org. Chem.* **2011**, 76, 1775.

21. Paton, R. S.; Goodman, J. M. *J. Chem. Inf. Model.* **2009**, *49*, 944.
22. (a) Lam, C.; Priest, D. *BioPhys. Jour.,* **1972**, 12, 248; (b) Sims, P. *J. Chem. Educ.,* **2009**, 86, 385; (c) Seeman, J. *J. Chem. Educ.,* **1986**, 63, 42.
23. Kozuch, S.; Shalk, S.; *Acc. Chem. Res.,* **2011**, 44, 101.
24. Truhlar, D.; Garrett, B.; Klippenstein, S. *J. Phys. Chem.,* **1996**, 100, 12771.
25. Fukui, K. *Acc. Chem. Res.,* **1981**, 14, 363.
26. (a) Marcus, R. *J. Chem. Phys.,* **1956**, 24, 966; (b) Silverman, D. *Biochim. et Biophys. Acta,* **2000**, 1458, 88; (c) Warshel, A.; Papazyan, A. *Proc. Nat. Acad. Sci.*, **1996**, 93, 13665; (d) Warshel, A. *Proc. Nat. Acad. Sci.*, **1978**, 75, 5250; (e) Roca, M.; Vardi-Kilshtain, A.; Warshel, A. *Biochem.,* **2009**, 48, 3046.
27. (a) Eichler, A.; Cricman, L.; Herter, S.; Kelly, P.; Turner, N.; Pieiss, J.; Flitsch, S. *ChemBioChem*, **2016**, 17, 426.; (b) Wijma, H.; Floor, R.; Bjelic, S.; Marrink, S.; Baker, D.; Janssen, D. *Angew. Chem. Int. Ed.*, **2015**, 54, 3726.
28. Verlet, L. *Phys. Rev.*, **1967**, 159, 98.
29. Lazaridis, T.; Karplus, M. *Proteins,* **1999**, 133, 152.
30. Kastner, *J. WIREs Comput. Mol. Sci.,* **2011**, 1, 932.

Chapter 2. Regioselectivity in Epoxide-Opening Cyclizations

2.1.1 Introduction

According to the rules for ring closing events developed by Sir Jack Baldwin on the basis of many empirical observations, the 6-*endo-tet* reaction is formally disfavored.[1] While Baldwin's rules are applicable to intramolecular nucleophilic substitution, there is perhaps more contention when applying these rules to intramolecular epoxide opening reactions: this is because the breaking C-O bond is outside the new ring being formed regardless of the regioselectivity of attack. This has led Jamison and co-workers to introduce the terminology of *fused*/*spiro* to classify selectivity in epoxide opening cyclizations (**Figure 1**), based on the expected transition state structure in each case. Formation of the tetrahydropyran (THP) occurs via the 6-*endo-tet* or *fused* pathway, while the tetrahydrofuran (THF) product results from a 5-*exo-tet* or *spiro* pathway. In Baldwin's original work and later investigations by Alabugin the selectivity of epoxides towards intramolecular attack has been discussed in terms of being intermediate between *tet* and *trig* reactivity.[1] This serves to underlie that regioselectivity of intramolecular epoxide opening is not easily governed by simple empirical rules, and that computations of competing TS structures can be useful towards understanding these reactions. In this chapter, for simplicity we retain the "classic" terminology of 5-*exo* and 6-*endo* ring-closure, although acknowledge that alternative descriptions are possible, and maybe even preferred by others.

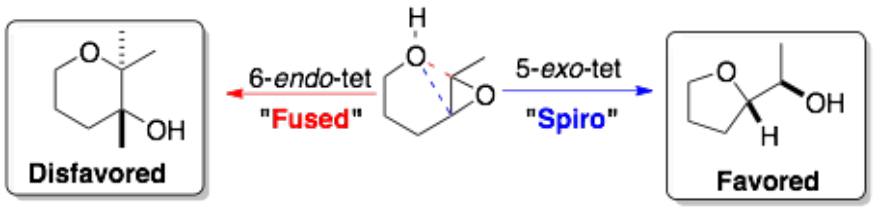

Figure 1. Mechanistic classification of intramolecular epoxide-opening according to Baldwin's rules and Jamison's revised description.

Although a regiochemical preference for 6-*endo-tet ring* closure is well-established with electrophiles such as alkyl halides, with epoxides the occurrence of counter-examples is more frequent.[2] Alabugin has questioned whether 5-*endo-tet* epoxide-openings constitute a formal exception to Baldwin's rules based on the discussions above. Pursuant to this are the enzymes that promote the 6-*endo* cyclization of epoxides, LSD19A being an example,[3,4]. This realization came to Nakanishi in 1985 with the identification of the structure of Brevotoxin and the related polyether natural products.[5] The critical identification of the polyunsaturated intermediate provided a clue and the starting point for K. C. Nicolaou's team to begin the synthesis of the ladder polyether natural product (**Figure 2**).[6,7]

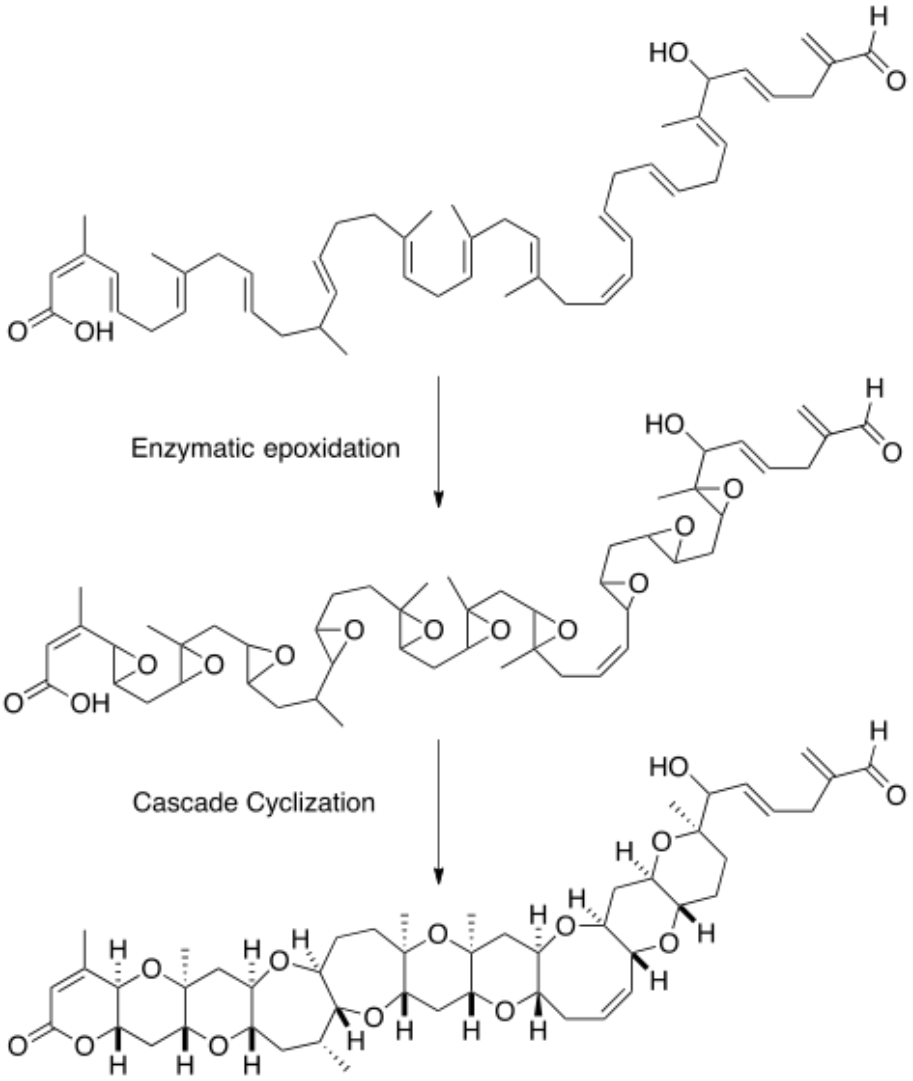

Figure 2. Proposed biosynthesis of Brevotoxin. The putative polyepoxide stereochemistry is not shown as the direction of sequential ring-closures is possible from left-to-right (and *vice-versa*) and remains to be established.

The synthesis of pyran-containing ladder polyethers via a regioselective 6-*endo*-*tet* reaction of epoxides was implicated enzymatically, but unknown by chemical means in the 1980's. Many innovative synthetic processes were developed as a result. We highlight notable synthetic approaches for two such examples, Brevotoxin and Halichondrin B. Brevotoxin is a secondary metabolite produced during algal red-tides. As isolation of the secondary metabolite from its natural source would have not provided enough material for biological testing, Nicolaou and co-workers synthesized the brevotoxin family in the 1990s.[8,9] To construct the three sequential 6-*endo* rings they utilized an electronic directing group to help steer the reaction in 1988.[10]

The 6-*endo* motif in this case was created by utilizing D-mannose as the initial starting point for the terminal ring. Through allyation and protecting group manipulation, a common intermediate was generated which was ultimately used in both the Nicolaou and Yamamoto synthesis of the brevetoxin family.[11,12] From this point, ozonolysis, olefination, reduction, oxidation were carried out to create generate the motifs necessary to promote the 6-*endo* ring closure and subsequent extension of the pyran core (**Scheme 1**).

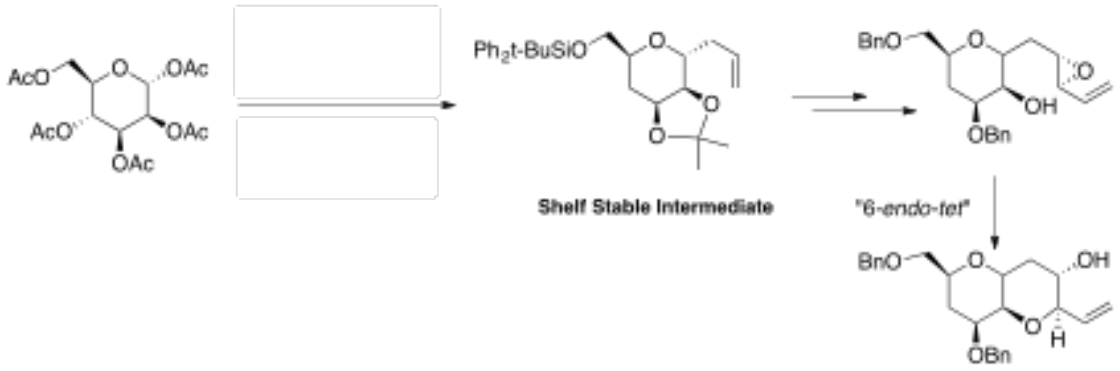

Scheme 1. Nicolaou's process for tetrahydropyran formation, involving regioselective pyran formation by a formal 6-*endo*-*tet* process.

Halichondrin B is a marine natural product discovered in 1986 and first synthesized by Kishi in 1992.[13] This natural product showed immense potential as an anti-cancer drug as it was active against P-glycoprotein resistant cell lines; these cell lines show resistance against Taxol and Vinca alkaloids which target the mitiotic spindle.[14] The Eisai Company has since procured the rights to the derivatives of Halichondrin B and discovered that the eastern hemisphere of the molecule is biologically active (**Figure 2**). Modification of the "tail" and conversion of the ester to a ketone has led to Eribulin (known under the trade name *Halaven*), which displays non-reversible binding to the mitotic spindle. The cytotoxity for this compound is extreme and is only used in late stage and drug resistant breast cancer.

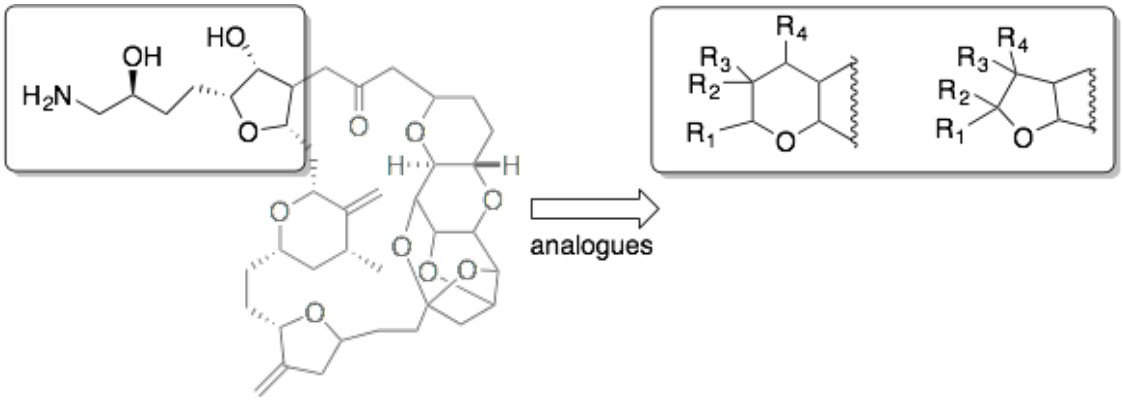

Figure 3. Eribulin (L.H.S.) and a series of pyran/furan derivatives developed during S.A.R campaign (R.H.S.).

This natural product is an exemplar for the industrial application of total synthesis,[15] however, 30 kg of starting material is required to produce 200-300 grams of *Halaven*. The industrial synthesis of the bicyclic pyran utilizes D-gulonolactone as starting material, with the second pyran ring being formed from reacting with methyl 3-trimethylsilyl-4-pentenoate with a basic workup to form the bicyclic pyran ring in one pot (**Scheme 2**). Eisai followed Kishi's route very closely but instead of using D-mannolactone they found that D-gulonolactone provided several downstream advantages. The major advantage was that the intermediates and target synthon could be crystalized, which allowed the development team to avoid using 40 kg of silica gel and 454 kg of petrol based solvent to produce 3 kg of the target synthon.

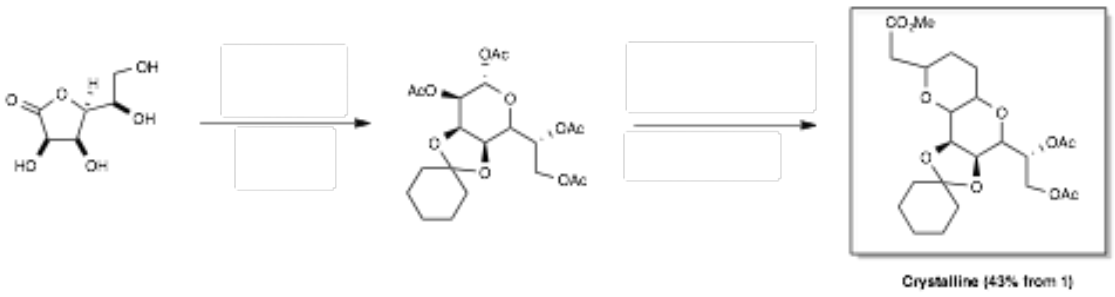

Scheme 2. The Eisai synthetic route towards Halaven.

In this case, a more direct route could be greatly beneficial in terms of both cost and potential for conjugation points as the western hemisphere of Halaven cannot be modified without destruction of the activity and subsequent commercial viability of the compound. Other such natural products include Mupirocin and ionophore

antibiotics.[16,17] Thus, functionalized THP derivatives, which could be generated in 6-*endo*- selective epoxide opening cyclization are attractive targets due to their biological activities, and the fact that this scaffold is relatively under-explored by most drug libraries.[18,19]

2.1.2 Water promoted 6-*endo* cyclizations

Jamison has discovered that water promotes 6-*endo-tet* selective ring-closures of epoxides and cascade reactions of polyepoxides, which occur with the opposite regioselectivity in organic solvents. The regioselectivity towards pyran formation is further enhanced by the presence of a pre-existing pyran ring, in a so-called "templating effect". It was established that with an initial pyran ring already in place, ring-closure occurs with 10:1 6-*endo*:5-*exo* selectivity.[20] The reaction is pH sensitive with the selectivity displaying a bell shape curve that is indicative of a general acid/base catalysis. It is of interest to note that this pH response is also found in the enzymatic promoted 6-*endo-tet* reaction by LSD 19A. Without the template, the 5-*exo* pathway is dominant; the extent of its dominance though is solvent specific.[21] Following this initial discovery subsequent work focused on correlating the product distribution as the template changed and establishing a direct cascade route (**Figure 4**).[22,23]

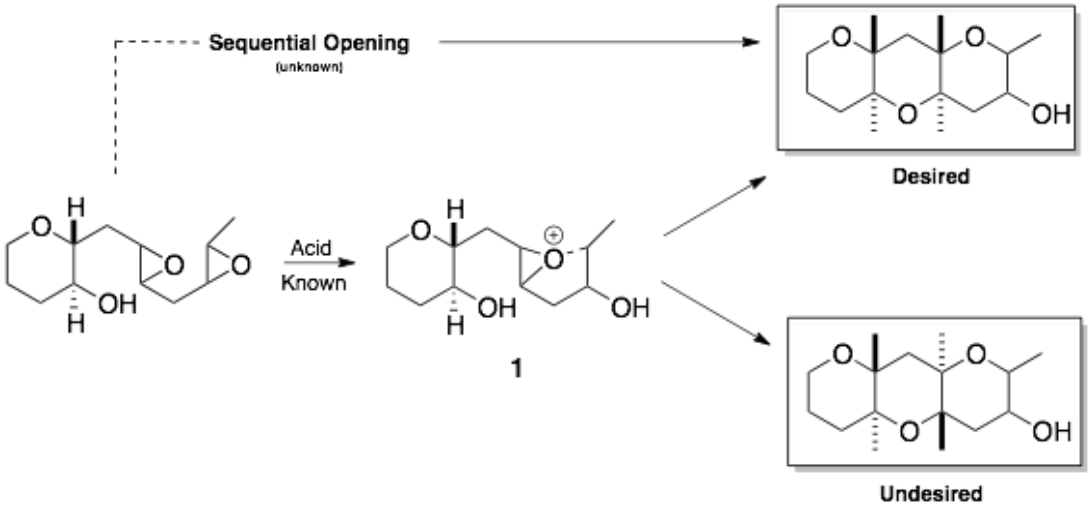

Figure 4. The current synthetic approach generates undesired side products through intermediate **1**. A sequential opening method was discovered by Jamison in the early 2000's that produces a single product.

Through synthetic alteration of the cyclic template, Jamison found that more heteroatoms (dioxane > pyran > cyclohexyl) in this adjacent ring increased the 6-*endo* product selectivity (**Scheme 3**).[24] The cyclohexane derivative showed essentially no selectivity for either THP or THF product.[25]

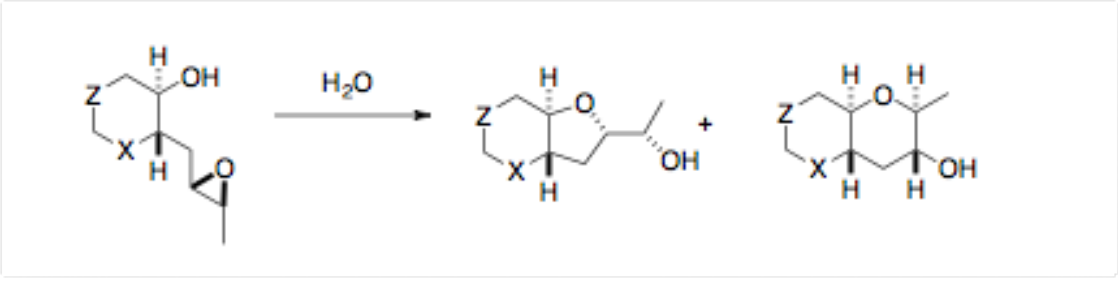

Compound	5-*exo*	:	6-*endo*
X=O, Z=CH_2 : Tetrahydropyran	1		10
X=CH_2 Z=CH_2 : Cyclohexane	1.2		1
X=O, Z=O : Dioxane	1		128

Scheme 3. Substitution pattern effect on the product distribution in epoxide cyclizations performed in water.

The proposed rationale for this variation in product distribution was based on arguments concerning the nucleophilic trajectory, which is affected by the reactant conformation.[20] Baldwin's empirical rules may be similarly rationalized in terms of the stereoelectronic requirements imposed associated with each reaction type.[1] Jamison has proposed that a twist boat/skew boat conformation is required to facilitate the nucleophilic attack: this should be more facile for a pyran than cyclohexyl ring (**Figure 5**). However, no experimental or computational evidence supports this hypothesis directly. On top of this, water was shown to be actively discriminating between the two-TSs not through classic enthalpic interactions but through entropic effects.[25] This

work gave us a compelling basis to study the basis for 6-*endo-tet* ring closure of epoxides computationally.

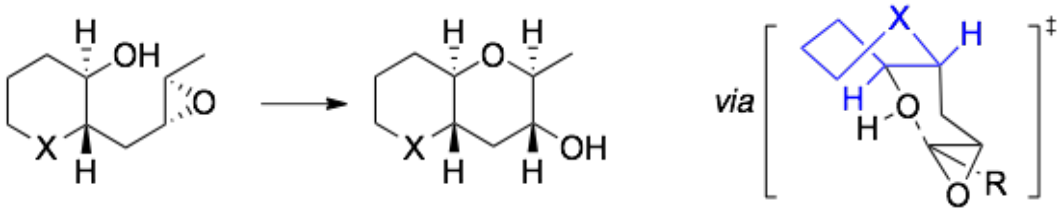

Figure 5. Proposed transition state model to account for the 6-*endo-tet* templating effect of a pyran ring.

2.1.3 Epoxide reactive trajectories: a meta-analysis

The physical foundation underlying the idea that nucleophiles follow fixed trajectories came from the crystallographic observations of Bürgi and Dunitz. They showed a series of structures with an amino group at varying distances from the electrophilic carbon of a ketone, in which the O-C-N angle (i.e. the nucleophlic trajectory) took values around 105°. A similar analysis had not yet been performed for epoxide functional groups, so we used the Cambridge Structural Database to do so, finding 33 examples of epoxides with contacts between the electrophilic C-atoms and a non-bonded oxygen atom.[26] There were no examples of other heteroatoms positioned within a cut-off of 3.0Å (based on van der Waals radii of r_O = 1.52Å, r_C = 1.70Å. Our statistical analysis in **Figure 6** shows that most structures are clustered within 135-170° (of the O---C-O angle) with a C-O distance of 2.8-3.0Å. A single structure (shown) is responsible for the two shortest contacts, where a water molecule lies in contact with both epoxide carbon atoms: interestingly, the epoxide C-O bonds are unsymmetrical (1.47 *vs.* 1.43Å) seemingly indicative of weakening at the side where the water molecule lies closer (2.14 *vs.* 2.39Å). The spread of our empirical data (in terms of the angle of approach) suggests that the approach of the oxygen atoms is relatively free, however, it is dangerous to extrapolate to the transition structure for nucleophilic attack from these solid state structures.

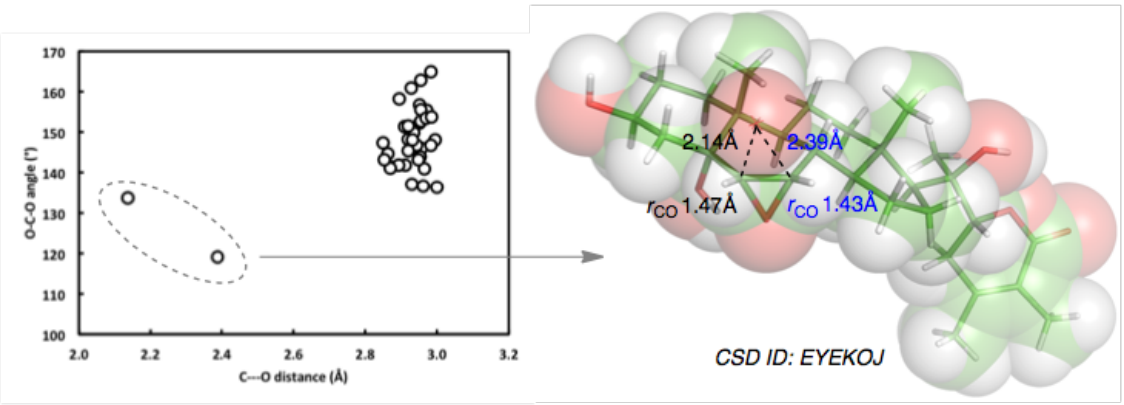

Figure 6. Meta-analysis of all X-ray crystal structures showing epoxide non-bonding contacts with oxygen atoms; the outlying structure is shown.

To understand the stereoelectronic basis of epoxide attack it is useful to consider the computed charge distribution and lowest unoccupied Molecular Orbtial (LUMO), which we have performed for the ethylene-epoxide. The electrostatic potential is, as expected, polarized so that the oxygen is negatively charged and the two carbon atoms are positively charged. Electrostatically, approach of a nucleophile is preferred from the opposite side of the O atom. The computed epoxide LUMO is formed from the out-of-phase combination of the orbtials on all three heavy atoms, with largest lobes on the carbon atoms. Immediately, it can be seen why the selectivity of epoxide-opening has been compared with alkene electrophiles: the two lobes on each carbon, with a central node, resemble the shape of a * LUMO for an alkene (**Figure 7**). For this symmetrical epoxide, both the charge distribution and the LUMO coefficients are symmetrically distributed, however, introduction of different substituents to each carbon atom will lead to polarization, and also different steric requirements at each position. Thus is becomes difficult to extrapolate this simple orbital picture to the several examples of regioselectivity discussed above, so that we have performed optimizations of the competing TS structures in each case.

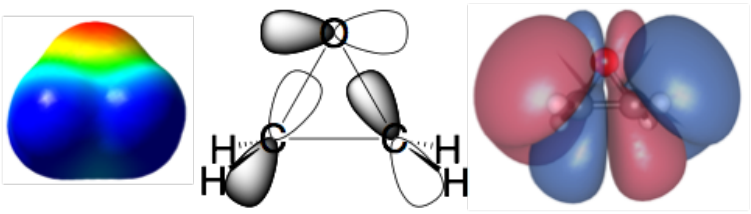

Figure 7. M06-2X/6-31G(d) computed electrostatic potential map and in plane LUMO for ethylene oxide.

2.1.4 Computational methodology

Model generation is essential for us to accurately discern the internal and external effects that promote 6-*endo-tet* selectivity. From Jamison's work we know that the 6-*endo* reaction has a second order dependence on the concentration of water as well as a solvent kinetic isotope effect indicative of proton transfer in the rate determining step, SKIE=1.33.[27,28] We hypothesized that tightly-coordinated water molecules could act as a source of strain that could help discriminate between the 5-*exo* and 6-*endo* trajectories. If the solvent "bridges" between the nucleophile and electrophile then we would have a transient but rigid secondary structure in the competing TS structures. Such a mechanism would imply an associated enthalpic and entropic cost of having to break multiple solvent-solvent interactions and reorganize the water into a well-defined conformation (**Figure 8**).

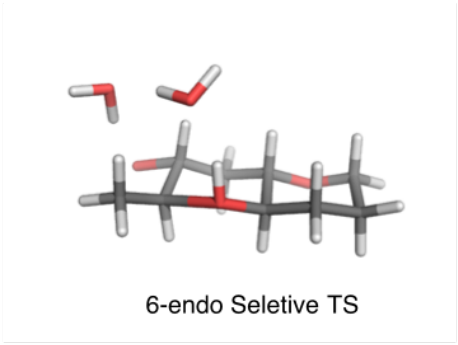

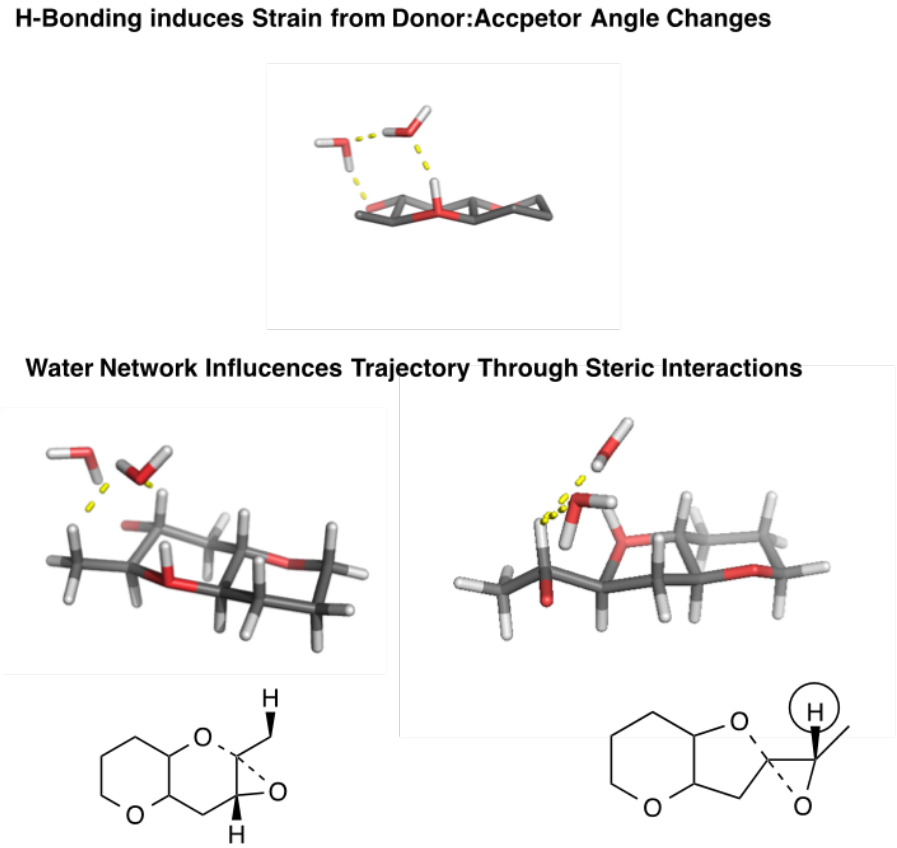

Figure 8. Proposed possible interactions between solvent and compound that could help discriminate between TSs.

The solvent bridge postulate is reflected below in **Figure 9,** by the models **1A** and **2B**. To remove any bias we also created models based on theories postulated by Jamison (**3A/B** and **4A/B**) to explain regioselectivity within their respective studies (conformational effects). The most common approach to identifying the correct model would be the comparison of the relative energy difference with the intent of finding the lowest energy species. Unfortunately, in this case the atom count is different for different solvent models, as well as the introduction of specific interactions in the

discrete mechanisms. We gauged the success of the models by comparing the predicted selectivity and solvent kinetic isotope (SKIE) effects against the reported values. Since this reaction is kinetically controlled (epoxide opening is irreversible) we could directly compare the TS energies to calculate the product distribution. Ground state (GS) and transition state (TS) structures were optimized at the M06-2x/6-31G(d,p) level of theory with an implicit conductor-like polarizable continuum model (CPCM) for the non-interaction solvent molecules.[29,30] This functional, developed by Truhlar, has shown to be able to obtain thermodynamics and kinetics of epoxide openings which are comparable to Coupled-Cluster (CCSD) benchmark calculations.[31]

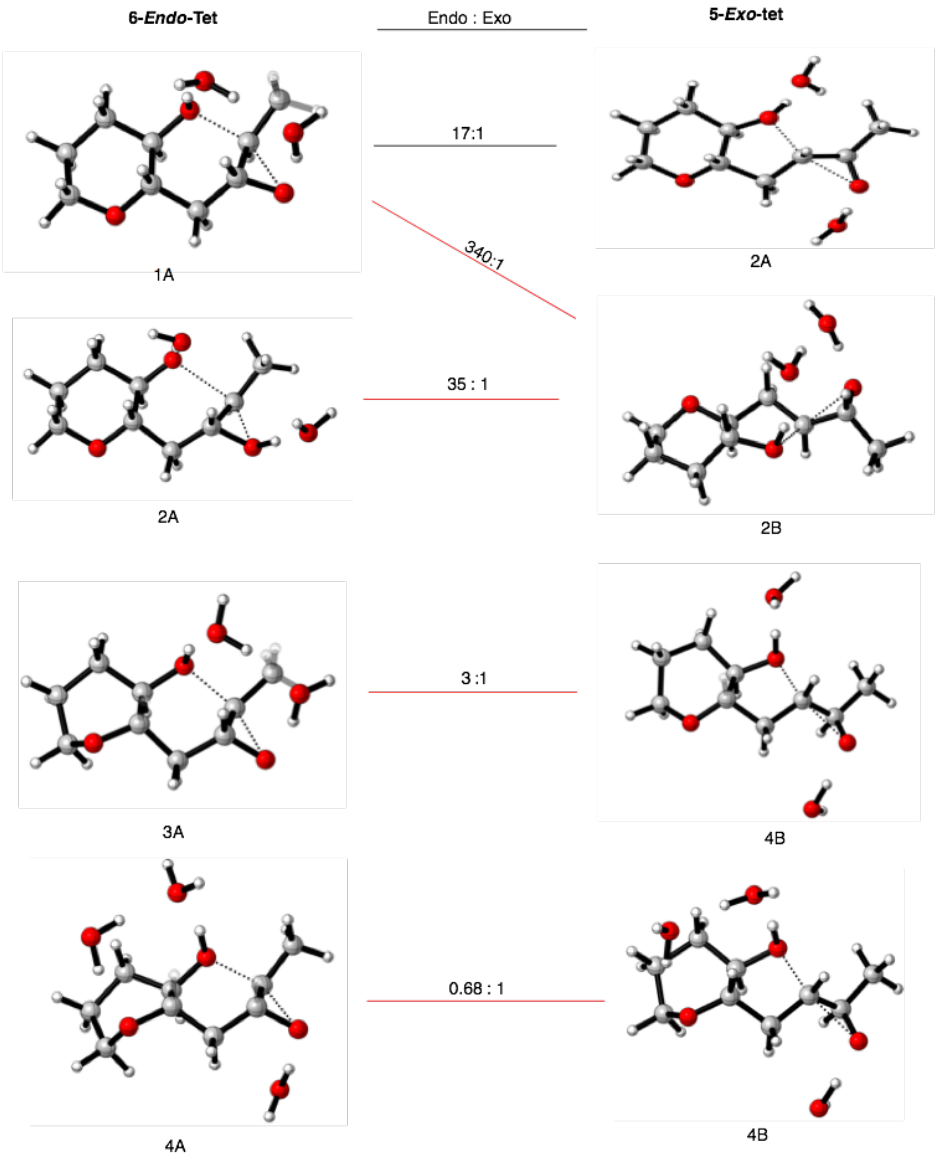

Figure 9. Schematic of different models for solvent and conformation interactions in the TS. 6-*endo* is the A class while 5-*exo* is B class; values in center represent the relative selectivity.

6-*endo* Model	5-*exo* Model	Predicted Selectivity (THP : THF)
1A	1B	3 : 1
1A	2B	1 : 156
1A	3B	1 : 3075
2A	1B	283,290 : 1
2A	2B	340 : 1
2A	3B	17 : 1
3A	1B	582,886 : 1
3A	2B	700 : 1
3A	3B	35 : 1

Table 1. Complete comparison against all models activation barriers and the estimate for the relative selectivity between them.

In the following discussions we discuss the "trajectory" of nucleophilic attack: several definitions are possible and we have defined the O-C-C angle made by the nucleophilic oxygen with the epoxide carbon atoms. In terms of approach, based upon the idea that the epoxide shares a similar LUMO to alkenes, we consider that angles approaching a Bürgi-Dunitz trajectory, around 105°, are closer to ideal. Based upon our computed LUMO, there is a node in-between the two C atoms, so we would expect more acute trajectories to suffer from destructive overlap.

We were elated to find that our model **1A**, which captures the second order dependence of the solvent and **2A** the representation for the first order dependence for cyclization by 5-*exo* resulted in a predicted product distribution of 17:1 which nearly matched the

experimental selectivity of 11:1. The difference between the 6-*endo* and 5-*exo* selectivity for the calculated and experimental results was 0.30 kcal/mol. To investigate Jamison and co-workers' hypothesis about the twist boat we decided to investigate the effect of having a 3rd water (4A) relative to having only two water molecules 3A. From their hypothesis, the internal hydrogen-bonding network to the *endo*cyclic oxygen is important in stabilizing the twist boat formation, which increases the population of this high-energy conformation relative to the chair. From this twist boat structure they believed that the distorted angles would allow the nucleophile to approach from an improved trajectory (**Figure 8**). From our calculations for the 6-*endo-tet* trajectory we found that the introduction of the 3rd water to interact with the *endo*cyclic oxygen did result in an improvement of the approach trajectory. The twist boat with two waters (**3A**) displayed a trajectory of 102.8° while the trajectory for the 3 water model (**4A**) resulted in an increase in the approach angle to 107.8°. From our calculations though, the introduction of the 3rd water resulted in a decrease in the 6-*endo* selectivity from 3:1 to 0.68:1 (*endo* :*exo*). To explore this result further we decided to investigate the new steric interactions that could introduce the shift in selectivity (3B vs. 4B).

The 5-*exo* trajectory has changed very little with the introduction of the 3rd water **3B**: 108.3^0, **4B**: 107.1^0. The nucleophilic position has not changed (1.85 Å) nor has the leaving groups' position (2.05 Å). The TS for the 6-*endo-tet* reaction becomes later with the introduction of the 3rd water (**3A – 4A**). As the approach trajectory has greatly improved over that of the chair conformation we would not expect the outcome that we were predicting. To better understand this effect we investigated the thermodynamic changes for both the product and substrate and the TS difference between the chair conformations and the twist boat shifts. By comparing the starting ground state (acyclic chain) for the chair and twist boat with two waters (1A and 3A) we find that chair conformation is more stable by -3.2 kcal/mol, resulting in a product ratio greater than 109 : 1. More importantly, the 6-*endo* TS for 1A is more stable by 7.4 kcal/mol. This shows that even though the approach trajectory improves by 1.4°, the unfavorable steric interactions between the template and new ring could be the driving force for this increase in the activation barrier. If this is true, we would expect to find that 6-*endo* products would display a similar trend. What we find when we compare the product

energy differences is that the chair-chair product is more stable by 6.4 kcal/mol relative to the twist-chair conformation.

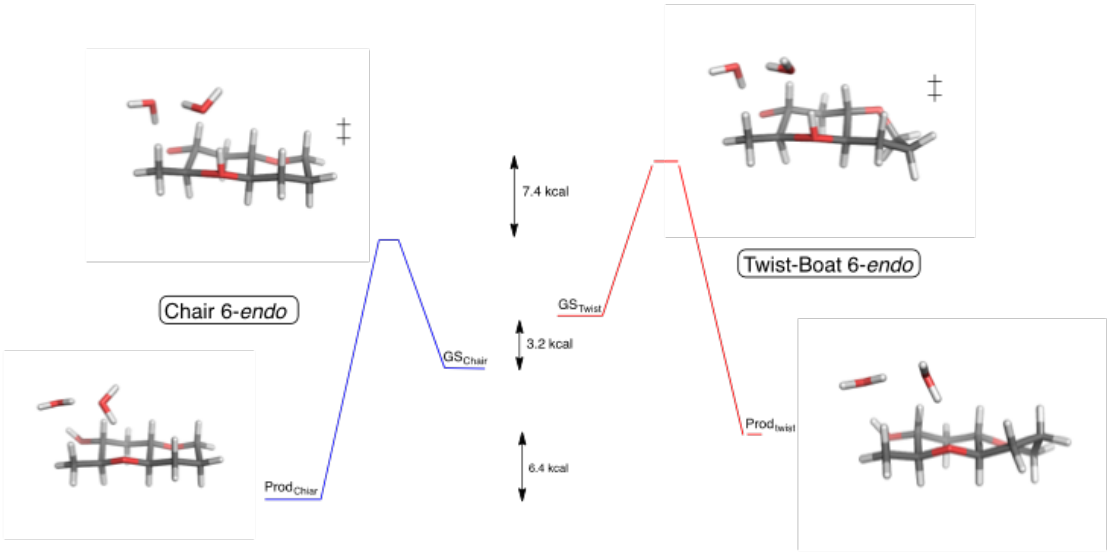

Figure 10. Reaction profile comparison between the 6-*endo* chair conformation relative to the twist-boat conformation.

Evidently, the hydrogen bonding interactions in the twist-boat TS do not compensate for the inherent, unfavorable conformational penalty. Our computational work thus suggests that the prevailing hypothesis, of a water-promoted twist-boat TS, is unlikely. Additionally, in experiments the 6-*endo*-selectivity increases for trans-fused pyran templates with two and three rings: such systems would be expected to show an even greater bias away from the twist-boat in favor of the chair conformations, such that the original mechanistic model is further weakened.

To determine the validity of our water placement we utilized a computational technique developed by Singleton,[32] which involves altering the mass of the exchangeable hydrogens and recalculating the activation free energy barrier with the subsequent alterations. The comparison of the new rates allows us to calculate the solvent isotope effect. The SKIE changed marginally between the water bridging model (**1A**) and non-bridging model (**2A**); 1.20 and 1.19 respectively (**Figure 11**). This is lower then the experimental result of 1.33, which lent support to the theory of a proton transfer within

the TS. To investigate a plausible reason for the lower value we profiled our **1A** model using the intrinsic reaction coordinate (IRC) technique.[33] We found that following the TS there is a proton shuttle between the reacting groups and the bridging waters (**Figure 11**). Along the IRC pathway we find that the proton transfer is "shoulder" off the traditional direct pathway down to the products. This "shoulder" has been characterized by Henry Rzepa and has been shown to be caused by a low TS barrier step, or a very high-energy intermediate.

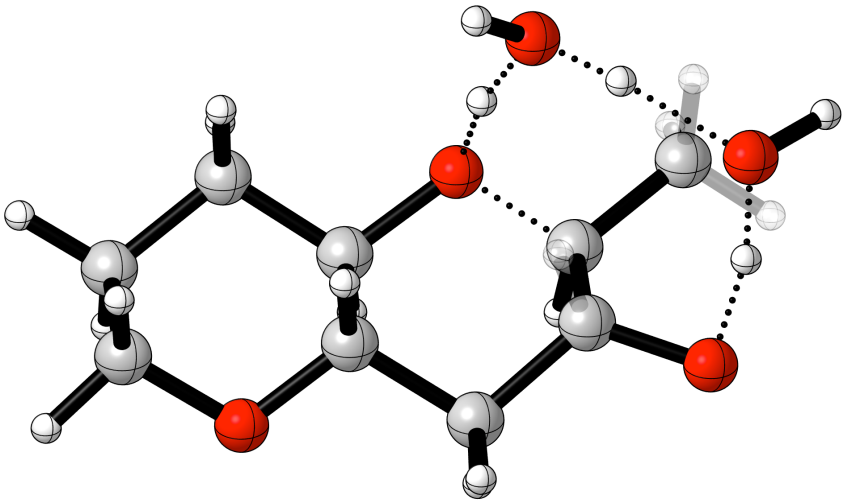

Figure 11. Proton transfer following RDS of the 6-*endo* transition state.

2.2 Classic 6-*endo*-selective approaches to epoxide opening

2.2.1 4,5-*trans*-epoxyhexanol

To begin our investigation we wanted to establish any inherent controlling factors before beginning a more comprehensive investigation. We selected *trans*-4-5-epoxyhexanol as our control model as this model was relatively simple and had experimental results for the reaction run in water (**Figure 12**).[21]

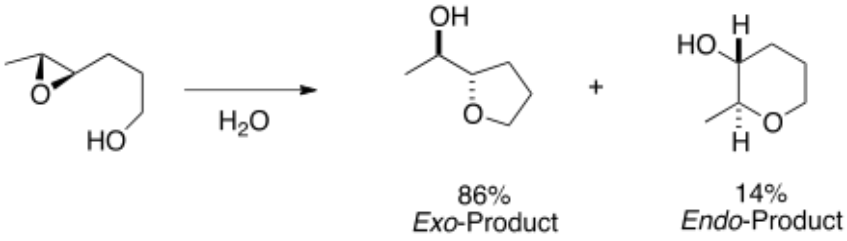

Figure 12. Product distribution for the ring-closure of *trans*-4-5-epoxyhexanol in boiling water.

The epoxide ring opening and subsequent cyclization are under kinetic control and thus activation barrier differences would allow us determine the favored reaction course. Acidic and basic reaction conditions were computed separately, by modeling them as extreme cases, i.e as a fully protonated epoxide, and as a deprotonated alcohol. This would correspond to specific acid/base catalysis. All TS structures, corresponding to the formation of THP and THF products, were optimized at the M06-2X/6-31G (d,p) level of theory with an implicit CPCM water solvent correction. The results are collection in **Table 2**, **Figure 13, and Figure 14** below.

Under acidic conditions, the 5-*exo* TS is able to undertake a more favorable trajectory then is 6-*endo*-counterpart by 11° (**Table 2)**. Under basic and neutral conditions the 5-*exo* and 6-*endo* reaction trajectories are more similar, differing only by 2.1°. For both acid and base catalyzed reactions the 5-*exo* TS is the more stable, in contrast to the water-promoted reaction, where the 6-*endo* TS is more stable. The transition state energy difference is highlighted in **Figure 13**.

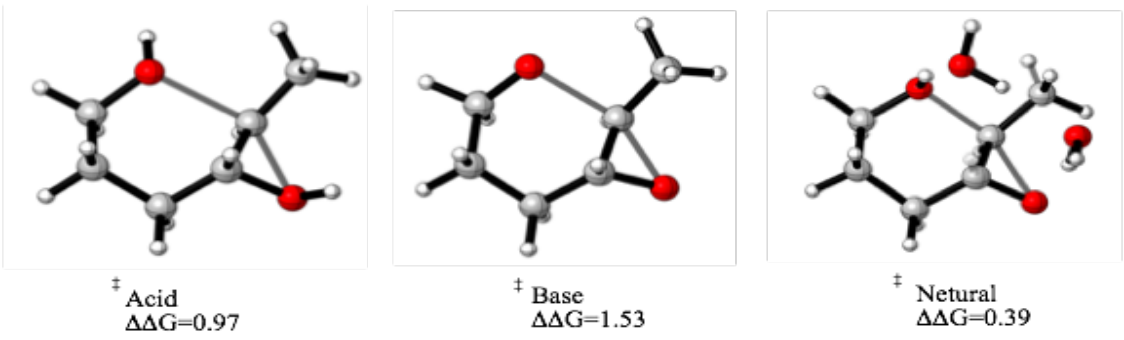

Figure 13. M06-2x/6-31G(d,p) TS energy difference between the 6-*endo* and 5-*exo* transition state. The positive value indicates that 5-*exo* is the favored pathway.

Conditions	TS	$\angle_{O\cdots C\text{-}C}$ (°)	$O_{nuc}\cdots C$ (Å)	$C\cdots O_{elec}$ (Å)
Acid	5-*exo*	103.4	2.18	1.83
	6-*endo*	92.12	2.21	1.84
Neutral	5-*exo*	104.6	1.92	2.00
	6-*endo*	101.6	1.92	1.99
Basic	5-*exo*	105.5	2.05	1.77
	6-*endo*	103.4	2.05	1.76

Table 2. CPCM-M062x/6-31G(d,p) approach trajectory under varying reaction conditions for the competing TSs.

From the traditional arguments based on Baldwin's rules it seems very odd that under basic conditions the 6-*endo* approach shows the greatest approach angle but the worst selectivity. After analyzing the structure of the 6-*endo*-TS we find the source of the increased discrimination of the 6-*endo* TS. To approach the reaction center from such a favorable trajectory, the 6-*endo* TS has to induce the ring formation significantly earlier, which resulted in unfavorable 1,3 interactions with the forming ring. This can viewed trying to "jump the gun" on the ring formation induced by an associative TS.

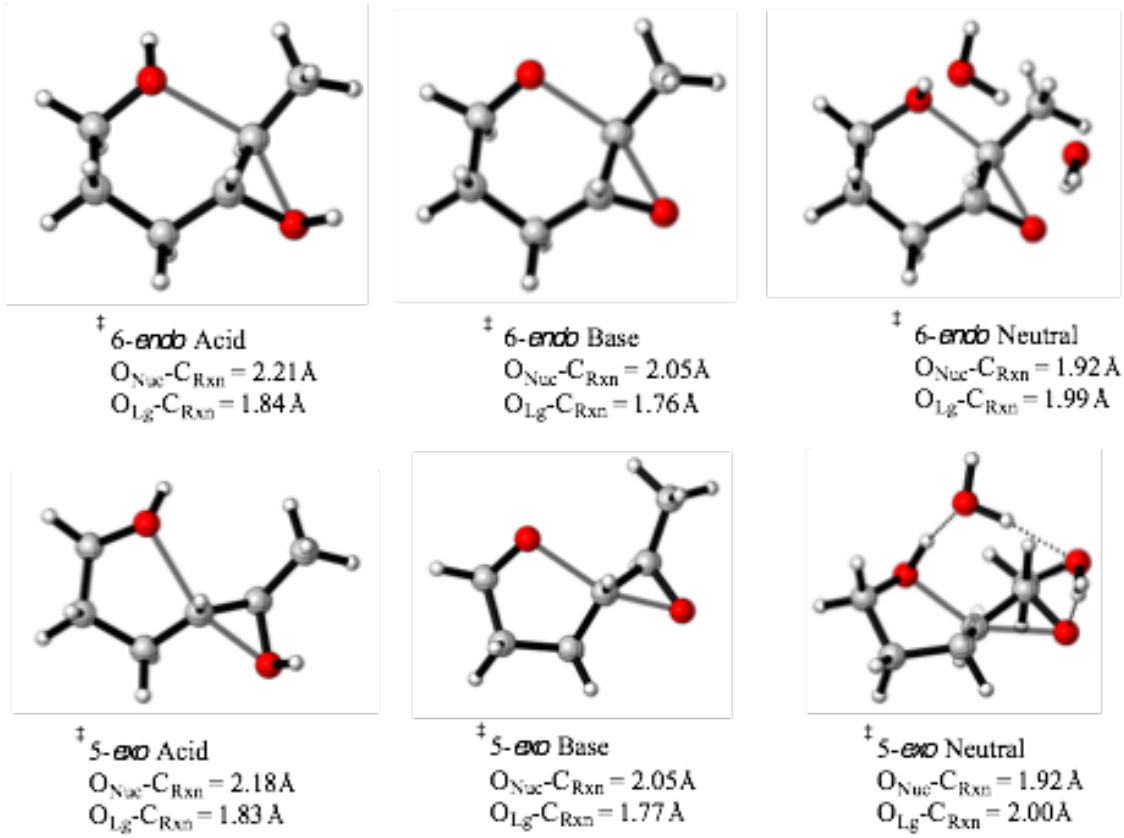

Figure 14. M06-2x/6-31G(d,p) TS structures; bond distances (Å) under various conditions for the respective TSs.

From a qualitative inspection of TSs, we can see that the pyran core is much more developed under neutral conditions then the acidic conditions. Based on the Hammond-Leffler postulate, a later TS would emulate the structural characteristics of the products. As this reaction occurs in water and the trajectory is sensitive to electronic steering it would be interesting to ascertain a quantitative interpretation of these factors to utilize during the analysis of other scaffolds.

Traditionally, determining the charge build-up in a TS can be probed through experimental Brønsted or Hammett relationships, which can be used to understand the changes in bonding taking place. To perform such a task computationally, we used the Natural Bond Orbitals 6 (NBO) program. This has developed a strong following for its capacity to robustly assign charges on atoms in complex structures, is also able to quantify formal bond orders of 2-center, 2-electron bonds: We have used Wiberg bond

orders (WBOs), which are more sensitive than the interatomic distance to the degree of bonding character.[35] In this scheme, a value of zero indicates no bond, one a full single bond, and intermediate values a partial bond, where the magnitude of the WBO is indicative of the degree of bond formation. This of course has found application in determining the magnitude of interactions between a catalyst and TS to help explain stereoinduction.[36] Our NBO calculations were utilized to help determine the TS position in terms of the extend of alcohol C-O bond formation and epoxide C-O bond cleavage.

From the NBO computed WBOs (here, abbreviated as $B_{Nuc/Lg}$) we found that TS for both 6-*endo* and 5-*exo* under neutral conditions increased to become more product like (**Table 3**). The greatest impact on the TS from the Brønsted acid and base case was on the 6-*endo* nucleophile, 0.39 and 0.18 respectively relative to the neutral case of 0.52. Under both Acidic and neutral conditions we find that the TS is dissociative, meaning that the leaving group has broken its bond to a greater extent then that of the approaching nucleophile. Under basic conditions, the **TS** is more associative which could help explain why the conformation has adopted unfavorable dihedral angles.

Conditions	TS	$\angle_{O\cdots C\text{-}C}$ (°)	B_{Nuc}	B_{Lg}
Acid	5-*exo*	103.4	0.16	0.40
	6-*endo*	92.12	0.13	0.18
Neutral	5-*exo*	104.6	0.50	0.58
	6-*endo*	101.6	0.52	0.57
Basic	5-*exo*	105.5	0.35	0.36

6-*endo*	103.4	0.34	0.34

Table 3. Characterization of computed TSs based on relative distance of TS and the approach trajectory.

From our calculations it would appear that a more product-like and slightly dissociative TS allows the 6-*endo* trajectory to become much more favored. The results for our simple *trans*-4,5-epoxyhexanol model reaction highlight that the position of the TS can have a significant affect on the product distribution. The dissociative nature found under the other reaction conditions could help explain how the reaction trajectory has been classically steered through electronic perturbation. To explore the inherent characters that help control the ring closure events we will investigate the two synthetic approaches developed to controlling ring closure: allylic and trimethylsilyl (TMS) steering groups (**Figure 15**).[10,37]

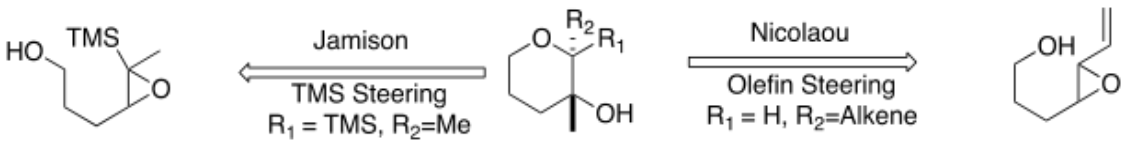

Figure 15. Retrosynthetic approach to 6-*endo* epoxide ring closure utilizing steering groups.

2.2.2 6-*endo*-selective closure of allyl-epoxides

In 1988 Nicolaou published an approach to achieve 6-*endo-tet* selective ring closure with allyl-epoxides (**Figure 16**). Empirical evidence has led to a understanding that the regioselective opening of epoxides are highly sensitive to electronic groups near the reaction center. Based on this, Nicolaou *et. al.* decided to incorporate an allylic system near the 6-*endo* reaction center to steer the reaction outcome. They found that with the introduction of the allylic system, the THP was the dominant product and that the

isolated yield increased for more electron-rich alkenes. Nicolaou also tested reactants with greater substitution at the reaction center and showed that their methodology was also insensitive steric interactions at the 6-*endo*-reaction center.

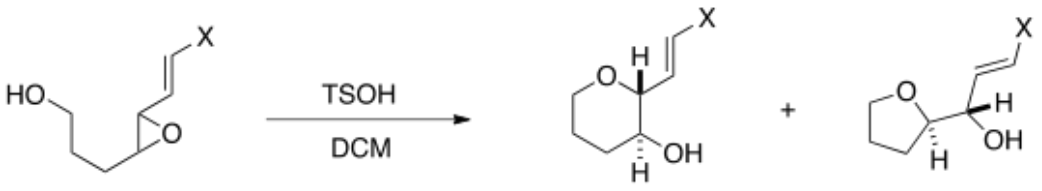

Compound	6-*endo*	:	5-*exo*
X = H	100		0
X = CO_2Me	60		40

Figure 16. Regioselective epoxide cyclizations with allylic steering groups developed by Nicolaou.

To begin our computational study we investigated the olefin stabilized reaction course promoted by a Brønsted acid (a strong acid, TsOH, was used experimentally). To simulate the effects of specific acid catalysis we assume the epoxide is fully protonated, and TSs and GSs were optimized at the M06-2x/6-31G(d,p) level of theory with a CPCM description of dichloromethane (DCM) solvation. We found that the difference in stability between the two competing TS structures is 3.7 kcal/mol, with the favored reaction course being the 6-*endo*. The magnitude and sense of selectivity match the experimental outcome (**Figure 17**), which is completely selective for the THP product.

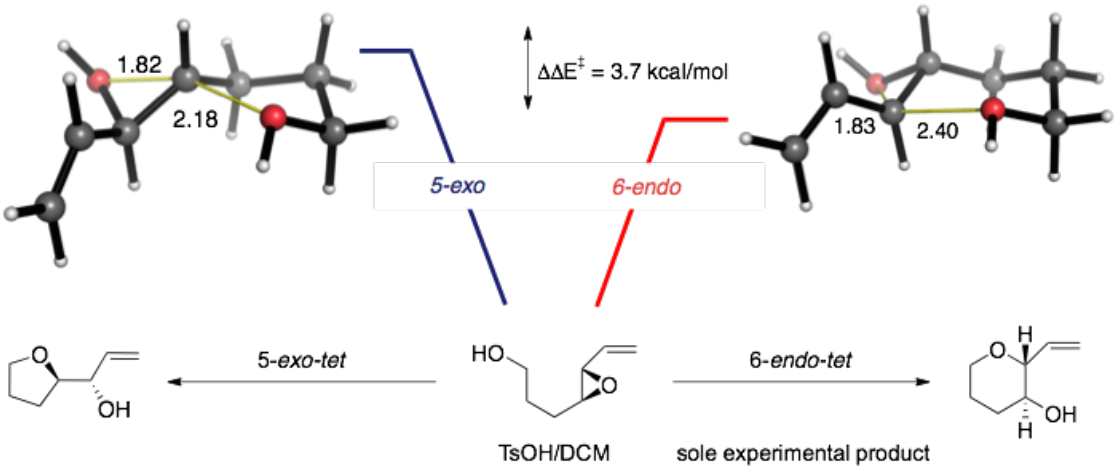

Figure 17. CPCM-M06-2x/6-31G(d,p) competing TS structures for the Brønsted acid promoted cyclization of an allylepoxide.

The computed TS structures show us that indeed the olefin stabilizes the development of carbocationic character at the adjacent carbon, with bond shortening between the internal olefin and alpha carbon. The approach trajectory is 87.5° which is a decrease of 4° from the 4,5-*trans* species. The position of the 6-*endo* TS is earlier with the nucleophile being 0.1 Å further away from the reaction center resulting in a more dissociative TS. The experimental observation that the C-6 carbon substitution had no impact on the 6-*endo*-product distribution (i.e. forming a quaternary center) helps to support our TS calculations as an "exploded" TS as we would expect the TS to be less sensitive to steric interactions.

TS	$\backslash_{O\cdots C\text{-}C}$ (°)	d_{Nuc} (Å)	d_{Lg} (Å)
5-*exo*	101.3	2.2	1.8
6-*endo*	87.5	2.4	1.8

Table 4. Characterization of TSs with an allyl steering group based on approach trajectory.

The 5-*exo* trajectory is unchanged with the introduction of the olefin. This result is not unexpected as conjugation doesn't extend beyond the ⟨-carbon. We believe that the 6-*endo*-*tet* reaction is accelerated by the stabilization of the TS through conjugation. The lowering of the intrinsic barrier for the 6-*endo* trajectory alone could help explain the large difference in the TS barriers. Two related arguments can be presented to rationalize the product distribution due to the allylic group; hyperconjugative donation from the –bond weakening the adjacent C-O bond, or alternatively, the in-phase combination of * and * orbitals producing a lower energy LUMO (analogously to the Polar Felkin-Anh Model) as shown in **Figure 18**. The net result of both hyperconjugative arguments is the 6-*endo* reaction would display a dissociative TS and the effect of the interaction would be limited to the ⟨ carbon (C-6).

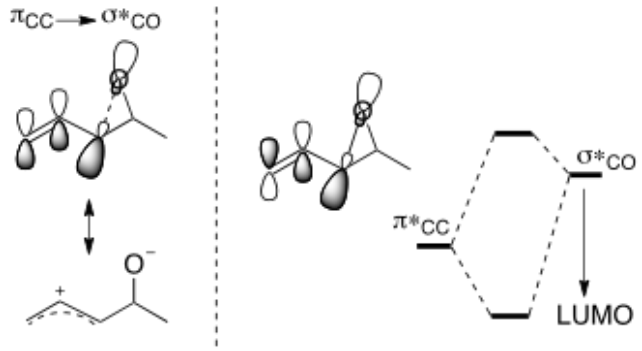

Figure 18. Stereoelectronic arguments to rationalize product selectivity with an allyl steering group.

One aim of Nicolaou's methodology was to form extended polyether skeletons found in several natural products, and consequently he investigated sequential cyclizations. A pyran template increased the 6-*endo*-*tet* selectivity with an ⟨-® unsaturated ester from 60:40 to 92:8 (*endo*:*exo*) as in **Figure 19**. As this mimics the template effect observed by Jamison, but now under anhydrous conditions, we investigated this reaction further. As summarized by **Table 5** the nucleophilic trajectory obtained for THF formation is unchanged from the allyl epoxide studied above, while the THP trajectory shows evidence of less activation from the neighboring group: the angle of approach is larger by 2.5° and bond formation is more advanced in the TS.

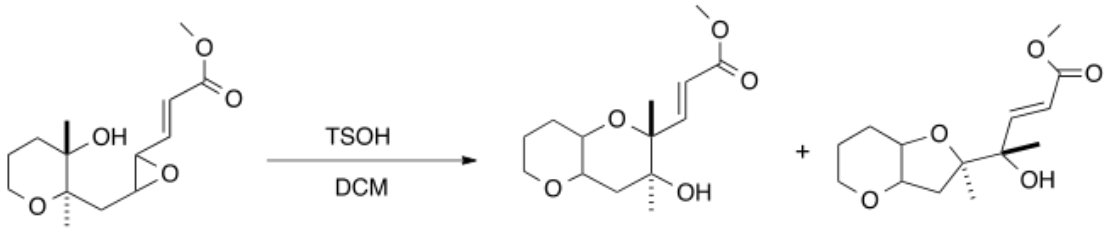

Compound	6-*endo*	:	5-*exo*
No Template	60		40
THP Template	92		8

Figure 19. Combination of an allylic substituent and a pyran template in epoxide-cyclization.

TS	$\backslash_{O\cdots C\text{-}C}$ (°)	d_{Nuc} (Å)	d_{Lg} (Å)	⊗⊗$E^{‡}$ (kcal/mol)
5-*exo*	101.3	2.2	1.8	1.3
6-*endo*	90.0	2.3	1.8	0

Table 5. Characterization of the TSs for ring closure with an ⟨-® unsaturated ester steering group (no pyran template).

With the electron deficient alkene we find that 6-*endo* selectivity has decreased from 3.1 kcal/mol to 1.3 kcal/mol which would result in a product distribution drop from >99 to 90% selectivity. The observable product distribution change may seem small but based on the change in the TS stability this effect is significant. From the structures alone we can see that the TS has become later with the nucleophile 0.1 Å closer to the reaction center, relative to the olefin model (**Figure 20**). From our 4,5-*trans*-epoxy alcohol calculations we would expect the later TS to result in a improved trajectory approach. From a structural comparison of the 6-*endo* TSs we find the C_{alpha}-C_{alkene} bond distance is the same for both TSs at 1.44 Å. The epoxide distance has not changed as well which would point to the TS becoming more associative relative to alkene. As we have seen from our basic model, an associative TS could result in increased unfavorable 1,3 interactions. This structural information informs us that the olefin

could be stabilizing the 6-*endo* TS through hyperconjugation, which supports the first argument presented above, namely than hyperconjugative donation from the ♦–bond weakens the adjacent C-O bond.

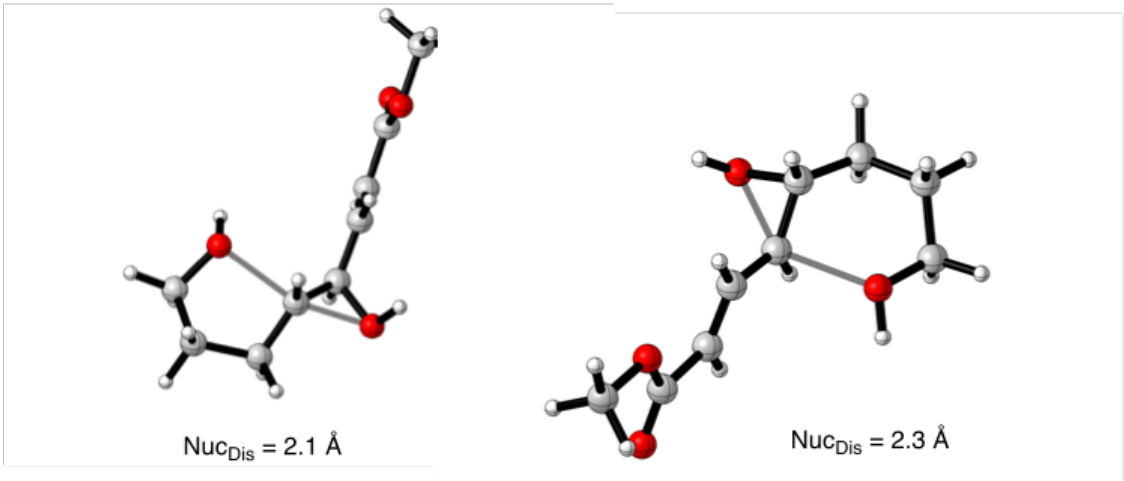

Figure 20. CPCM-M06-2x/6-31G(d,p) competing TSs for ring closure with an ⟨-® unsaturated ester steering group (no pyran template).

With the introduction of a pyran template Nicolaou found that the selectivity for the 6-*endo* product distribution increased from 60% to 90%. With the introduction of the template we find that the TS has become more dissociative when compared to the non-templated case above. The nucleophile's position has retracted back to 2.29, nearing that of the alkene case, and the epoxide bond length has stayed the same (**Table 6**).

TS	$\backslash_{O\cdots C\text{-}C}$ (°)	d_{Nuc} (Å)	d_{Lg} (Å)	⊗⊗$E^{‡}$ (kcal/mol)

5-*exo*	101.8	2.2	1.9	2.9
6-*endo*	88.9	2.3	1.9	0

Table 6. Characterization of the TSs for ring closure with an ⟨-® unsaturated ester steering group with an existing pyran template.

Our initial hypothesis is that the template induces a conformational restriction that helps to promote the 6-*endo* trajectory. When we compared the critical dihedral angles we found that they did not differ significantly from the acyclic case (77.9°, 65.8°). This effect though is to be expected as the TS has become more dissociative. As we have seen previously, electronic deactivation of the 5-*exo* reaction center could result in selective formation of the 6-*endo* trajectory. If the template was inducing an electron withdrawing effect on the reaction center we would expect that the position of the leaving group in the TS shift closer to the reaction center to prevent an increase in unfavorable charge build up (**Figure 21**).

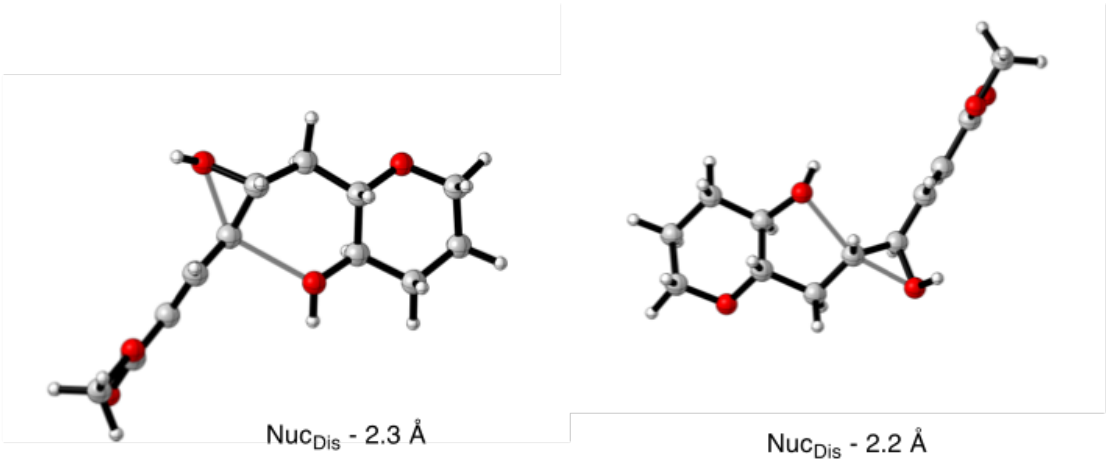

Figure 21. CPCM-M06-2x/6-31G(d,p) competing TSs for ring closure with an ⟨-® unsaturated ester steering group and a pyran template.

When we compared the 5-*exo* TS, the template increased the epoxide C-O bond distance by 0.02 Å. From the deactivation theory we would not expect to be the case. Deactivation of the nucleophile is also possible but again we see the opposite trend, the

nucleophile position reflects an early TS, which is unexpected. What is possible though is that the thermodynamics of the reaction have changed, i.e the products energies have become more stable and the difference between the 5-*exo* and 6-*endo* have increased (**Table 7).** This would result in a more exothermic reaction, shifting to an earlier TS which would help explain the optimized structures.

Case	Product ⊗⊗E_{rxn} (kcal/mol)	Favored Product
Acyclic	2.4	6-*endo*
Template	11.7	6-*endo*

Table 7. Thermodynamic difference between tetrohydropyran and furan with and without the template.

By comparing the product energy differences between the tetrahydropyran and tetrahydrofuran product with the introduction of the template we indeed find that the 6-*endo* product is becomes more stable with the introduction of the template by 9.3 kcal/mol relative to the acyclic case. From our results it would appear that the TS position plays a significant role in the stability of the 6-*endo* TS and template impacts the 6-*endo* selectivity through modulation of thermodynamics.

2.2.3 6-*endo*-selective closure of silylated epoxides

Jamison *et al.* developed an elegant approach, to 6-*endo* selective closure, by using a "traceless" directing group at the position where attack is desired. A trimethylsilyl (TMS) directing group was used for this purpose (**Figure 22**). Initially discovered in 2002, this methodology, coupled with classic aliphatic chain extension using alkyne couplings, resulted in a rapid approach to generate the ladder polyether core.

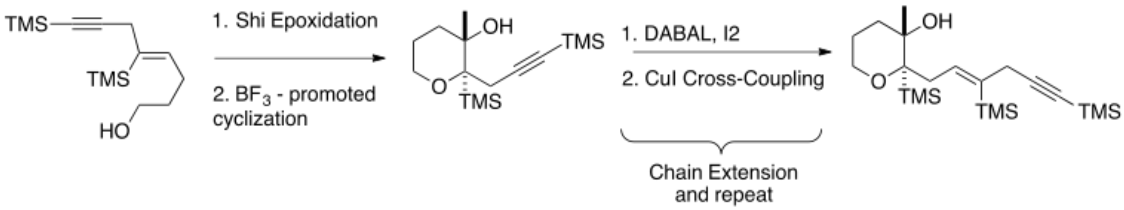

Figure 22. Jamison's approach to ladder polyether formation via 6-*endo*-selective epoxide closure.

Under Lewis acidic conditions, Jamison found that the 6-*endo* reaction was favored with 95:5 selectivity (THP:THF). This is perhaps a surprising result, since the trimethylsilyl group increases the steric demands associated with nucleophilic attack to form the pyran ring. Additionally, based on the logic which successfully accounts for the control exerted by an allylic substituent, a silyl group would be expected to stabilize ®-carbocationic character at the position corresponding to THF formation. Intrigued by these results, we investigated why the reaction displays pronounced 6-*endo* selectivity. We summarise the relevant stereoelectronic effects in **Figure 23**.

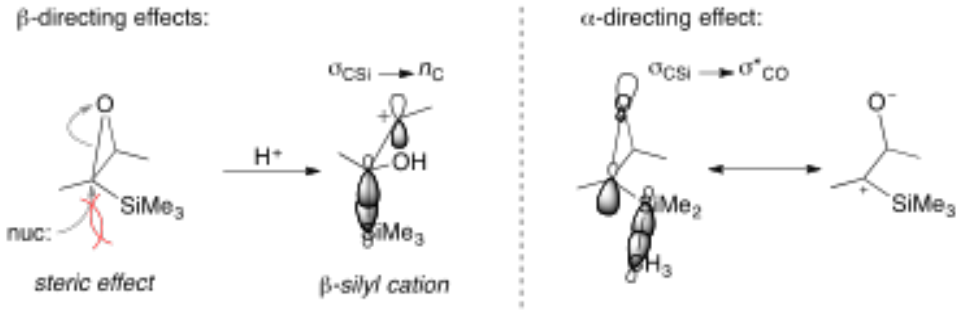

Figure 23. Competing steric and stereoelectronic influences of a silyl substituent upon epoxide opening.

The TMS-directed cyclization was promoted experimentally by a Lewis acid, BF_3. We explicitly modeled the BF_3 coordinated to the epoxide, at the M06-2x/6-31 G(d,p) level of theory in CPCM dichloromethane. This methodology was utilized to the locate and optimize the TSs and GSs for the respective trajectories. Our calculations predict the 6-*endo* ring-opening trajectory is favored by 5.3 kcal/mol. Although qualitatively correct, this value is larger then that obtained in experiment (1.3 kcal/mol) as shown in **Table 8**.

TS	\O···C-C (°)	d_{Nuc} (Å)	d_{Lg} (Å)	⊗⊗$E^{‡}$ (kcal/mol)
5-*exo*	103.7^{0}	2.0	1.9	5.3
6-*endo*	96^{0}	2.2	2.0	0

Table 8. Characterization of the TSs for ring closure with a trimethylsilyl steering group.

Coordination of the Lewis acid to either oxygen lone-pair of the epoxide was considered, and we have focused on the most stable TS for each pathway. In the 5-*exo* TS we can see that there are significant unfavorable steric interactions; 1,3 allylic strain and BF_3 steric interactions originate from the TMS group (**Figure 24**).

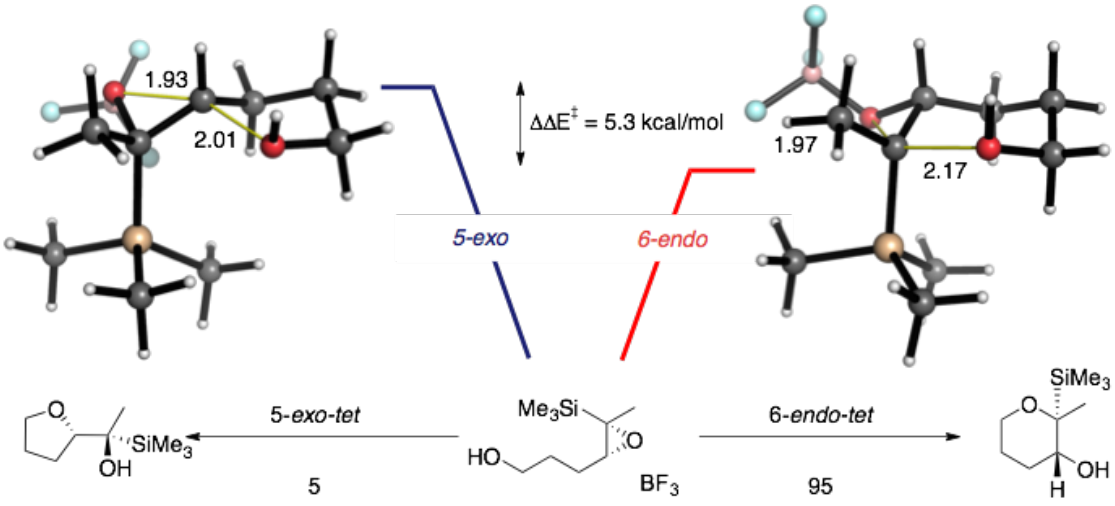

Figure 24. CPCM-M06-2x/6-31G(d,p) competing TS structures for the Lewis acid promoted cyclization of a silylated epoxide.

In the 6-*endo*-TS the approach angle is 96° while the 5-*exo* approach angle is 103.7°. This significant increase in the approach angle for the 6-*endo* TS is also reflected in the more product like TS. In the 6-*endo* TS we find that one of the Si-C bonds in the TMS-group is aligned to be antiperiplanar with the C-O ∫* anti-bonding orbital. This is

consistent with donation from the Si-CH_3 bond weakening the adjacent C-O bond, although optimized bond lengths did now show lengthening due to their weakening from hyperconjugation. This could mean that hyperconjugation is relatively insignificant, and that the electronegativity difference between silicon and carbon stabilizes substitution at the adjacent position. In the 5-*exo* TS we can see that the methyl groups from the TMS and the C_5-C_6 bond are nearly eclipsing. This eclipsing interaction results from steric interactions between the BF_3 and TMS. We illustrate these interactions in **Figure 25**: steric interactions were gauged from NCI (non-covalent interaction) analysis of the electron density. This approach uses the gradient of the electron density to highlight regions of weak interactions, such as steric or Van der Waals interactions.[39]

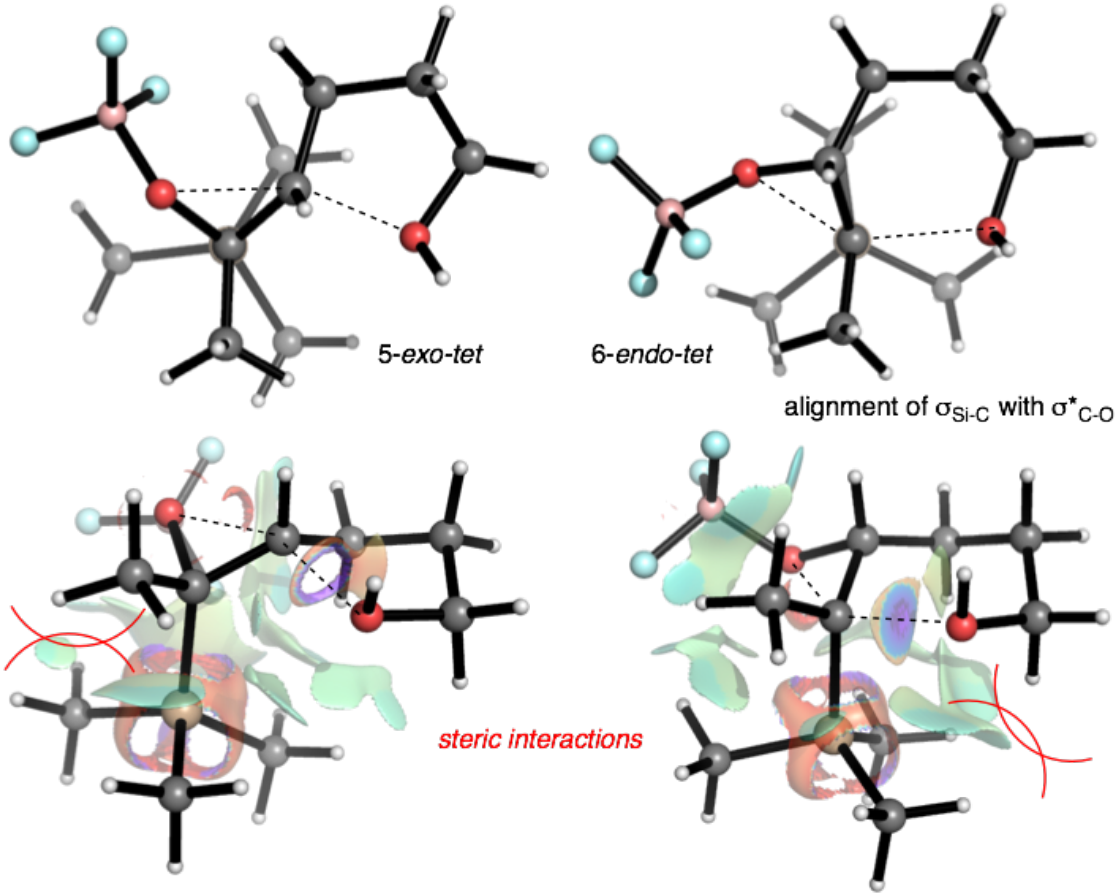

Figure 25. 5-*exo* and 6-*endo* TS structures and key stereoelectronic and steric interactions.

A significant difficulty in fully quantifying the inherent driving force for TMS directing group is the strong steric clash between the TMS and BF_3, which is highly dependent on the trajectory. To obtain an understanding of the stabilizing affect of the TMS we decided to compute the reaction under Brønsted acidic catalysis. Jamison and co-workers did not report results for an acid promoted cyclization, although we felt this would give insight into the relative contributions of electronic and steric interactions. From these calculations it would appear that the 6-*endo* selectivity decreased because the TS became earlier. We find that the nucleophile position for the 6-*endo* trajectory had decreased by 0.17 Å and the leaving group decreased by 0.07 Å relative to the BF_3 promoted reaction. This earlier TS resulted in a less favorable approach trajectory, which could help explain the drop in the 6-*endo* selectivity. For the 5-*exo* TS we find that with the removal of the steric clash in the Brønsted model the TMS group adopts a more staggered conformation; 16.8° to 42.3° (for BF_3 and H^+ activation respectively).

In both models the 5-*exo* TS is unable to adopt the necessary conformation to induce any ∫ bond overlap from the C-Si bond with a developing carbocation. From our TS structures we found that the C-Si TMS bond distance was the same for both the 5-*exo* and 6-*endo* TSs in both models which solidifies the idea that the electronegativity difference with the TMS is not stabilizing the reaction center. We believe that the TMS group is able to stabilize the charge build up through hyperconugation as the 6-*endo* TS structure shows the necessary conformation for the interaction.

TS	$\backslash_{O\cdots C\text{-}C}$ (°)	d_{Nuc} (Å)	d_{Lg} (Å)	⊗⊗$E^{‡}$ (kcal/mol)
5-*exo*	100.7	1.9	1.8	2.4
6-*endo*	89.5	2.1	1.8	0

Table 8. TS approach trajectory and relative stability of Brønsted-acid promoted cyclization of silylated epoxides.

By altering the reaction conditions from acidic to basic, Jamison and co-workers found that only the 6-*endo*-*tet* cascade product was formed; starting with a template already present. This is unusual as one would expect that hyperconjugation by TMS would

stabilize the build up of positive charge (as in the Lewis or Brønsted acid promoted case), but under basic conditions we would not expect this to be as significant. Our calculations found that for the acyclic species (i.e. without a template), the 6-*endo* trajectory is favored by only 0.9 kcal/mol; as there are no experimental results we have no data to make a comparison against (**Figure 26**).

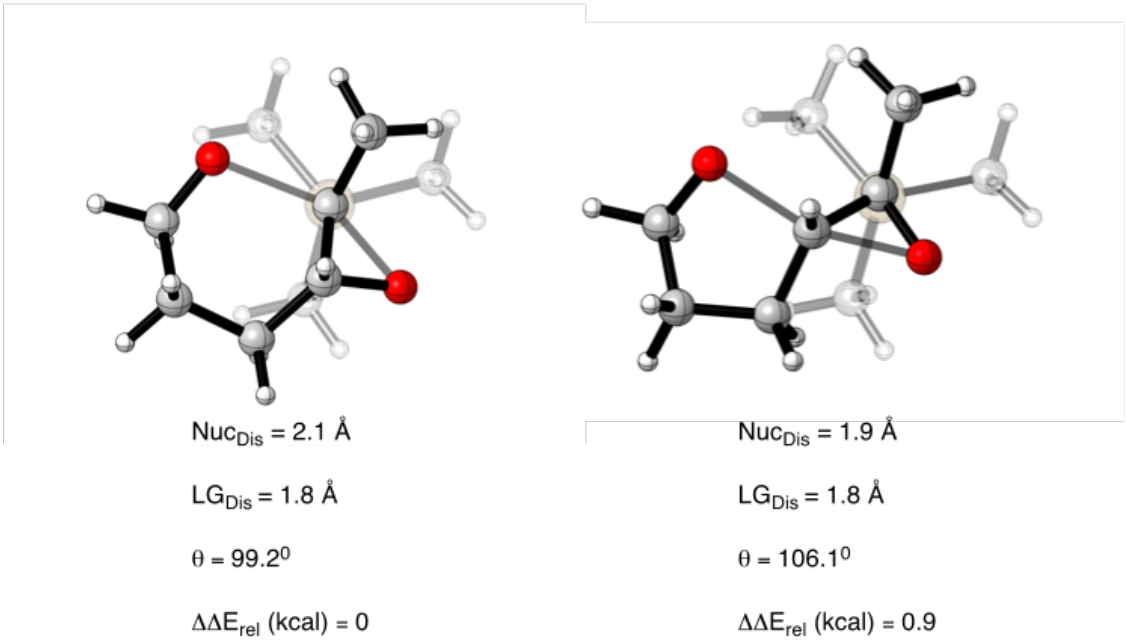

Figure 26. TS difference between the 6-*endo* and 5-*exo* TSs under Brønsted base conditions.

The TS in this case has become more associative relative to the Brønsted acid-promoted reaction with the nucleophile approaching closer to the reaction center by 0.22 Å and the leaving group distance decreasing by 0.11 Å. The approach angle for the 6-*endo* TS has increased by 3° to 99° but this slight improvement in the trajectory is made redundant by a similar improvement in the 5-*exo* trajectory. Structurally, the TS structures for both THP and THF formation show close similarity to the earlier acid-promoted example. The erosion of selectivity computed does support the earlier idea that hyperconjugation is important: in the base-promoted reaction, there is less build of positive charge at the reaction center in the 6-*endo* TS, and so the gap between the two structures is decreased relative to the Lewis/Brønsted acid promoted reaction.

Experimnetally, the template is normally in place before cyclization occurs. To see how the template affects the product distribution we investigated the first cyclization following its introduction. From our calculation swe found that the selectivity for the 6-*endo* reaction course increased to 2.3 kcal/mol resulting the 6-*endo* product being the only observed product from the reaction (**Figure 27**).

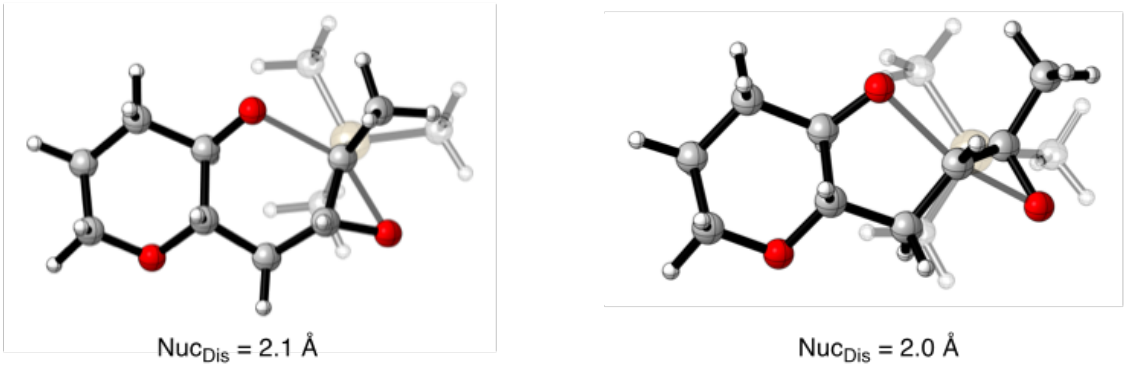

Figure 27. TS comparison between 6-*endo* and 5-*exo* under Brønsted base conditions with a template.

Unlike the allylepoxide, the 6-*endo* reaction TS did not change with the introduction of the template. The 5-*exo* TS only changed slightly with the structure becoming more dissociative. The increase in 1.4 kcal/mol difference may have been a result from the thermodynamic change that we have seen with previous examples. When we compared the difference between the acyclic and template products we again found that the template increased the difference in energy between the *endo* and *exo* products (**Table 9**).

Case	Product ⊗⊗E_{rxn} (kcal/mol)	Favored Product
Acyclic	6.4	THP
Template	11.1	THP

Table 9: Thermodynamic difference between tetrahydropyran and furan in the presence of a pre-formed tetrahydropyran core.

2.2.4 Rationale for Substrate Controlled Regioselectivity

We considered the optimized structures and LUMOs for neutral and protonated epoxides bearing the two directing groups investigated above at the same level of theory (**Figure 28**). Firstly, in the protonated case (which serves as a model for both Lewis and Brønsted acid activation mechanisms) the structures and LUMOs reinforce our previous dicussions in terms of C-O weakening. For ethylene oxide, protonation leads to a symmetrical lenghening of the C-O bonds by 0.08Å as they weaken. In the substituted cases, the lenghening is unsymmetrical: with an allyl group the adjacent C-O bond lenghtens more by 0.14Å than the other C-O bond, and with a silyl group more a similar effect is observed, this time by 0.06Å. At the same time, the nature of the LUMO reflects this trend: for both cases the larger coefficient is at the carbon adjacent to the allyl/TMS group. Attack is therefore preferred at this position. In the neutral epoxides, there is a much smaller asymmetry in both structure and LUMO. However, these are distorted in the same way, with longer C-O bonds adjacent to the substituent. Interestingly, the difference in C-O bond lengths is larger for the neutral silylated epoxide than for the allyl epoxide.

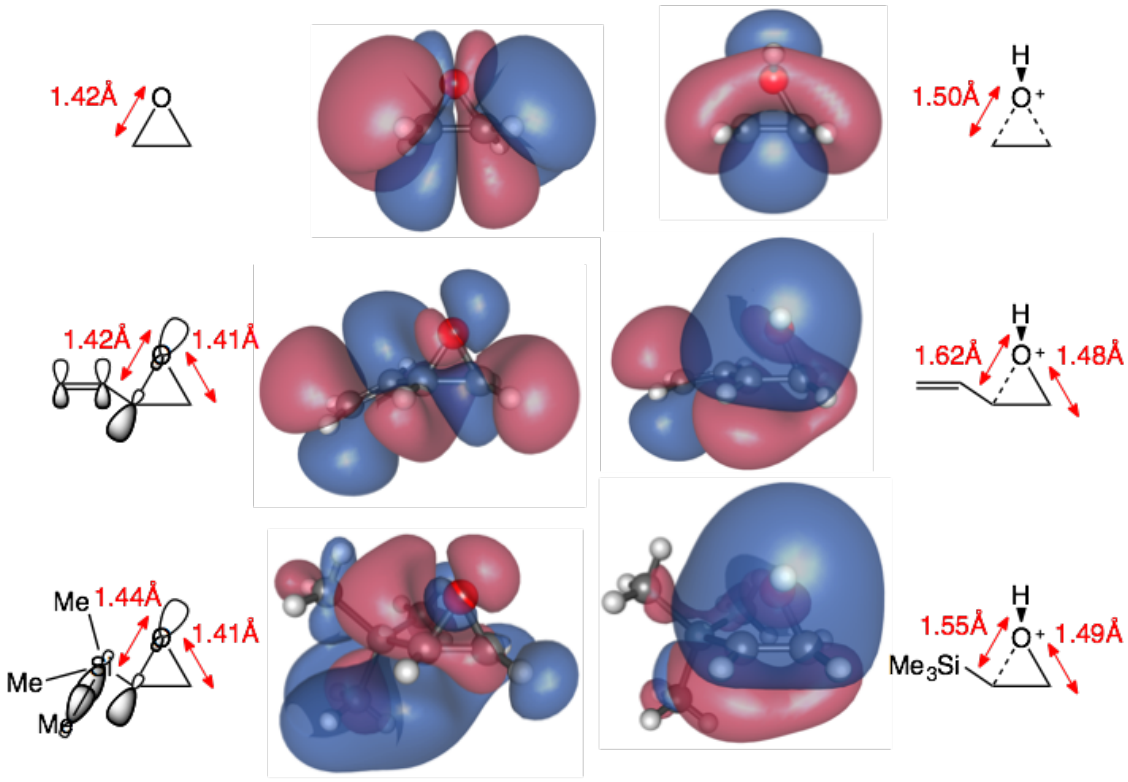

Figure 28. M06-2X/6-31G(d,p) optimized reactant geometries and LUMOs for neutral and protonated epoxides with different substituents.

From the studies performed on the classic reaction techniques as well as the conformational studies for the solvent models we have that electronics, TS position and thermodynamics can play a significant role in determining the product distribution. With this information in hand though it is still difficult to correlate the TS position, mechanism (dissociative) and thermodynamic effect. As we have seen in the Brønsted base reaction model for the *trans*-4,5 epoxyhexanol the position of the TS is later then that of the Nicolaou reaction. As we know from Hammond postulate the later the TS position the more physical characteristics that it will share with the product. The Nicolaou reaction showed the most significant change in the thermodynamic with the introduction of the template (9.3 kcal/mol) but this only resulted in a 1.3 kcal/mol increase in the TS difference. On the other hand, the Jamison model only showed a 4.7 kcal/mol increase with the induction of the template but a 1.4 kcal/mol increase in the difference between the TSs. These results highlight that the position of the TS is able to mitigate the impact of the thermodynamic influence.

2.3 Regioselectivity in templated epoxide opening cyclizations

2.3.1 Template Effect

Jamison *et. al.* in 2007 introduced a THP template into their reaction design to explore its effect upon subsequent ring closures in water. From this and subsequent studies, they found that the greater the number of heteroatoms in the template ring the greater the 6-*endo* regioselectivity and the more robust the selectivity was to changes in pH. In Jamison's initial study it was argued that the template was explicitly involved in the controlling the reaction though its interactions with the solvent which would result in a twist-boat conformation. This conformational shift was argued to induce an improved trajectory approach that would result in a more favored 6-*endo* reaction. Our calculations have shown that even though the twist-boat induces a favorable approach trajectory (6° relative to chair conformation) this is outweighed by the unfavorable thermodynamic effect and increased activation barrier associated with the less stable conformation.

As we have seen in our previous calculations the introduction of the template induces an increase in the thermodynamic discrimination between the furan and pyran ring formation. To investigate the templates interactions with water we decided to focus our investigation on the derivatives of the template under both neutral and Brønsted acidic conditions. The same computational methodology that was developed in the preceding section was adopted.

2.3.2 Tetrahydropyran template

Before investigating the possible effects of the template on the rate of reaction we sought to understand the effects of the THP core on the first cyclization step. From our calculations (**Figure 29**) we found that the predicted selectivity for the cyclization product distribution was 20:1 versus 11:1 ($\otimes\otimes TS_{(6\text{-}5)}$ -1.94 kcal/mol) found experimentally. With the marginal error we believed that the results and subsequent structures generated would give an accurate interpretation on the effect of template.

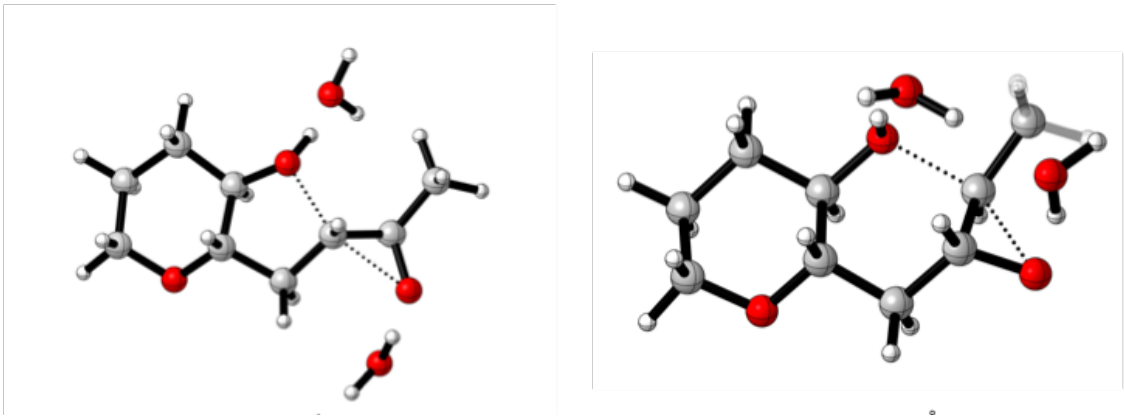

Figure 29. CPCM-M06-2X/6-31G(d,p) TS structural difference between 5-*exo* and 6-*endo* TS promoted by water, with a THP template effect.

The 5-*exo* TS became more dissociative relative to the acyclic case but the trajectory increased by 4°. For the trajectory to improve for this mechanism we would expect that the TS has become later. The 6-*endo* TS has not changed drastically with the induction of a THP template.

Template	**Conditions**	**TS**	$\backslash_{O\cdots C\text{-}C}$ (°)	d_{Nuc} (Å)	d_{Lg} (Å)
THP	Neutral	5-*exo*	110.1	1.87	2.02
		6-*endo*	101.4	1.92	2.00

Table 10: Further characterization of the TS for tetrahydropyran template in water.

Introduction of a second THP template was considered computationally, and resulted in a further increase in 6-*endo* selectivity, giving a predicted selectivity of 34:1 (THP:THF) (⊗⊗$TS_{(6\text{-}5)}$ -2.45 kcal/mol). Experimentally Jamison and co-workers found a selectivity increase to 19:1 (THP:THF) with this modification, so our calculations were able to reproduce the trend in selectivity with good accuracy (**Figure 30**).

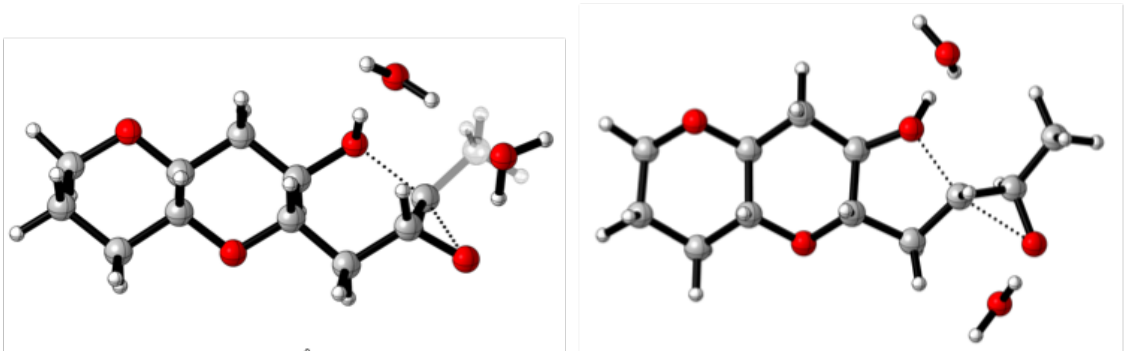

Figure 30. CPCM-M06-2X/6-31G(d,p) TS structural difference between 5-*exo* and 6-*endo* TS promoted by water, with a *trans*-fused bis-THP template effect.

Our TS calculations found that the bicyclic THP template increased the dissociative nature of the 5-*exo* TS to a greater extent than for 6-*endo*. The trajectory for both cases increased slightly over that of the monocyclic THP template. The separation between the product energies increased slightly by 0.1 kcal/mol (11.4 *vs* 11.3 kcal/mol; bi- and monocyclic templates, respectively), which would not account for a pronounced increase in selectivity.

Template	**Conditions**	**TS**	$\angle_{O\cdots C\text{-}C}$ (°)	d_{Nuc} (Å)	d_{Lg} (Å)
BI-THP	Neutral	5-*exo*	111.1	1.85	2.04
		6-*endo*	101.5	1.91	2.01

We were intriguied by the possibility, that rather than inducing a conformational effect, an important role of the templates was to influence the reaction center by a withdrawl of electron density through the sigma-framework. This would lead to greater charge separation in the TS by deactivating the nucleophile. As Jamison and co-workers have already shown, the discriminaton between 5-*exo* and 6-*endo* is greatly affected by the entropic barrier for the reaction. From our TS calculations we found that the TS does indeed become later, i.e. more dissociative. We would expect that charge separation in the TS has increased relative to the GS to a greater extent in the bicyclic-template

versus that of the single pyran. This effect was probed by NBO calculations on the structures to obtain natural charges for each TS (**Table 11**). We observed that the charge separation within the reaction center increases with the introduction of the template. This effect though is localized to the 5-*exo* TS and does not affect the 6-*endo* TS. Additionally, the greater charge separation for the 5-*exo* TS would also be expected to cause more pronounced solvent reorganization, which would contribute to an entropic factor disfavoring THF formation.

Template	Trajectory	LG Charge (e)	Nuc Charge (e)	Charge Separation (e)
Bis-THP	6-*endo*	-0.11	0.23	0.34
	5-*exo*	-0.12	0.26	0.38
THP	6-*endo*	-0.11	023	0.34
	5-*exo*	-0.12	0.25	0.37

Table 11. Analysis of the charge build up different between the TSs with different template structures to promote the discrimination.

Our initial calculations highlighted that introduction of a THP template increased the 6-*endo* selectivity by increasing the thermodynamic difference between the THP and THF products. This thermodynamic effect, however, is approximately constant for a mono- or bicyclic template. The additional selectivity gained from the longer template instead results in a slightly later 5-*exo* TS, which we hypothesize is the result of an enhanced inductive affect on the reaction center. The greater charge-separation in the 5-*exo* TS is a direct effect of being slightly later, and could also result in more (unfavorable) solvent organization versus 6-*endo*-TS.

2.3.3 Cyclohexyl template

Following observations with the THP template, Jamison and co-workers reported results with a cyclohexyl derivative as the template. It was found that the cyclohexane template, unlike the tetrahydropyran motif, displayed a first order dependence on the solvent for the 6-*endo* reaction course. Utilizing the two water model that we had developed previously we find that the predicted selectivity is 1.2 :1 (THP:THF) (⊗⊗$TS_{(6\text{-}5)}$ -0.24 kcal/mol) while the experiment shows 1 : 1.4 selectivity (**Table 12**). If we compare 5-*exo* TS with a cyclohexyl template versus the 4,5 epoxyhexanol we find that the reaction has become more associative, the forming bond distance is 1.87 Å vs. 1.92Å; cyclohexane and no-template respectively and is also true relative to the pyran template. The 6-*endo* TS on the other hand shows similar structural characteristics to the un-templated reaction.

Template	**Conditions**	**TS**	$\angle_{O\cdots C\text{-}C}$ (°)	d_{Nuc} (Å)	d_{Lg} (Å)
Cyclo	Neutral	5-*exo*	105.6	1.87	2.03
		6-*endo*	100.9	1.92	1.99

Table 12. TS characterization utilizing the standard water bridging template.

We would expect from these results that the 5-*exo* should be the dominant product and display a distribution greater then that of the epoxyhexanol case. The introduction of the template induces greater selectivity for the 6-*endo* product. With the introduction of the cyclohexane motif we find that the tetrahydropyran template is more stable by 6.3 kcal/mol relative to the single pyran case. This combination could be a possible explanation for why we find that the 6-*endo* trajectory is more stable then the 5-*exo* trajectory. This argument though is highly dependent on the model that we had chose initial. As we have discussed already, the cyclohexane displays a first order dependence on the solvent. As our model is trying to replicate the second order dependence we

deiced to break the solvent bridge for the 6-*endo* model and utilize the same non-solvent bridge model that we utilize for the 5-*exo* TS.

With the alteration of the 6-*endo* TS we find that experimental outcome 1 : 1.2 is nearly matched by our model, 1 : 1.6 (*endo* : *exo*). When we investigate the new 6-*endo* TS we find that the trajectory has improved by 3° and the position of the nucleophile has remained unchanged. We find that in this model, the distance of the breaking C-O bond in the TS has decreased by 0.03 Å to produce a more associative TS relative to the solvent bridging model (**Table 14**).

Template	**Conditions**	**TS**	$\backslash_{O\cdots C\text{-}C}$ (°)	d_{Nuc} (Å)	d_{Lg} (Å)
Cyclo	Neutral	5-*exo*	110.1	1.87	2.01
		6-*endo*	101.1	1.92	1.96

Table 14. TS characteristics utilizing novel solvent model Figure 33.

2.3.4 Dioxane template

At the opposite end of the 6-*endo* selectivity spectrum from cyclohexyl is the dioxane template which had displayed the greatest selectivity across the most diverse conditions 128: 1 and 7: 1 (THP:THF) ($\otimes\otimes TS_{(6\text{-}5)}$ -4.82 kcal/mol, $\otimes\otimes TS_{(6\text{-}5)}$ -0.23 kcal/mol) under neutral and acidic conditions. The dioxane template displayed the classic general acid/base pH response curve, a double hump characteristic of discrete molecules acting as an acid or base. This made us believe that even though that the kinetics dependence on the solvent was unknown we could apply the tetrahydropyran model and methodology to this investigation. Our initial calculations focused on the epoxide cyclization under neutral conditions which displayed a product distribution of 130:1 (*endo* : *exo*).

Template	**Conditions**	**TS**	$\backslash_{O\cdots C\text{-}C}$ (°)	d_{Nuc} (Å)	d_{Lg} (Å)
Dioxane	Neutral	5-*exo*	110.7	1.84	2.05

	6-*endo*	102.1	1.91	2.03

Table 15. TS Characteristics of the Dioxane template under classic solvent model.

In the optimized TSs we found that the nucleophilic approach trajectory has an improved approach trajectory for the 6-*endo* TS when compared with the cyclohexane derivative, but it is similar to that computed with a THP template. The 5-*exo* TS on the other hand has a similar trajectory with the cyclohexane template. However, comparison of the distances for the forming and breaking C-O bonds become shorter and longer, respectively. The 5-*exo* TS is more dissociative relative to both the tetrahydropyran and cyclohexane template. The 6-*endo*-TS has become more dissociative as well but alterations to the bond distances are much less significant. The thermodynamic difference in the THP and THF product stablities is decreased by 1.4 kcal/mol relative to the THP-template. This significant shift in the selectivity with a decreases in the thermodynamic difference is rather surprising. To explore this case further, we decided to investigate the Brønsted acid promoted 6-*endo*-*tet* reaction with a dioxane template.

Utilizing the Brønsted model we found that the predicted outcome from our calculations was a 1.4 : 1 versus that of the 7: 1 , *endo* : *exo*, found experimentally. Even though there is error in our predications we believe that the structures generated could still be useful (**Table 16**).

Template	Conditions	TS	$\backslash_{O\cdots C\text{-}C}$ (°)	d_{Nuc} (Å)	d_{Lg} (Å)
Dioxane	Acidic	5-*exo*	104.6	2.16	1.90
		6-*endo*	95.1	2.21	1.87

Table 16. TS Characteristics of the Dioxane template under Brønsted acid conditions.

As we would have expected from our earlier calculations, the TS has become significantly earlier relative to the neutral cases. The significant difference is that the TS has become later relative to both the acyclic and tetrahydropryran Brønsted acid cases. The shifts to a later TS for both the neutral and acid model could result from the deactivation of nucleophile. Jamison and co-workers discussed briefly the possibility that the electronegative nature of the ring was inducing the 6-*endo* selectivity but dismissed this proposal based on their results from a cycloheptyl template.

2.4.5 Cycloheptane Template

Jamison and co-workers developed a cycloheptyl templated reaction, for which it was anticipated that the skew-boat conformation would not be accessible. As this motif contained the *endo*-cyclic oxygen it may also serve as a probe for the effect of deactivation of the nucleophile upon the regioselectivity. Experimentally, it was found that the cycloheptane template induced a 1:3 selectivity, in favor of the THF product. From our calculations utilizing a bridging water motif, we found that the selectivity was 1:12 in favor of the THF product. The shift to 5-*exo* was reflected in our results so we believed that we could utilize the structures to determine the origin for the shift (**Table 17**). The 5-*exo* TS has become more earlier and more associative with the epoxide shorting its bond distance relative to the other templates. This initial result would give some credence to the hypothesis that the endocyclic oxygen has a limited effect on the selectivity. Nevertheless, this template also leads to a difference in product stabilities, which we have seen influences the selectivity of ring-opening. From our calculations we found that the thermodynamic preference for the THP product lessened by 2.5 kcal/mol relative to a THP template. Even without alteration of intrinsic activation barriers, we would expect this thermodynamic effect to lead to a shift towards THF formation.

Template	Conditions	TS	Angle	Nuc $_{Dis}$	LG $_{Dis}$
Cycloheptane	Neutral	5-*exo*	109.8	1.86	1.99

	6-*endo*	98.8	1.92	1.99

Table 17. TS Characteristics of the Cycloheptane template under classic solvent model.

2.4 Environmental interactions

2.4.1 Electronic Effects

From our results thus far we have found that the position of the epoxide-opening TS and its structure have a significant impact on the selectivity of the reaction. We have computed the differential stabilities of the THF and THP products for different templates in different conditions and, as expected, the THP dominates, although by differing amounts depending on the system considered. While thermodynamics has an effect, mainly through the position of the TS, there is no simple correlation between these thermodynamic energy differences and experimental selectivies. (**Table 18)**.

Template	Conditions	Favored Product	⊗E (kcal/mol)
Dioxane	Neutral	6-*endo*	9.9
	Acid	6-*endo*	6.2
THP	Neutral	6-*endo*	11.3
	Acid	6-*endo*	7.2
Cyclohexane	Neutral	6-*endo*	9.6
Cycloheptane	Neutral	6-*endo*	8.8

Table 18: Relative Product stability difference with the varying templates

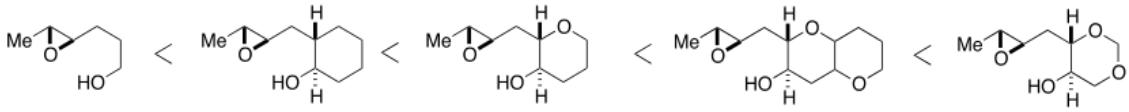

Figure 31. 6-*endo* product selectivity trend observed experimentally.

As stated previously the dissociative nature of the TS seems to correlate with lower stability, and is often observed for the 5-*exo* TS leading to 6-*endo* selectivity. Utilizing Wiberg Bond Orders (WBOs) we have compared the extent of bond breaking and bond formation in the different TS structures (**Table 19**). This provides additional detail beyond the length of these bonds in the structures.

Template	Conditions	TS	$\angle_{O\cdots C\text{-}C}$ (°)	B_{Nuc}	B_{Lg}
Dioxane	Neutral	5-*exo*	110.7	0.60	0.65
		6-*endo*	102.1	0.60	0.61
	Acid	5-*exo*	104.6	0.19	0.45
		6-*endo*	95.1	0.13	0.45
THP	Neutral	5-*exo*	110.1	0.65	0.62
		6-*endo*	101.1	0.60	0.57
	Acid	5-*exo*	104.0	0.22	0.42
		6-*endo*	94.2	0.18	0.43

Cyclo	Neutral	5-*exo*	110.1	0.66	0.60
		6-*endo*	101.1	0.61	0.55

Table 19. Bond Formation in the transition state for the respective transition state.

From these results we can see that as the electronic density of the ring is depleted with the introduction of the *endo*-cyclic oxygens and as a result, the 6-*endo* TS becomes more dissociative; (B_{Nuc} 0.61 and 0.6 for cyclohexane and pyran respectively) and (B_{lg} 0.55 and 0.57 respectively). The dioxane TS from this analysis has changed very little when compared to the pyran template. The most significant impact of the electronic perturbation is on the 5-*exo* TS where we can see that the leaving group bond breaking increase by 0.05 Å and the nucleophile bond formation decrease by 0.06 Å as we shift between the cyclohexane and dioxane templates. As Jamison and co-workers have highlighted, water is able to help discriminate between the reaction trajectories based on entropic effects. From the TS structure we would expect that as the TS becomes later and more dissociative, charge separation will increase. The charge could induce solvent re-organization around the TS resulting in the unfavorable entropic effect, particularly for the 5-*exo* TS.

To investigate this possibility we have computed the natural charges at the reaction center of the GS and TS structures. The relative difference allowed us to calculate the charge separation (**Figure 32**). I chose to utilize this approach instead of the dipole moment as I believe that if we treated the solvent as explicit rather then implicit we would find that the solvent would recognize the charged separated groups as discrete entities versus a global vector.

Template	Conditions	TS	Angle	CS (e)	⊗
Dioxane	Neutral	5-*exo*	110.7	0.39	0.4
		6-*endo*	102.1	0.35	

THP	Neutral	5-*exo*	110.1	0.38	0.3
		6-*endo*	101.1	0.35	
Cyclo	Neutral	5-*exo*	110.1	0.37	0.2
		6-*endo*	101.1	0.35	
Bi-Template	Neutral	5-*exo*	109.8	0.38	0.3
		6-*endo*	98.8	0.35	

Table 19. CS = Charge Separation in the transition state as shown in Figure 32.

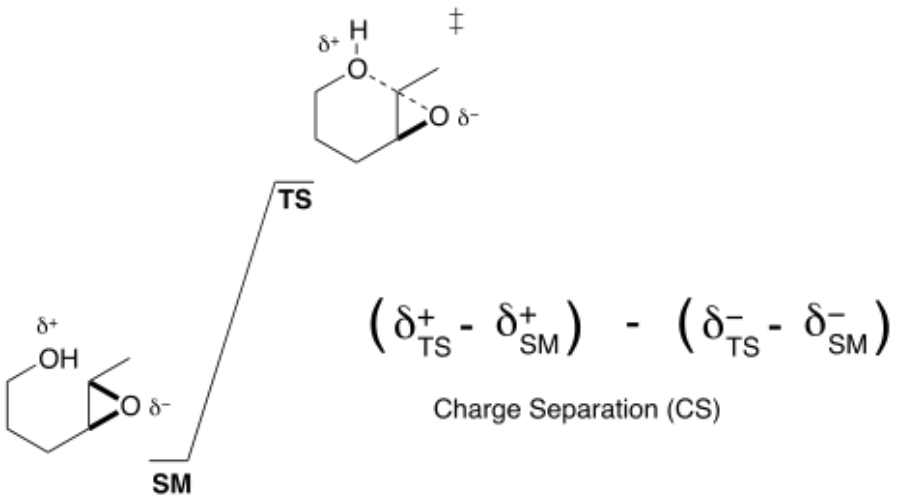

Figure 32. Approach to Calculating the Charge Separation (CS) seen by the environment.

From the charge separation shown in (**Table 19**) it becomes apparent that the TS position influences this quantity, which in turn will affect the first solvation shell around the TS. This contributes an entropic factor to the regioselectivity, which is difficult to compute exactly, although qualitatively we argue that it will be related to the degree of charge separation. Thus far we have found that the templates lead to a thermodynamic improvement for the 6-*endo* trajectory, while changing the electronics of the template result in changes in the solvent organization for the 5-*exo* trajectory.

What we have not discussed thus far is how the electronics of the ring is able to attenuate the position of the TS. To investigate this correlation we will need to determine the inherent characteristics of the reaction potential energy surface.

2.4.2 Epoxide opening Potential Energy Surface (PES)

To better understand the inherent dynamics of the reaction we decided to calculate a More O'Ferrall-Jencks plot of the THP-templated reaction under neutral reaction conditions (**Figure 33**). This plot is traditionally generated through the investigation of the linear free energy relationships and provides the researcher information on the interdependence of interactions for a given reaction. To emulate this approach we calculated a grid for the reaction coordinate, where the two coordinate directions were the forming and breaking C-O bonds. All other geometric coordinates were fully optimized while these two coordinates were incremented systematically to generate a 3-dimensional energy surface showing the saddle point (i..e TS structure) and the region around it on the PES. The distances were scanned over the range (3.0 – 1.5 Å for the nucleophile and 1.5 – 2.3 Å for the epoxide; with grid spacing of 0.1 Å) at the M06-2x/6-31G(d,p) level of theory as used previously in this chaper. For this investigation we utilized the most thoroughly investigated system, the THP-templated reaction in water. The surfaces are represented as contour plots for with isocontours every 5 kcal/mol: a rainbow color scheme shows low energies in violet and high energies in red.

(A)

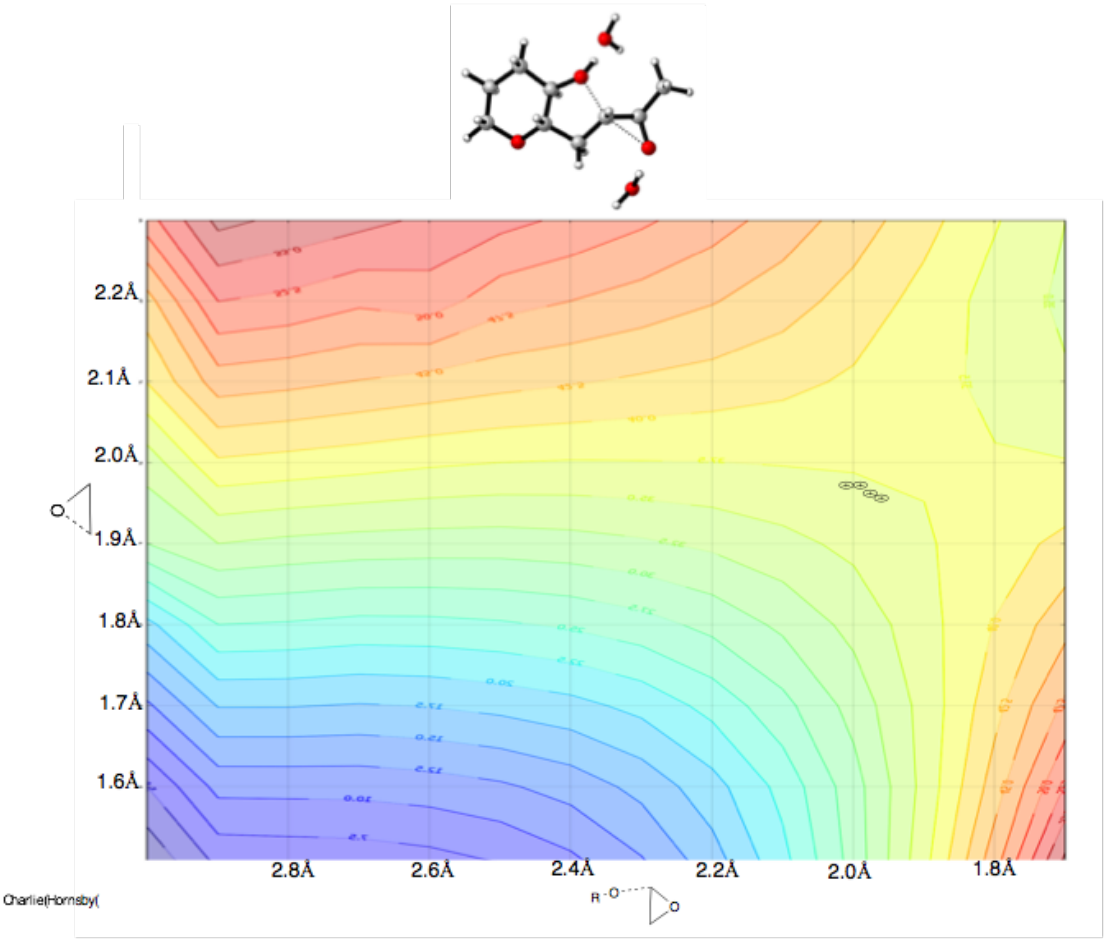
2.2Å
2.1Å
2.0Å
1.9Å
1.8Å
1.7Å
1.6Å
2.8Å
2.6Å
2.4Å
2.2Å
2.0Å
1.8Å
Charlie(Hornsby(

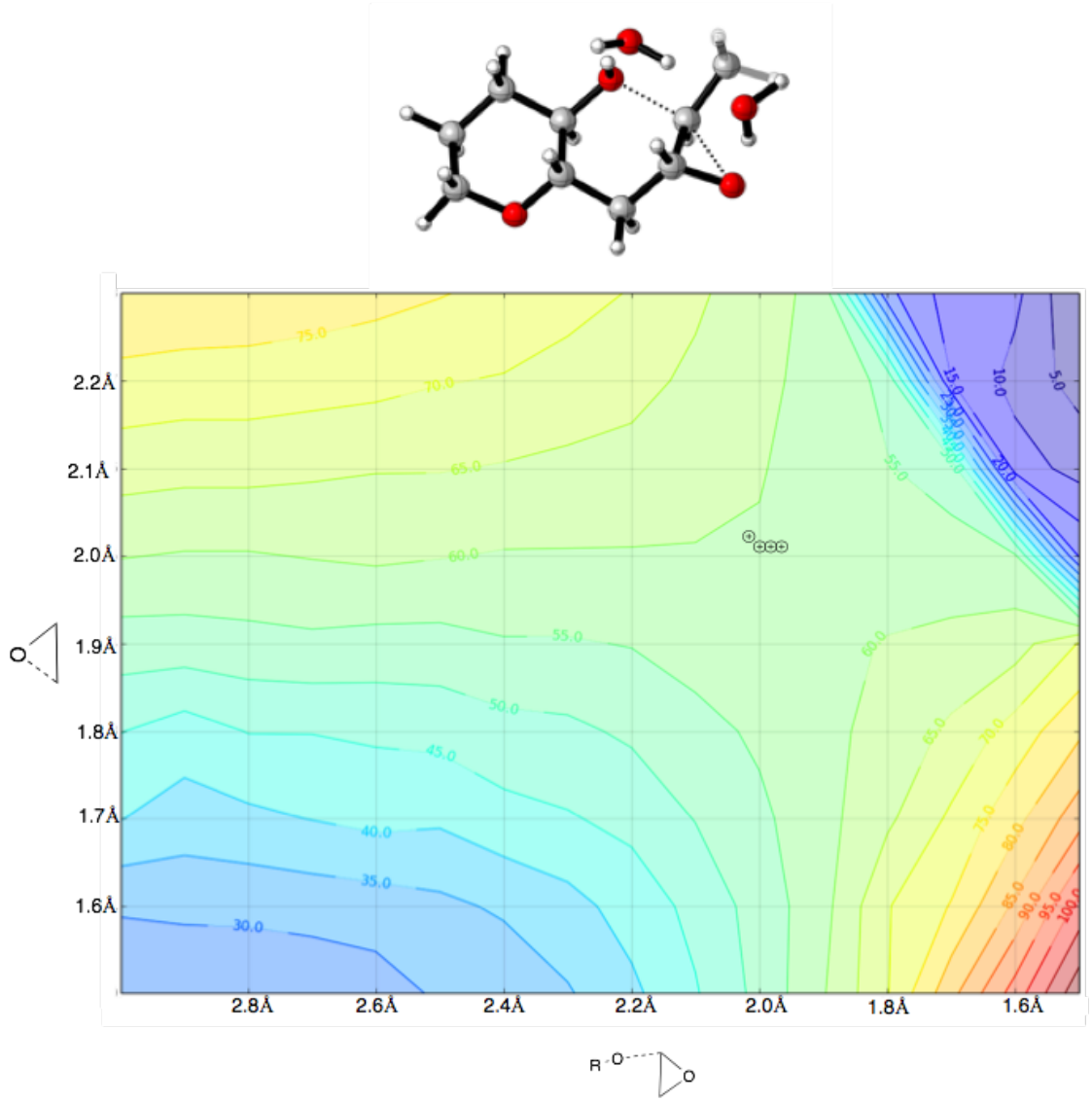

Figure 33. Potential Energy surface for the tetrahydropyran template. X marks on graphs highlight the TS position of the cyclohexane, tetrahydropyran, Bi-template and dioxane TSs. Graphic images were prepared using the *MatPlotLib* Python library to interpolate between computed energy values. (A) 5-*exo* reaction profile. (B) 6-*endo* reaction profile.

From the computed Moore O'Ferrall-Jencks plot the effect of having a later transition becomes apparent. It would appear that the 5-*exo* reaction is much more sensitive to alterations of the in the position of the nucleophile and leaving group then the 6-*endo* reaction. For the 6-*endo* TS, the region of the PES around the TS is flatter, and more forgiving of such alterations. By alternating the electronic nature of the template the

chemist is able to control the nucleophilicity of the alcohol which results in a significant shift in the leaving group to adopt the lowest energy reaction course. This effect is less pronounced in the 6-*endo* reaction course but should be fairly pronounced in the 5-*exo* reaction trajectory. When we focused our attention to the 5-*exo* trajectory we indeed find that the TS is much more sensitive to alterations in the electronics of the template.

As we have seen in computed structures, and now in the shape of the PES around the TS, the 5-*exo* TS is sensitve towards perturbation by alteration of electronics or solvent. Changing the TS structure towards a later structure results in greater charge separation, which is itself unfavorable, but also leads to more pronounced solvent ordering around the TS; this entropy effect was highlighted already by Jamison. Attempts to evalute the effect of solvent polarity using implicit solvent models showed no effect upon selectivity. However, the implicit model fails to capture the solvation shell around each TS and so would be inadequate in describing any entropic effects of solvation.

2.5 Conclusions

From our computational results we have established that the regioselective of the epoxide-opening cyclizations are influenced by several factors which influence the transition state. Firstly, electronic effects from a donating substituent such as allyl or trimethylsilyl group weaken the adjacent C-O bond to direct nucleophilic attack at that position, which can be used to select for 6-*endo* closure. In the case of the templates studied, there is a weaker inductive effect at play, but which nonetheless affects the transition state position. For reactions in water, the ability of water to act as a "bridge" avoids unfavorable charge build up in the TS, and this is achieved preferentially for the 6-*endo* pathway. It remains the case that this closure proceeds via a less favorable trajectory in stereoelectronic terms, however, the enthalpic and entropic contributions in water outweigh this. The 5-*exo* pathway was found to be more sensitive to perturbation of template or solvent and as a result was raised in energy relative to the competing ring-closure. In the absence of a template, and with acid or base catalysis the more traditional 5-*exo* pathway remains as the more favorable ring closure.

2.6 References

1. (a) Baldwin, J. E.; *J. Chem. Soc. Chem. Commun*. **1976**, 734.; (b) Gilmore, K.; Mohamed, R.; Alabugin, K. *WIREs Comput. Mol. Sci.*, **2016**, early view.
2. Johnston, C. P.; Kothari, A.; Sergeieva, T.; Okovytyy, S. I.; Jackson, K. E.; Paton, R. S.; Smith, M. D. *Nature Chem.* **2015**, *7*, 171
3. Hotta, K.; Chen, X.; Paton, R. S.; Minami, A.; Li, H. Swaminathan, K. T.; Mathews, I. I.; Watanabe, K.; Oikawa, H.; Houk, K. N.; Kim, C. Y. *Nature* **2012**, *483*, 355
4. Gruber, K.; Zhou, B.; Houk, K.; Lerner, R.A.; Shelvin C. G.; Wilson, I.A. *Biochemistry* **1999**, *38*, 7062
5. Nakanishi, K. *Toxicon* **1985**, *23*, 473
6. Nicolaou, K.C.; Edmonds, D. J.; Bulger, P.G. *Angew. Chem. Int. Ed.* **2006**, *45*, 7134
7. Morten, C.J.; Byers, J. A.; Van Dyke, A. R.; Vilotijevic, I.; Jamison, T.F. *Chem. Soc. Rev.,* **2009**, *38*, 3175
8. Nicolaou, K.C.; Yang, Z.; Shi, G.; Gunzner, J.L.; Agrios, K.A.; Gärtner, P. *Nature* **1992***, 392*, 264
9. Nicolaou, K.C.; Rutjes, F.P.; Theodorakis, E.A.; Tiebes, J.; Sato, M.; Untersteller, E. *J. Am. Chem. Soc.* **1995**, *117*, 10252
10. Nicolaou, K.C., Prasad, C.V.; Somers, P.K.; Hwang, C.K. *J. Am. Chem. Soc.*, **1989**, *111*, 5330
11. Nicolaou, K.C.; Frederick, M.O.; Aversa, R.J. *Angew. Chem. Int. Ed.* **2008**, *47*, 7182
12. Kadota, I.; Jung-Youl, P.; Koumura, N.; Pollaud, Matsukawa, Y.; Yamaoto, Y. *J. Org. Chem.* **1998**, *63*, 6597
13. Aicher, T. D.; Buszek, K. R.; Fang, F. G.; Forsyth, C. J.; Jung, S. H.; Kishi, Y.; Matelich, M. C.; Scola, P. M.; Spero, D. M.; Yoon, S. K *J. Am. Chem. Soc.* **1992**, *114*, 3162
14. Towle, M.J.; Salvato, K.A.; Wels, B.F.; Aalfs, K.K.; Zheng, W.; Seletsky, B.M.; Zhu, X.; Lewis, B.M.; Kishi, Y.; Yu, M.J.; Littlefield, B.A. *Cancer Res*. **2011**, 71, 496
15. Chase, C.E.; Fang, F.G.; Lewis, B.M.; Wilkie, G.D.; Schnaderbeck, Zhu, X. *Synlett* **2013**, *24*, 323

16. Thomas, C.M.; Hothersall, J.; Willis, C.L.; Simpson, T.J. *Nat. Rev. Micro.*, **2010**, *8* , 281
17. Minami, A.; Migita, A.; Inada, D.; Hotta, K.; Watanabe, K.; Oguri, H.; Oikawa, H. *Org. Lett.* **2011**, *13*, 1638
18. Bauer, R.A.; Wurst J.M.; Tan, D.S. *Curr. Opin Chem. Biol.* **2010**, *14*, 308
19. Kulkarni, B.A.; Roth, G.P.; Lobkovsky, E.; Porco, J.A. *J. Comb. Chem*. **2002**, *4*, 56.
20. Vilotijevic, I.; Jamison, T.F. *Science* **2007**, *317*,1189
21. Wang, Z.; Cui, Y.T.; Xu, Z.B.; Qu, J. *J. Org. Chem.* **2008**, *73*, 2270
22. McDonald, F.E.; Wang, X.; Bao, D.; Hardcastle, K. *Org. Lett*. **2000**, 2, 2917
23. Bravo, F.; McDonald, F.; Nelwert, W.; Do, B.; Hardcastle, K. *Org. Lett*. **2003**, 5, 2123
24. Mousseau, J.J.; Morten, C.J.; Jamison, T.F. *Chem. Eur. J.* **2013**, *19*, 10004
25. Byers, J.A.; Jamison, T.F.; *Proc. Natl. Acad. Sci*. **2013**, *110*, 16724
26. Groom, C.; Bruno, J.; Lightfoot, P.; Ward, S. *Acta Cryst.* **2016**, B72, 171.
27. Morten, C.J. Jamison, T.F. *J. Am. Chem. Soc.* **2009**, *131*, 6383-6385
28. Byers, J.A; Jamison, T.F. *J. Am. Chem. Soc.* **2009**, *131*, 6678-6679
29. Ditchfield, R., Hehre, W.J.; Pople, J.A. *J. Chem. Phys.* **1971**, 54, 724
30. Barone, V.; Cossi, M. *J. Phys. Chem. A* **1998**, *102*, 1995
31. Walker, M.; Harvey, A.J.; Sen, A.; Dessent, C.E. *J. Phys. Chem. A.* **2013**, *47*, 12590
32. Vetticatt, M.J.; Singleton, D.A. *Org. Lett.* **2012**, *14*, 9, 2370
33. Hratchian, H. P.; Schlegel, H. B. *J. Chem. Theory and Comput.* **2005**, *1*, 61
34. http://www.ch.imperial.ac.uk/rzepa/blog/?p=10015. Accessed 3rd March 2016.
35. Foster, J. B.; Weinhold, F. *J. Am. Chem. Soc.* **1980**, *102*, 7211
36. Paton, R. S. *Org. Biomol. Chem.* **2014**, *12,* 1717
37. Carey, F.A. Sundberg, R.A. Advanced Organic Chemistry: Part A, 5th edition, Springer: New York, 2007.
38. Weinhold, F.; Carpenter, E. *Plenum,* **1988**, 227.
39. Johnson, E.; Keinan, S.; Mori-Sanchez, P.; Contreras-Garcia, J.; Cohen, A.; Yang, W. *J. Am. Chem. Soc.* **2010**, 132, 6498.

Chapter 3. Stereoselective Spiroketalization of Enol Ethers

3.1 Introduction

3.1.1 Introduction

The enantioselective synthesis of natural products underlies much of medicinal chemistry research. Complex synthetic targets have been successfully synthesized that have allowed the scientific community to introduce novel molecules with applications in both medicine and agriculture. There is a continuing need for enantiopure molecules with significant therapeutic activity in the treatment of microbes and parasites. Modern attempts to discover new compounds have focused on screening chemical libraries to find bioactive lead molecules or those that display synergistic interactions with current treatments.[1,2,3] The chemical libraries utilized in these screens can either be fully synthetic derivatives (heterocyclic) or compounds designed around privileged structures found within nature.[4,5]

Spiroketals are considered a privileged scaffold, as they are believed to mimic the beta-turn motif found in many protein-protein interactions.[6] Spiroketal conformations may be classified as anomeric or non-anomeric. The contra-steric preference for the former of these two conformations derives from preferential interactions between the lone pair of the endocyclic oxygen and ∫* of the exocyclic C-O bond (**Figure 1**). This interaction is classically thought in terms of hyperconjugative arguments although theoretical studies point to the importance of electrostatic interactions in dictating relative stabilities.

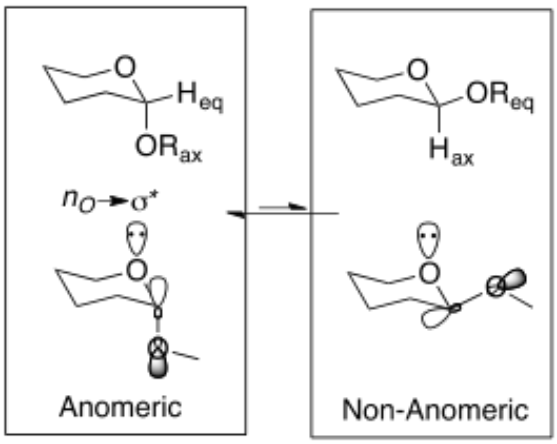

Figure 1. Anomeric and non-anomeric spiroketal conformations showing the frontier molecular orbital basis for the endo-anomeric effect.

The stereoselective synthesis of spiroketals is complicated by the observation that under acidic conditions their formation can be reversible: in other words, while the non-anomeric product may be formed initially the more stable anomeric product will eventually come to dominate as the only product.[7] This observation confirms that the non-anomeric product can be formed under kinetic control, and that the anomeric product is the thermodynamic product. The non-anomeric product is therefore more challenging to access, which has led to intense effort to develop synthetic methods for kinetically-controlled spiroketal formation.[8]

In combinatorial library design, purity is a significant issue and critical to address early on. In the later stages of drug discovery, the capacity to produce a chiral lead molecule with excellent enantioselectivity (>90% ee), yield (>90%) and purity (>80%) can result in a significant amount of cost savings for a medicinal chemistry project.[9] The challenge of accessing a chemically complex library, using synthetic methods that can be scaled up readily has been the ethos of several research groups' strategies in the design of combinatorial libraries and in total synthesis.[10,11] We contrast two strategies for stereoselective synthesis; the early stage introduction of a stereocenter which is used to control subsequent transformations (i.e. substrate controll), and late stage stereoselective transformations. The sensitivity of the non-anomeric spiroketal towards

interconversion to the more stable anomeric form requires that this functionality is introduced at a realtively late stage in a synthetic route.

3.1.2 Conceptual Models for Enantioselective Synthesis

The field of enantioselective synthesis has traditionally focused around several very well developed ("priviledged") catalysts or ligands. Understanding of stereoselective synthesis has been influenced strongly, in particular by application of the Curtin-Hammett principle.[12] The seperation of catalyst behavior (kinetics) and thermodynamics has been one of ease versus that of necessity. Particularly for enantioselective catalysis, there will be a fairly complex relationship between several thermodynamic equilbria which are established (and will shift as reagents are consumed etc) during catalysis. Although computational chemists traditionally think in terms of activation (free energy) barriers , and experimental chemists in terms of rate constants, the elementary rates themselves will change with the concentrations during a reaction. Such complexity makes the de-novo construction of a catalytic reaction especially challening, and often the assumption Curtin-Hammett (CH) type-behavior is a simplification necessary to understand or model the reaction taking place.[13] We outline the CH principle more fully below, but summarize this concept graphically in **Figure 3**.

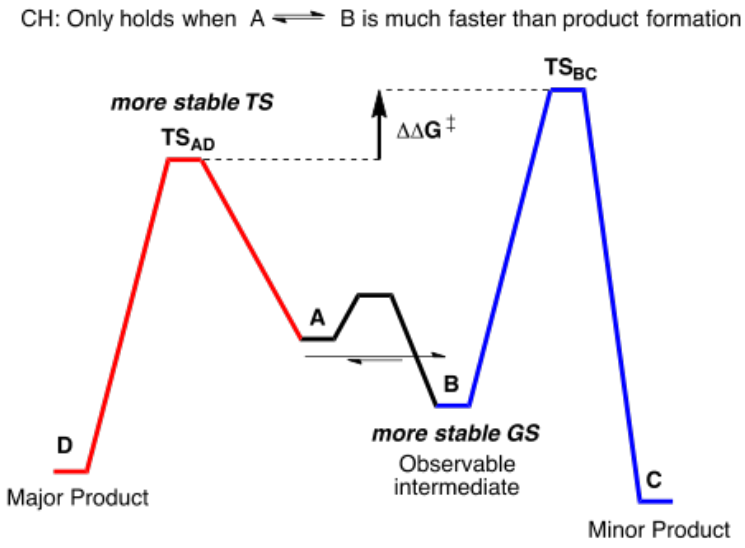

Figure 3. Qualiative free energy profile illustrating Curtin-Hammett behavior, in which the less stable intermediate leads to the major observed product.

The example illustrated by **Figure 3** emphasises that in the CH principle, it is transition state stability which dictates the major product rather than the relative stabilities of the preceding intermediates. The scenario illustrated above also shows that the more stable intermediate (which may be the only one identifiable in experiment) may in fact not lead to the observed product: i.e. the more active pathway is derived from the least stable catalytic species in this case. The belief that by destabilizing the ground state the catalyst is able to accelerate a reaction is not a new hypothesis.[14] If we assume that **Figure 3** describes the formation of different stereoisomers, under conditions of a rapid pre-equilibrium, the stereoisomer formed by the most stable transition state will become the dominant species, assuming that its formation is irreversible. The relationship between the major products being derived from the least stable intermediate in a rapid pre-equilibrium was initial reported by Curtin and Hammett (**Figure 4**).

$$\frac{[C]}{[D]} = \frac{k_{BC}}{k_{AD}} \; K_{AB}$$

$$K_{AB} = e^{(G_B - G_A)/RT} \qquad k_{BC} = e^{(G(TS_{BC}) - G_B)/RT}$$

(transition state theory)

$$\text{leads to: } \frac{[C]}{[D]} = e^{(G(TS_{BC}) - G(TS_{AD}))/RT}$$

Figure 4. Derivation of the Curtin-Hammett equation shown in short-form.

In the context of asymmetric catalysis, one of the most famous expositions of the CH principle is asymmetric hydrogenation of enamides catalyzed by Rh-BINAP complexes to form enantio-enriched amino acid derivatives.[15] The catalytic mechanism is believed to start from the solvated cationic Rhodium catalyst which then coordinates the enamide, (Z)-alpha-acetamidocinnamate (**Figure 4**).

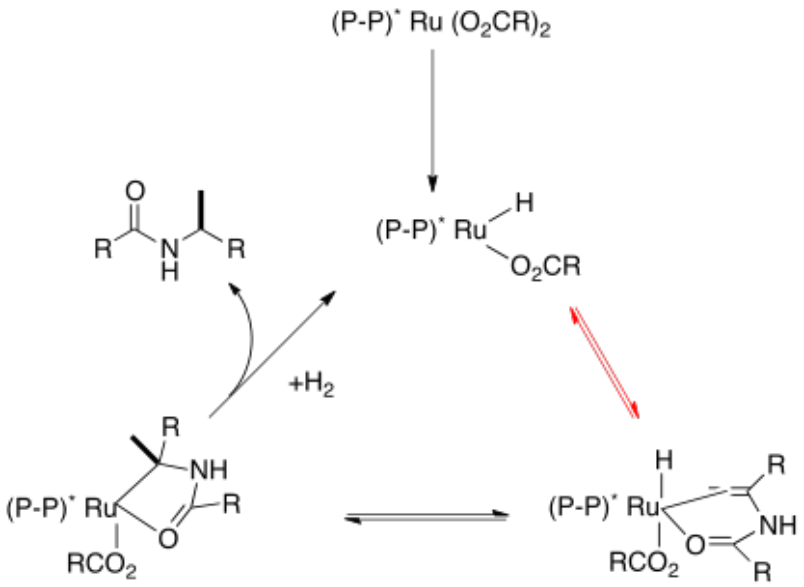

Figure 4. The so-called "Brown-Halpern" mechanism for the enantioselective enamide reduction. The red equilibrium arrows highlight point of rapid equilibrium between competing pro-chiral intermediates.

The diastereomeric catalyst-substrate complexes formed in enamide hydrogenation are able to rapidly interconvert between the pro-R and pro-S complexes. This rapid pre-equilibrium results in the least stable (reactive) diastereomeric leading to dominant product. This well-studied mechanism, partially as a result of the characterizable catalytically active intermediates, has made the Noyori reaction a go-to reaction in industrial production of chiral compounds (**Figure 5**).

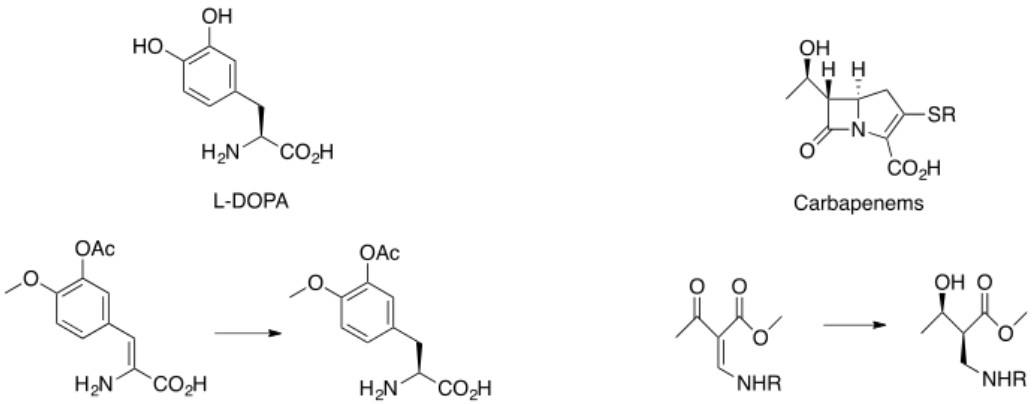

Figure 5. APIs produced through the Noyori reduction method.

The validity of the CH principle depends on the assumptions outlines earlier, and implies a rapid pre-equilibrium (i.e. interconversion of diastereomeric reactant complexes). If this is not the case, it can lead to erosion of the observed enantioselectivity and in some instances flipping of the enantioselectivity, compared to the fully operative CH scenario.[16] This behavior was demonstrated by Daley *et al.* while investigating the reduction of several 3,3-dimethyloxaloacetate derivatives. In the case of the asymmetric hydrogenation shown above, saturation by H_2 limits the interconversion of the reactant complexes and leads to a change in enantioselectivity even though the competing transition states for the hydrometalation step are unchanged. It is fair to say that the CH principle makes the life of the computational chemist significantly easier, since in principle it is only necessary to focus on the competing TS energies. However, the blind assumption that it the C-H principle is in operation may lead to erroneous results.[17]

In this chapter we study different mechanisms of kinetically-controlled spiroketalizations, and look at the role of chiral catalysts (phosphoric acids) in mediating this tranformation stereoselectively. A perplexing issue for phosphoric acid catalysis is the mechanism of action. Unlike the homogenous hydrogenation catalyst mentioned above, the sheer scope of reactions promoted by the chiral phosphoric acid makes it difficult to describe the effects of the catalyst to a single action.[18,19] Thus far though there has been limited experimental kinetic work performed to investigate the mechanism of reactions promoted by phosphoric acids. We decided to start with a simple model and work our way up in complexity, from intramolecular to intermolecular reactions, with varying degrees of symmetry. Rather than just focussing on competing TS structures, we also address the role of the bound subtrate, and investigate whether it is necessary to consider this to understand the selectivity in a qualititative and quantitative fashion.

3.2 Simple Spiroketalizations

3.2.1 Simple Spiroketalizations

As noted previously, a catalyst that displays dynamic behavior could display several ground-state complexes, which can alter the kinetics of the reaction. In **Figure 6,** modulation of the catalyst's 3,3'-substituents from 1,3,5-trisopropylphenyl to anthracenyl groups leads to a complete erosion of enantioselectivity from 92% to essentially racemic product. It is possible that this could be derived from differences in transition state geometries, or equally, the reaction kinetics may be diverted to regimes outside of that envisaged in the Curtin-Hammett scenario. To investigate this correlation and test the non-CH principle model, we decided to investigate the intramolecular enantioselective spiroketalization reaction performed by Nagorny *et. al*.[20]

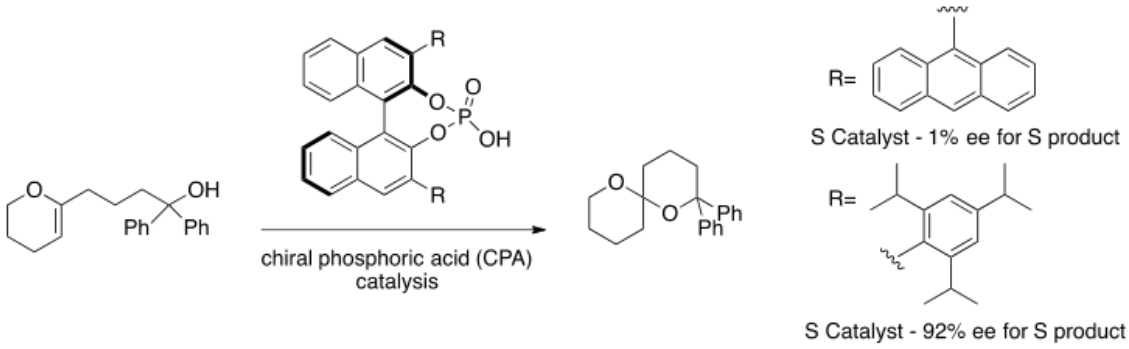

Figure 6. Varying enantioselectivity in asymmetric spiroketalization through catalyst modulation.

Before we were able to investigate the enantioselective reaction we needed to establish the mechanism of kinetically-controlled spiroketalizations from enol-ether substrates. In doing so, we sought to determine the rate-determining step **(RDS)** and validate our methodology on a simple chemical model. Based on known experimental data, the non-anomeric selectivity of the phosphate catalyst could be described by two different mechanisms; specific acid catalysis and general acid/base catalysis (**Figure 7**).

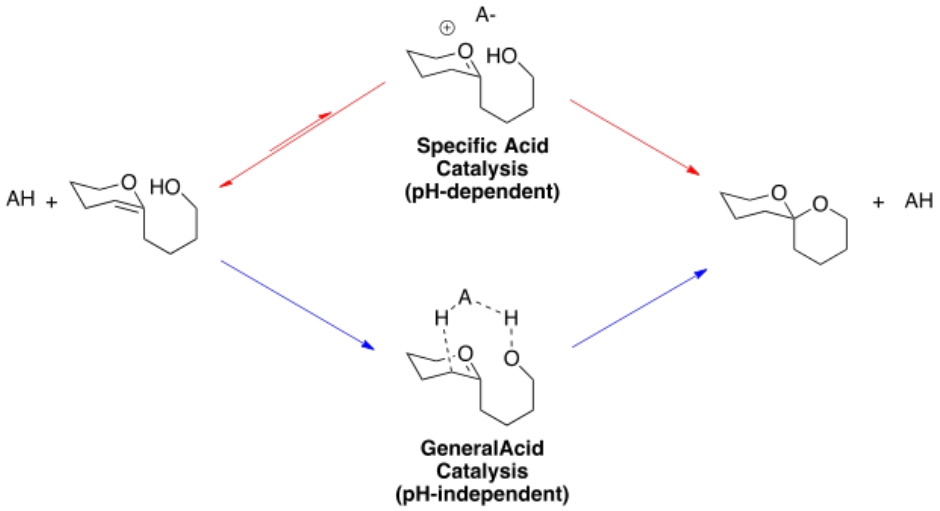

Figure 7. Putative mechanisms investigated for Brønsted-acid promoted spiroketalization.

The specific acid mechanism (**Figure 7**, red) was advanced by Pierre Deslongchamps based on the increased non-anomeric selectivity observed when the acid used to promote the reaction was altered.[21,22] Deslongchamps argued that the selectivity was dependent on the conformation of a discrete oxonium intermediate formed following the protonation. As the conformation drifts from a half-chair to a skew boat in the non-anomeric species we would expect diaxial strain to increase. The anomeric trajectory, on the other hand, proceeds from a half-chair conformation to a chair conformation in the product resulting in a trajectory that will show lower diaxial strain (**Figure 8**). In fact, the endo-anomeric effect is stronger in the TS leading to the non-anomeric conformation in the skew boat conformation. The difficulty with this argument is knowing how to evaluate the combined quantitative influence of all of the steric and stereoelectronic interactions, and whether one is dominant.

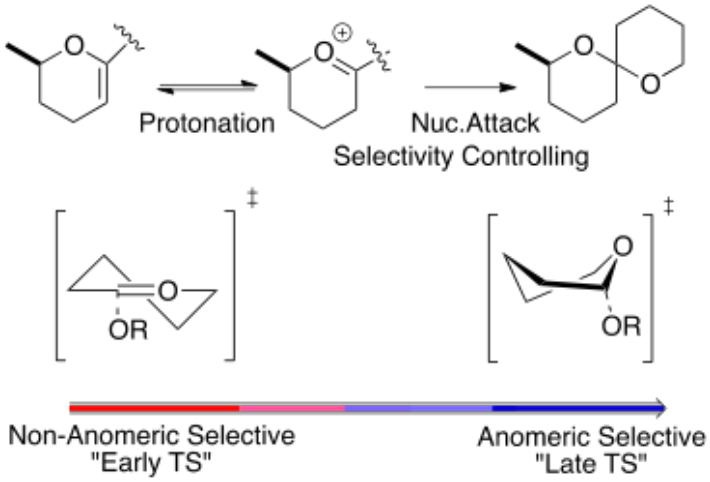

Figure 8. The impact of the conformation of the transition state on the selectivity for the outcome of the reaction.

The existence of charged intermediates is also possible in the chiral phosphoric acid (CPA) catalyzed spiroketalization of enol-ethers, which occurs stereoselectively. Here proton transfer to the enol-ether from the catalyst forms a chiral phosphate counterion, which can influence the stereochemical outcome of C-O bond forming step by forming a tight ion-pair with the oxonium intermediate. This would embody the aptly named process of Asymmetric Counterion Directed Catalysis (ACDC) (**Figure 9**).[23]

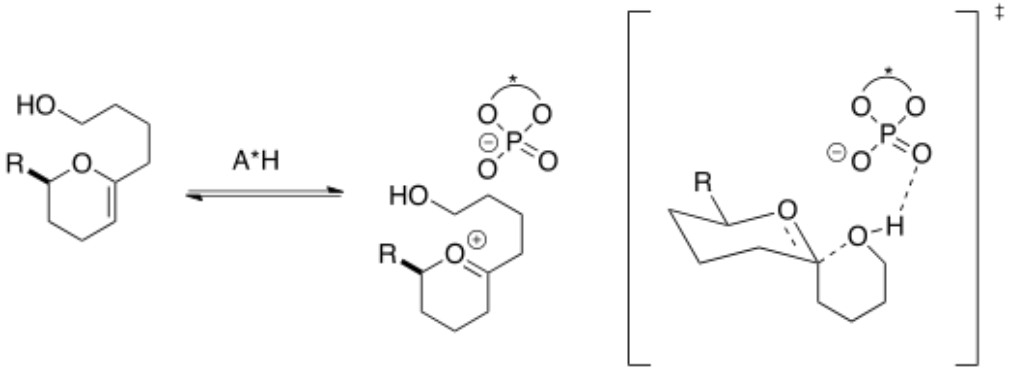

Figure 9: CPA promoted enantioselective spiroketalization proceeding through a specific-acid mechanism, with stereoinduction by ACDC.

On the other hand, a simultaneous general base/acid mechanism has also been proposed based on the experimental evidence of Tan, who showed that the spiroketalization of an epoxidated glycal performed in methanol solvent proceeded with non-anomeric cyclization as the dominant product.[24] To investigate this mechanism they consructed a linear free energy relationship (LFER) and peformed kinetic studies to determine the role of the solvent and the position of the transition state based on the sensitivity to the aromatic susbtituent (**Figure 10**).

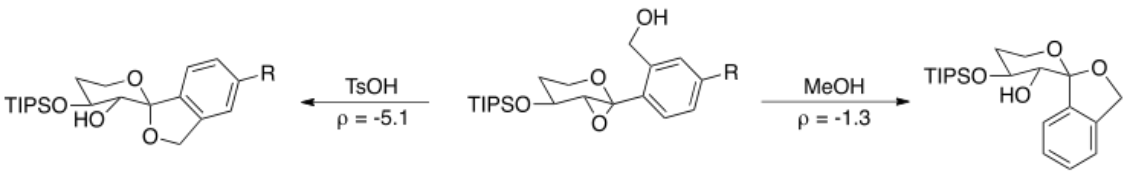

Figure 10: Investigations performed by Tan and co-workers; reactions in TsOH and MeOH display different Hammett constants indicative of differences in mechanism.

Tan and co-workers obtained a low Hammett ⟩-value for the methanol promoted spiroketalization relative to the acid promoted spiroketalization. They proposed that the mechanism for the methanol-promoted spiroketalization was a S_N2 reaction: the methanol solvent deactivates the anomeric effect by interacting with the *endocyclic* oxygen. This would limit the ability to form a stable carbocation/oxocarbenium intermediate, which is presumably the case for the reaction occuring with TsOH. Based on our previous computational investigations with the 6-*endo-tet* reaction we believed could use a "solvent bridge model" to investigate the proposed S_N2 mechanism. Our computational results in this chapter are presented firstly for the reactions described by Deslongchamps and Tan, in which the spirocyclizations are promoted by small, chairl molecules. We use this work to gain insight into the mechanistic and conformational details of the transformation, and then proceed to study the role of CPA catalysts in enantioselective spirocyclizations. This process was developed to ensure that the computational methodology was performing adequately, so that conclusions derived from the transition structures and reaction coordinate were not erroneous.

3.2.2 Brønsted Acid Promoted Spiroketalizations

In the 1970's and early 1980's Deslongchamps investigated the role of anomeric effects upon stereoselectivity. In his seminal work on spiroketalization he found that the pKa value of a Brønsted acid had a significant effect upon the anomeric selectivity in spiroketalizations of enol-ethers (**Figure 8)**. The fact that different product ratios are obtained with different acids confirms that the reaction is not thermodynamically controlled. To account for these experimental results, Deslongchamps proposed that the stereo-controlling event occured after oxonium formation: the discrimination depended on the position of the transition state for nucleophilic attack.

The significance of the TS position of nucleophilic attack derives from the role of the "intrinsic" anomeric effect in controlling reactions. For the non-anomeric trajectory the ring must adopt a skew-boat conformation to allow for the anomeric effect to operate.[22,25] For the anomeric trajectory there is no need for such ring-distortion. However, it is also necessary to consider intermolecular and intermolecular interactions; intermolecular interactions between the glycal and the conjugate base, and intramolecular (steric and stereoelectronic) interactions when considering ring conformation. The effect of the transition state position becomes quite evident when the transition state is early, both trajectories display similar conformations thus the selectivity is dependent on the steric interactions with counter-ion. When the transition state is later, the ring-distortion for the non-anomeric approach promotes greater selectivity for the anomeric product, which has a lower-energy conformation. In this mechanism there are several intermolecular effects that would difficult to separate from the product distribution with different acids (**Figure 11**): the stability of the ion-complex would have an impact on the selectivity as changes in the stability of this intermediate could shift the position of transition state; the general base activity of the counterion though would be more convoluted since it could accelerate the reaction without altering the TS position. To investigate Deslongchamps' model and determine the inherent controlling effects we modeled the Brønsted acid spiroketalization of the enol-ether in **Figure 12** using HCl, formic acid and phosphoric acid. DFT calculations were performed at the M06-2X/6-31G(d,p) level of theory to investigate the mechanism of this transformation.

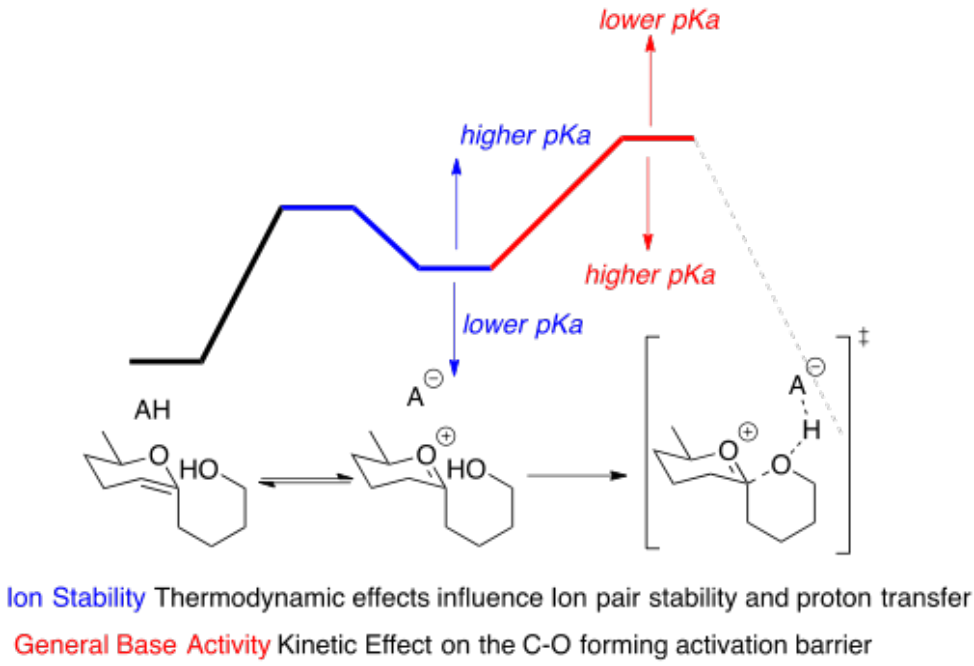

Figure 11. The potential role of the conjugate base (i.e. the counteranion) upon the the kinetics of spirocyclization.

The three acids (HCl, HCO_2H, H_3PO_4) are common reagents in promoting spiroketalization which display different Brønsted acidities and steric requirements. Approximate pKa_1 values are -7, 3.8 and 2.1. From our computational study we can probe their effects on the selectivity of the reaction and probe the possible existence of the oxonium as an intermediate. In fact, during the course of our calculations we were unable to locate a stable intermediate corresponding to an oxonium/conjugate base ion pair. In our optimizations, the proton transfer from acid to the enol-ether was always followed by evolution to the cyclized product without an intervening intermediate. Therefore, computationally the favored mechanism with each acid was a concerted, but highly asynchronous process in which a proton is shuttled between subtrate and conjugate base, leading to intramolecular nucleophilic attack. This new information led us to suppose that the rate-determining step is the proton transfer to the enol as the barrier to the nucleophilic attack was too small to determine. Treating the proton transfer as the rate-determining step allowed us to predict the spiroketalization selectivity (**Table 1**). The experimental substrate has a pre-existing stereocenter so that the two diastereomers can be distinguished experimentally. In our computations, since we can follow the evolution of two TS structures to the anomeric or non-anomeric

product this substituent is not necessary for us to compute the kinetic selectivity. Of course, this substrate could not be tested experimentally since the conformational interconversion of products would be rapid, however, we are able to compare the relative TS energies against the experimental product ratios.

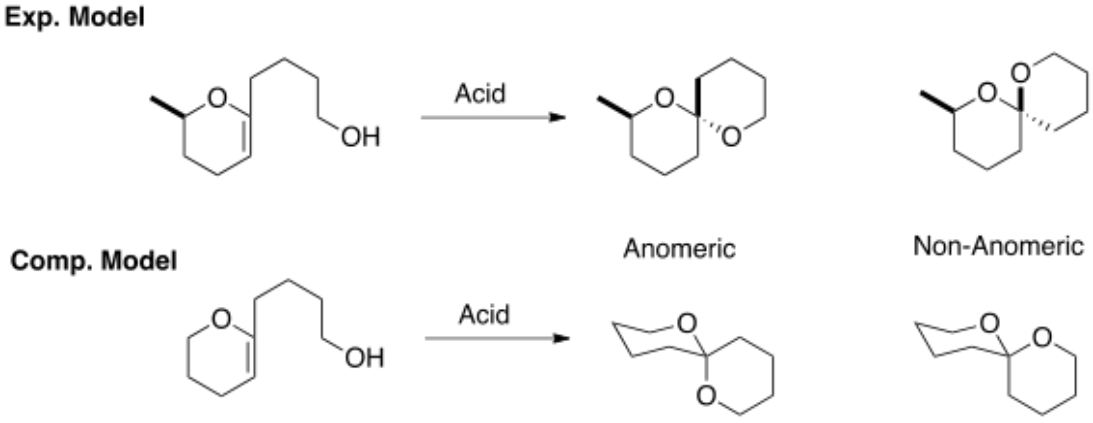

Figure 12. Spirocyclization reaction studied computationally.

Acid	Experimental Selectivity	⊗⊗$E^{‡}$ (kcal/mol)	Computed Selectivity
HCl	55% Anomeric	0.1	54 % Anomeric
H_3PO_4	60% Anomeric	0.2	60% Anomeric
HCO_2H	57% Non-Anomeric	-0.2	58% Non-Anomeric

Table 1. Comparison of kinetic selectivities computed *versus* experimentally obtained product ratios.

Our calculations suggest that a single step controls the reactivity, for which two distince conformations of the TS are possible. From this new mechanism the origin of the selectivity could result from the geometric differences between the acids and their

respective interactions with the pro-anomeric or pro-non-anomeric faces of the substrate. Key differences between the acids considered are the required spatial interactions that would promote a general base activity to re-generate the acid. The acid with the least spatial constraints is HCl. From a structural analysis of optimized TS structures we find that the critical difference between these structures is the non-anomeric acyclic ring has adopted a distorted chair conformation (80°) while the anomeric TS displays a more ideal dihedral angle of 71° (**Figure 13**). The fact that the selectivity is modest means that the relative stabilities of the two structures are very similar. This is consistent with the idea that the stereoselectivity is controlled by protonation which is relatively unselective, and then the nucleophilic closure proceeds without an additional barrier.

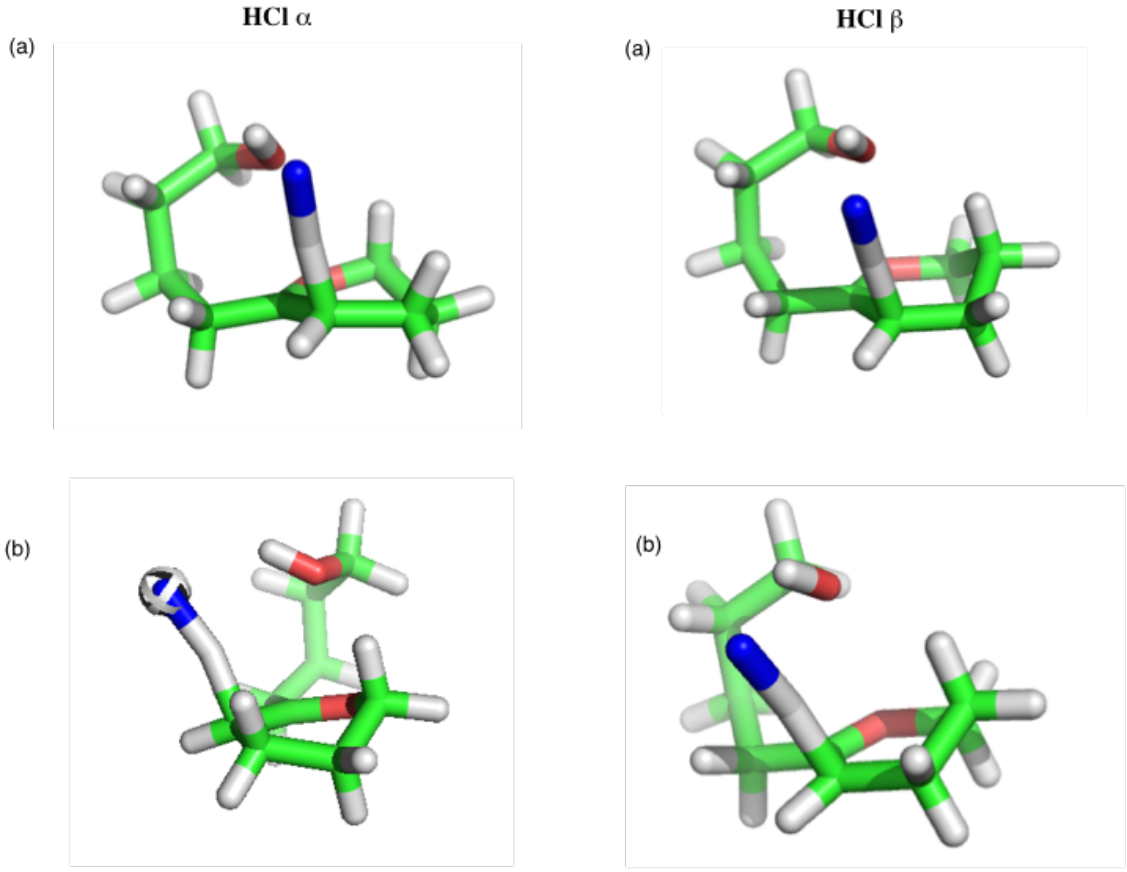

Figure 13. M062x/6-31G(d,p) TS structures for anomeric (⟨) and non-anomeric (®) spiroketalization promoted by HCl; (a) highlights the geometry of the rate-determining proton transfer while (b) highlights the ring conformation.

In the GS leading to the anomeric product we find that the HCl proton is 1.91 Å away from enol carbon, with an approach trajectory of 94.3°. The non-anomeric counterpart displays an approach trajectory of 91.8° with a very similar distance to the proton. In the non-anomeric ground state the HCl can position itself to display a productive NAC: the alcohol can distort since there are no unfavorable steric interactions with the axial H-6 proton. The anomeric conformation on the other hand has to adopt a more unfavorable NAC as the alcohol is unable to adopt a new dihedral angle because of steric interactions with the axial hydrogen at H-6.

Considering the phosphoric acid, phosphate is known (i.e. in nature) to accept hydrogen bonding interactions with its oxygens and to act as a general base through this interaction. In the GS we find that alcohol coordinates to the phosphoric acid through a hydrogen bond in both non-anomeric and anomeric reaction pathways. The dihedral angle is similar between these conformations (76.1° and 75.3°, respectively) and the H-bonding distances are similar (1.98Å for both) (**Figure 14**). In the TSs we find the same trend of angles and distances. Considering the position of the transferring proton in each TS, for the anomeric TS, the proton lies 1.36 Å away from the oxygen and 1.28 Å from the carbon. The non-anomeric TS has an earlier transition state with the proton transfer 1.32 Å from the oxygen and 1.30 Å away from the reacting carbon.

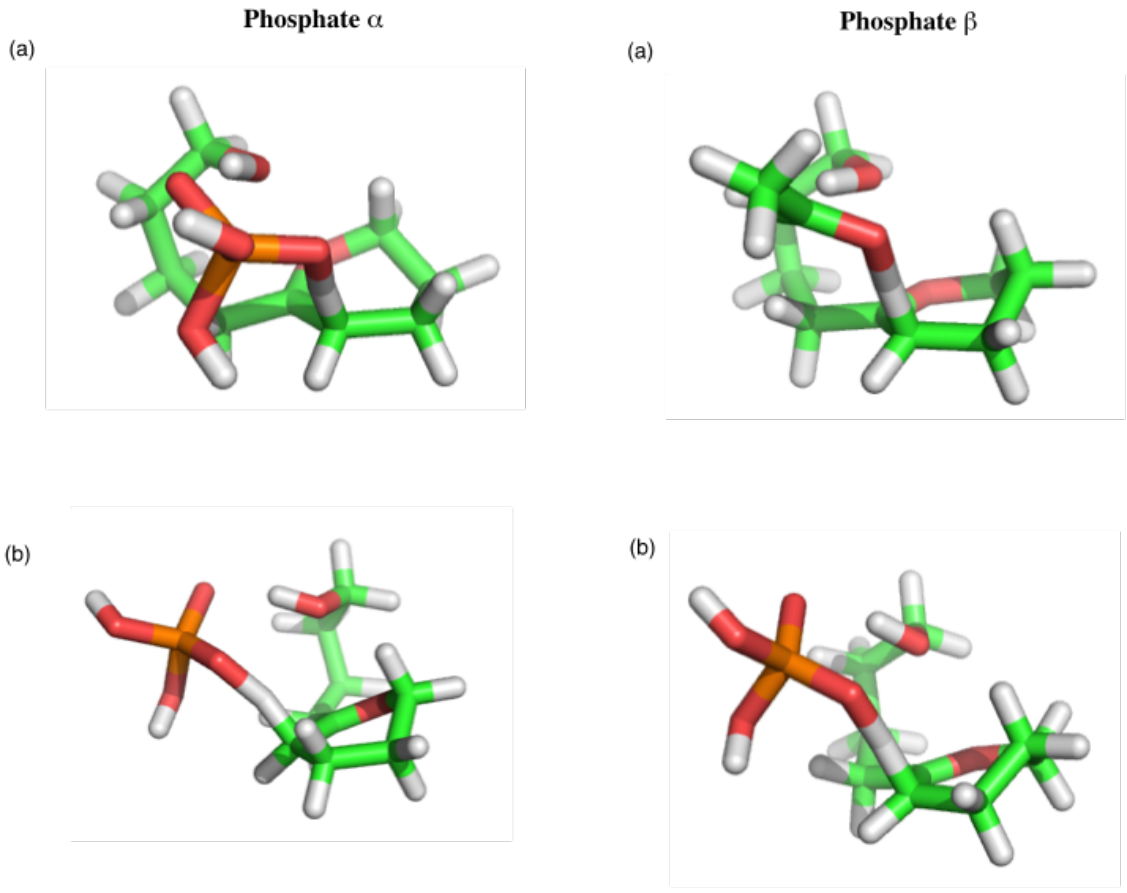

Figure 14. M062x/6-31G(d,p) TS structures for anomeric (⟨) and non-anomeric (®) spiroketalization promoted by H_3PO_4; (a) highlights the geometry of the rate-determining proton transfer while (b) highlights the ring conformation.

Based on the results for the Deslongchamps' model for cyclization the rate determining and selectivity determining step is the protonation of the enol. This TS evolves to the cyclized produce without the intervention of a second TS for C-O formation. The selectivity for the reaction is dependent on the conformation of this transition state. The relatively small differences between anomeric and non-anomeric product ratios is consistent with protonation of either alkene face without pronounced selectivity, and collapse to the product. The ability of the conjugate base to interact with the alcohol, effectively shuttling a proton between this alcohol and the enol-ether is assisted by coordination with e.g. phosphoric acid.

3.2.3 Alcohol Promoted Spiroketalizations

Tan's work has focused on the synthesis of benzannulated spiroketal natural products.[28] During the development of their methodology they found that the non-anomeric spiroketalization reaction could be promoted in methanol alone. Upon investigation of this reaction they found that the kinetics showed a second order dependence on the solvent, methanol, and displayed a Hammett ⟩–value of -1.3. The low ⟩ value as compared to the tosic acid promoted case, -5.1, convinced the authors that the reaction had become S_N2 *versus* S_N1 proceeding via an oxonium intermediate (**Figure 10**).

To explain the aberration of the anomeric effect the authors proposed that methanol is hydrogen bonding to the endocyclic oxygen. We examined this model computationally and compared experimental Hammett values against our predicted values obtained from transition state theory. GS and TS structures were optimized at the M062x/6-31G(d,p) level of theory, including explicit solvent molecules and an implicit solvent correction to describe bulk electrostatic and polarization effects. Single point energy calculations were then performed on the optimized structures at the B2-PLYP/def2-TZVPP level of theory. We constructed an initial model based on proposed interaction of a methanol molecule with the ring oxygen atom. However, in our optimizations the methanol relocated to coordinate with the nucleophilic alcohol, acting as general base, and the interaction with the ring oxygen was not maintained. This reaction model displayed S_N2-type behavior for all derivatives of the aryl group.

Para Substituent	**Activation Barrier (kcal/mol)**	**Calculated TST $\log(k_X/k_H)$**	**Experimental $\log(k_X/k_H)$**
H	18.98	0	0
OMe	18.99	-0.01	0.24
Me	17.98	0.92	0.057
CF_3	19.41	-0.40	-0.86

Table 2. Activation parameters computed with MeOH interacting with the endocyclic oxygen, and correlation with experimental values.

The reaction profile for this model displays the S_N2 (i.e. concerted) energy profile that we could expect for inversion of the stereocenter. In the TS with a p-OMe group we find that the endocyclic O_{endo}-C bond distance has decreased from 1.39 to 1.30 Å, which could support the formation of the oxonium intermediate. The possible existence of the oxonium intermediate can be decided based on the structure of the TS, focussing on the dissociative reaction center, nucleophilic trajectory and ring conformation. The reaction center can give a initial clue to the oxonium formation as the intramolecular promoted opening would be significantly faster than nucleophilic attack. This would result in a dissociative transition state. From the TS structure for the p-OMe derivative we find that the bond breaking is 2.17 Å in the TS and 1.39 Å in the GS, while there is only very minimal bond formation; the nucleophile is 2.03 Å away (**Figure 15**). The exploded transition state as well as the shorted endocyclic oxygen bond could support an oxonium intermediate. Of course this is not conclusive as we would expect that an electronic deficient center could still shorten its sp^3 bonds because of the change in the electronegativity.

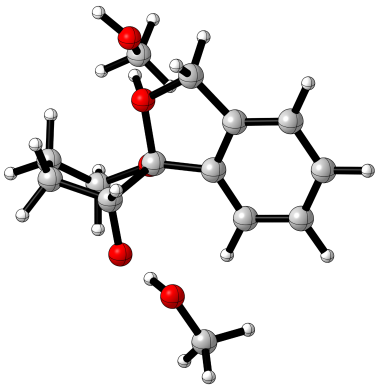

Figure 15. CPCM-M06-2x/6-31G(d,p) TS structure resulting from investigation of the originally proposed model.

The nucleophilic trajectory relays information about the LUMO. We examined a control substrate without an endocyclic oxygen atom to examine the TS geomtry of epoxide opening (**Figure 16**). We find that in this TS structure the approach trajectory for epoxide opening is 98.7° and that for the oxonium approach is 104.8°.

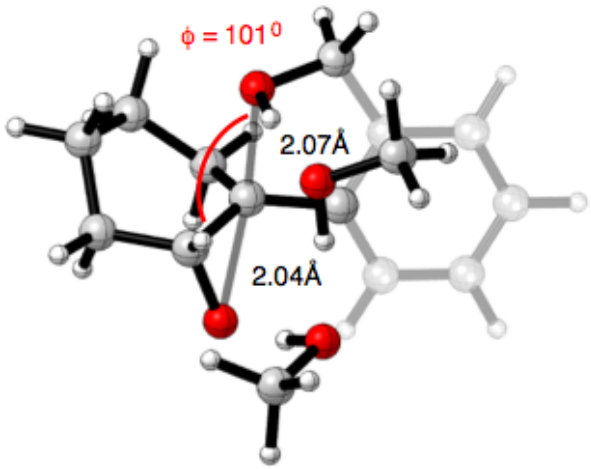

Figure 16. TS with approach trajectory and distances for the intramolecular epoxide opening without an adjacent oxygen atom.

The conformation of the pyran in this model is indicative of an early twist boat, which would promote orbital overlap between O_{endo} and C_{ano}. If the reaction was going through an S_N2-type mechanism then we would not expect any assistance from the endocyclic oxygen in stabilization of the nucleophilic trajectory. To explore how the electronic tuning of the reaction center affects the transition state we investigated the CF_3 substituted derivative. From our calculations the nucleophile is deactivated and the epoxide bond retracts slightly (**Table 2**). The approach trajectory for the epoxide has increased to 100.3° while the trajectory approach for the oxonium has decreased to 103.5°. This would give some indication that the nucleophile is interacting with epoxide LUMO. The conformation and decrease in the endocyclic bond to 1.29 Å would indicate that the endocyclic oxygen has become more engaged in the reaction center.

This result is what we would expect for a general acid/base reaction where the acceleration of nucleophilic attack is such that the reaction proceeds via a single TS, an S_N2 reaction course along the potential surface. This effect is observed in enzymology

and has been more thoroughly characterized through transition state inhibitors and computational modeling. [29] This model has structural similarity to inverting glycosyl-transferases.

Following the intrinsic reaction coordinate (IRC) we find that the product in our computational model is unable to transfer the protons from the nucleophile to the leaving group along the reaction coordinate. Using the CF_3 derivative as an example we find that the nucleophile is 1.56 Å away with the pryan template displaying a full twist boat conformation. It is evident from the structure that the "product" was unable to transfer the protons (**Figure 17**). This higlights a potential limitation of an isolated model for the reaction, in which the bulk solvent is unable to participate in e.g. proton shuttling since it is only described implicitly. The limitation of the model aside, the originally proposed model speculated that hydrogen bonding to the endocyclic oxygen was inhibiting the anomeric effect, however computations suggest that this is not relevant to the substrate reactivity observed.

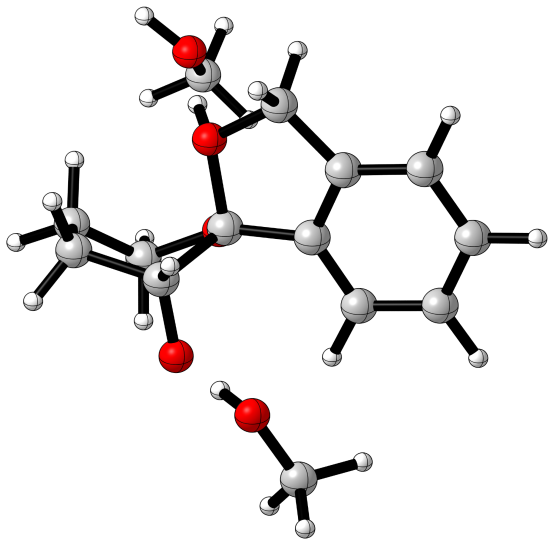

Figure 17. "Product" found at the end of the IRC as a result of unstable charge development.

From our knowledge of glycosylations we surmised that the anomeric effect could be attenuated if the ring was distorted to an unfavorable conformation resulting in poor overlap between the endocyclic oxygen and epoxide. This distortion would curtail the formation of the oxonium intermediate by inducing strain in the ring as a result of the endocyclic oxygen trying to maximize overlap with the epoxide LUMO. To induce this effect we could expect that there would have to be a favorable effect to counteract any strain from a ring distortion. This could occur if the methanol molecules were able to communicate through a hydrogen-bonding network. This network would also allow the effective charge transfer between with in the reaction center that was lacking previously, (**Figure 18**). Another possibility is the bulk solvent is organizing around the transition state in such a way that the anomeric face is blocked through H-Bonding interactions with the solvent.

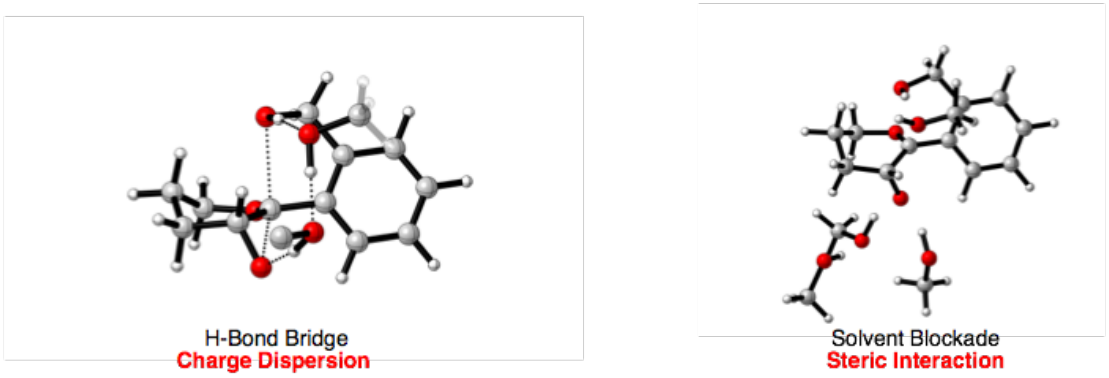

Figure 18. Possible methods by which solvent can inhibit the anomeric effect.

To test these ideas we emulated the approach from our previous calculations. By studying the three substrated with a bridged-methanol type model, we obtained a calculated ⟩ of = -1 with an R^2= 0.93, close to experiment (**Table 3**). The reaction profile for this reaction displayed the traditional oxonium formation only for the methoxy derivative; however, the attack of this had a barrier of 0.05 kcal/mol, which effectively makes all three substrates react in a concerted mechanism since the lifetime would be shorter than a vibration. With an electron-deficient substituent we found that the second transition state, nucleophic attack, was lower in energy then the intermediate: this can occur due to innaccuracies in solvation treatment etc. and effectively means that the second step is barrierless.

Para Substituent	Activation Barrier (kcal/mol)	Calculated TST $\log(k_X/k_H)$	Experimental $\log(k_X/k_H)$		
H	16.80	0	0		
OMe	16.38	0.38	0.33	0.24	0.14
Me	16.88	-0.079	0.085	0.042	0.044
Cl	17.30	-0.46	-0.30	-0.35	-0.56
CF_3	17.44	-0.59	-0.63	-1.1	-0.85

Table 3. Activation parameters computed for the solvent bridge model and the ⟩ values compared against the experimental measurements (in triplicate).

Within this solvent-bridged model, the TS for the methoxy derivative shows a trajectory approach of 95.7° and 97.4° for the epoxide and oxonium intermediate respectively (**Figure 19**). These trajectories would indicate that the TS is earlier relative to the non-hydrogen bond network model. The TS in this case is significantly more exploded relative to the non-bridging model with the epoxide bond breaking at 2.17 Å

and the nucleophile 2.52 Å away. The conformation of the pryan ring did not alter drastically from that of the Tan's original model.

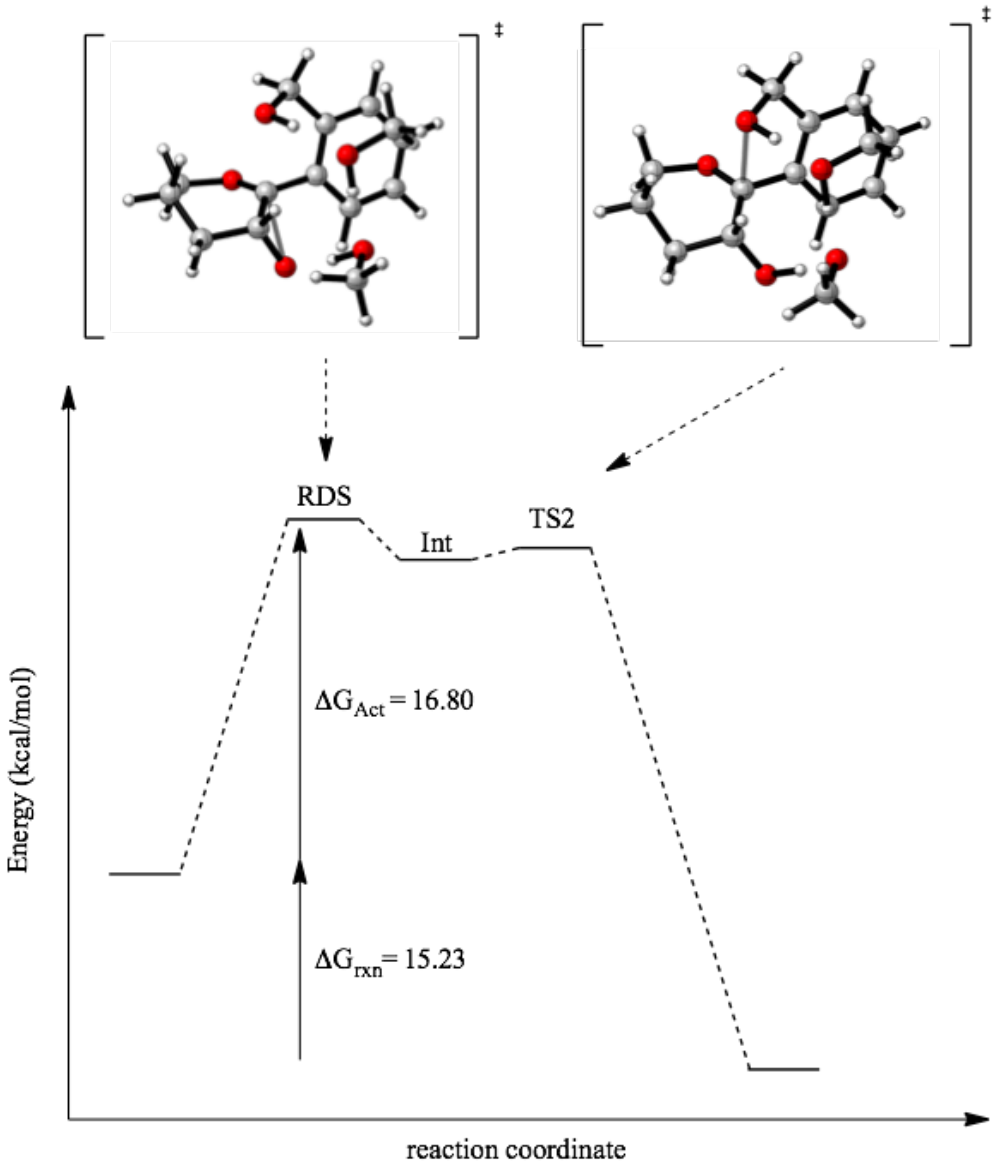

Figure 19. CPCM-M06-2x/6-31G(d,p) computed representative reaction coordinated for bridging MeOH molecules in an S_N2 spiroketalization.

As we would expect from a reaction with a low charge development at the reaction center the transition state changes very little with differing substituents, from methoxy to the trifluoromethyl derivative. The CF_3 TS shows an approach trajectory of 95.3° and 98.1° which is similar to OMe, but significantly different from its contemporary in the non bridging case. From these results it is evident that with greater electronic

release there is a strong possibility that the reaction can display S_N2 characteristics. These characteristics have not arisen by abolishing the anomeric effect but through acceleration of the nucleophilic step by providing simultaneous activation of the electrophile and nucleophile by shuttling the proton from one to the other, avoiding unfavorable charge separation.

Our small "cluster" model captures the essential electronics of the reaction, and the importance of proton transfer between nucleophile and electrophile. However, with QM calculations it is difficult to capture the realistic effects of the bulk solvent beyond an implicit treatment. This prompted us to consider using a QM/MM MD methodology and to compare the results with the known LFER data. Therefore, we performed QM/MM MD umbrella-sampling simulations. The semi-empirical DFTB method was used for the QM description of the TS in the simulation and MM (AMBER force field) was used to describe a box of methanol solvent molecules.[30] These simulations led to an estimated activation barrier of less than 5 kcal/mol, which is in obvious disagreement with DFT results.

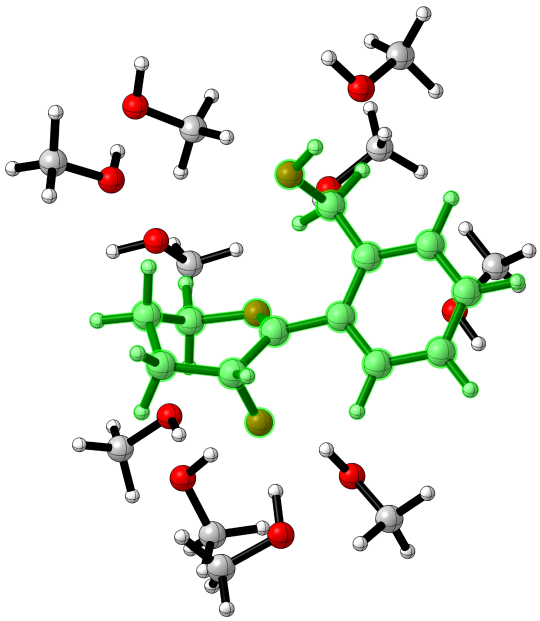

Figure 20. Model highlighting the solvent surrounding the transition state and the portion of the model being treated with high-level computation.

As an alternative to using the DFTB/MM energetics, we utilized the structural information generated during the course of the MD simulations to perform energy calculations with Gaussian (**Figure 20**). Effectively, this approach generates models with several solvent molecules whose positions have been sampled properly. Snapshots from the MD simulations were generated at regular intervals every 50 ps, and the model was truncated by only keeping the solvent molecules with 5 Å of the reaction center the MD simulations contain several thousand atoms, from the methanol solvent molecules. This resulted in snapshots of systems with around 100+ atoms which were recomputed at the PM6 semi-empirical level of theory. To recalculate the reaction profile the structure was reoptimized to find a TS but the solvent positions were fixed. This approximation assumes the transition state lifetime (on the order of a femtosecond) is shorter then that of the rate of non-viscous diffusion. From this approach we were able to optimize a transition state structure and re-develop the Hammett plot. From this initial proof of concept we were able to generate an explicit solvent model that displayed a $\rangle$ =-1.43 (exp. -1.3) with an R^2=0.75. The solvent molecules perform the same role as in the cluster model with two MeOH molecules: namely to activate the OH group and the epoxide. In this larger model there is no formal proton transfer mediated through the solvent molecules, however, this could be

an artefact from the classical simulation used to generate the conformations. In this model, the TS is more oxonium-like, however, the attack still occurs with inversion since several molecules interact with the epoxide blocking the anomeric face of the glycal (**Figure 21**).

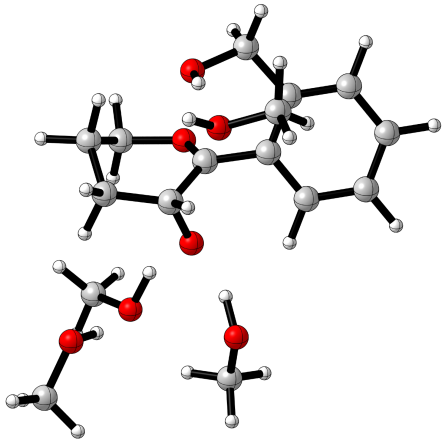

Figure 21. TS in bulk solvent showing the anomeric face being blocked by the solvent through hydrogen bonding.

We next investigated whether single point energy calculations could improve the accuracy of these calculations, since the PM6 semi-empirical method is likely to introduce innaccuracies. For these single point calculations we used the M062x/TZVP level of theory. The results that we obtained from these DFT calculations showed no improvement.

Our results thus far highlight that the rate-determining step for spiroketalization from utilizing an enol substrate is the proton-transfer from the acid. Addition across the C=C bond mechanism is in a *syn*-fashion, either proceeding via a very short-lived oxonium intermediate, or more often, by the asynchronous addition of a tethered nucleophile. This avoids unfavorable charge separation in the transition state, leading to a stereo-control event linked to the stability of both the ground-state complex and the transition state. In the reactivity of the epoxides of enol-ethers, the role of hydrogen bonding additives, such as methanol solvent, is to mediate the proton transfer from the nucleophilic alcohol to the electrophilic epoxide, again avoiding unfavorable charge separation in the TS. These studies suggested to us that CPA-catalayzed spirocyclization of enol-ethers would follow similar rules, namely, that the catalyst

would enable syn-addition across the C=C bond, effectively shuttling a proton from the alcohol to the enol-ether. We therefore turned to the enantioselective CPA-catalyzed transformation.

3.3 C.P.A Promoted Sprioketalization

3.3.1 Computational studies with TRIP

In order to treat the size of the systems we decided to use QM/MM for our calculations which have been shown in the past to be successful in other phosphoric acid catalyst models.[31] In this reaction, stereoelectronic effects play an important role, and improper selection of the DFT method could lead to an erroneous model. To determine which functional was the most appropriate we calculated the transition states for the proton transfers between the anomeric and non-anomeric face. With the 6-31G(d,p) basis set, we found that the M06L functional correclty predicted the correct major product (1.80 kcal/mol in favor of the non-anomeric product), while both B97D3 and B3LYP were unable to predict the correct major product (1.38 and 1.46 kcal/mol in favor of the anomeric product).

The lower level of theory was chosen as molecular mechanics, with the Universal Force Field (UFF). This has been shown in the past to the describe CPA-catalyzed reactions with good reproduction of experimental results, and described the torsional potential of the BINOL backbone well. Nevertheless, we did notice some differences with respect to the M06L catalyst structure, which is critical for the description of the chiral pocket size and interactions.[31] The ONIOM (QM/MM) method has difficulty with interactions at the boundaries of the two levels of theory, such as charged interactions between the high- and low-level. To help mitigate these errors we would peformed DFT single point energy calculations on the ONIOM optimized structures. Using the transition states derived from B97D3, B3LYP, and M06l we performed single point calculations with CPCM solvent corrections for heptane. Since M062x was not used previously we decided to use the M06L transition state structures. From **Table 8** it is evident that the M062x single point calculation were the most accurate since they predicted the selectivity of the experimental reaction.

Functional	Basis Set	Selectivity
B97D3	TZVP	1.9 kcal/mol (Anomeric)
M06L	TZVP	0.14 kcal/mol (Non-Anomeric)
M062x	TZVP	1.12 kcal/mol (Non-Anomeric)
EXP		**-0.94 kcal/mol (Non-Anomeric)**

Table 8. Accuracy of the single point energy calculations with different functionals.

The model that we found to be the most predictive was the *syn*-addition model. An alternative *anti*-addition was rejected since it predicted the anomeric product as heavily favored, and perhaps more compellingly, the absolute energy of the *syn*-addition models' transition state was 6 kcal/mol lower then that of the most stable anti-addition transition state. For the addition of phosphate to the substrate we were unable to find a transition state.

We performed NMR experiments which suggested that a deuterated phosphoric acid could deuterate an enol ether substrate, however, computationally it was not possible to locate a discrete oxinium intermediate for the non-anomeric reaction pathway. Could our inability to find the transition state be because the barrier to was to small or along this potential energy surface was there no second transition state? To aid in addressing this question we performed a scan along the nucleophile-anomeric carbon trajectory from the transition state position to the product position. This showed the barrier to the second TS as only 1 kcal/mol, indicating that it would be very short lived. This information tells us that even though the oxonium intermediate is being formed, the general base activity is accelerating the addition of the nucleophile.

We also considered the possibility of two distinct coordination modes of the catalyst: monodentate and bidentate. These distinguish whether the catalyst interacts via a single oxygen atom, or by two (i.e. bifunctional) oxygen atoms along the reaction pathway. In most previous applications, the bidentate mode is assumed to be operative, however, such activity has been proposed and supported in some retaining glycosyl transferases[34] (**Figure 22**). Two aspects that separate these two coordination modes are the recognition of the ground state and their steric requirements. The bidentate ground state binds via two hydrogen bonds and requires the substrate to fully accommodate into the BINOL ligand pocket. This requirement is diminished in the monodentate binding since there is only one hydrogen bonding interaction. Additionally, these two different binding modes are not discrete pathways. It would appear that the monodentate could arise following the breaking of the more stable bidentate ground state. With the establishment of the mechanism and the methodology we felt confident in exploring the mechanism of the phosphoric acid catalyzed spiroketalization.

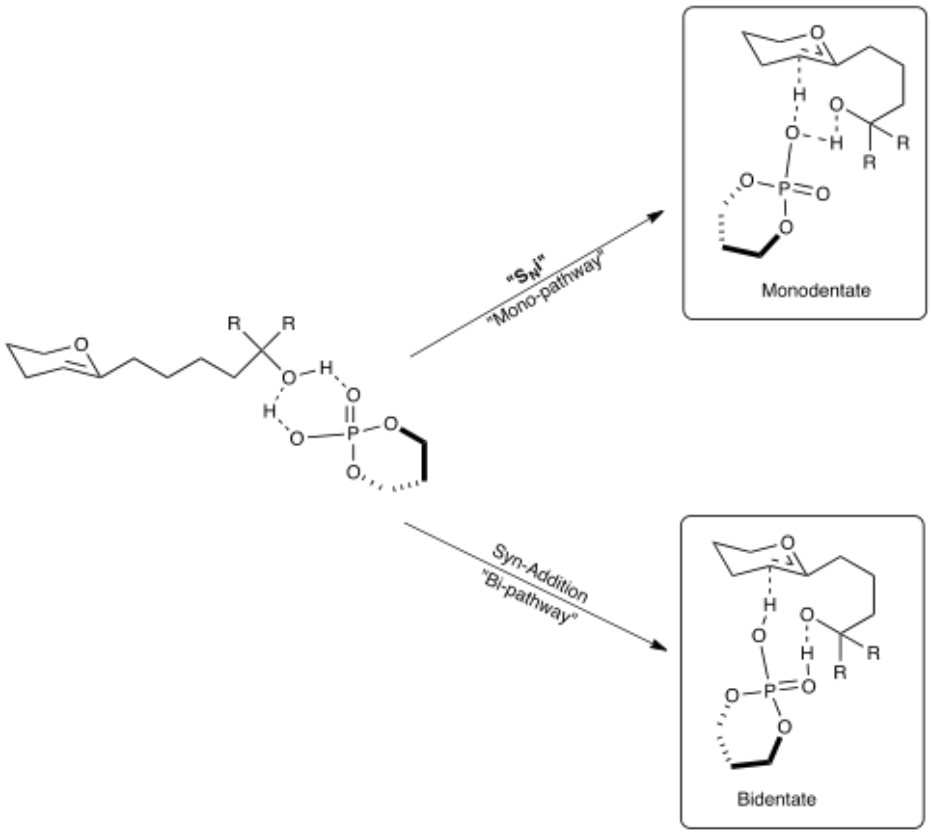

Figure 22. The difference between the bidentate and monodentate binding to promote the spirocyclization, considered computationally.

3.3.2 D-Glycal Spiroketalization by (S) TRIP

Nagorny *et. al.* showed that using S-TRIP phosphoric acid catalyst instead of an achiral catalyst, it was possible to obtain the non-anomeric adduct (**Figure 23**).[35]

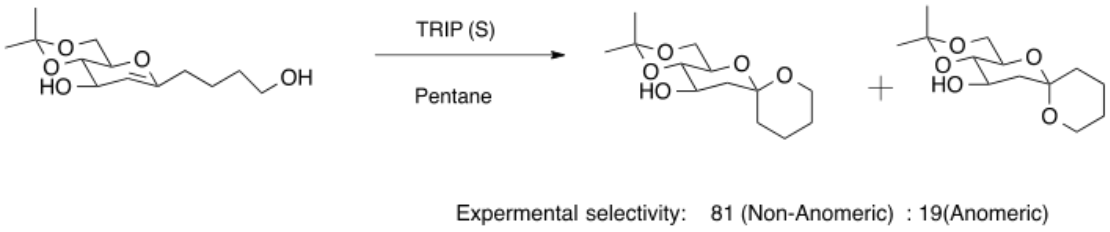

Figure 23. Experimental outcome for the TRIP promoted spiroketalization of a glycal

This significant experimental shift in selectivity combined with our understanding of the achiral promoted reaction made us believe that catalyst could help discriminate between the ground state structures. From our reaction model (**Figure 24**) we can see that the phosphoric acid forms a pro-non anomeric complex that is 4.3 kcal/mol more stable then the pro-anomeric complex. The anomeric activation barrier though is 11.9 kcal/mol while the non-anomeric activation barrier is 14.9 kcal/mol. From our calculations it would appear that the anomeric complex becomes more favorable when the reaction begins to approach the transition state with an improvement in its selectivity by 3.3 kcal/mol.

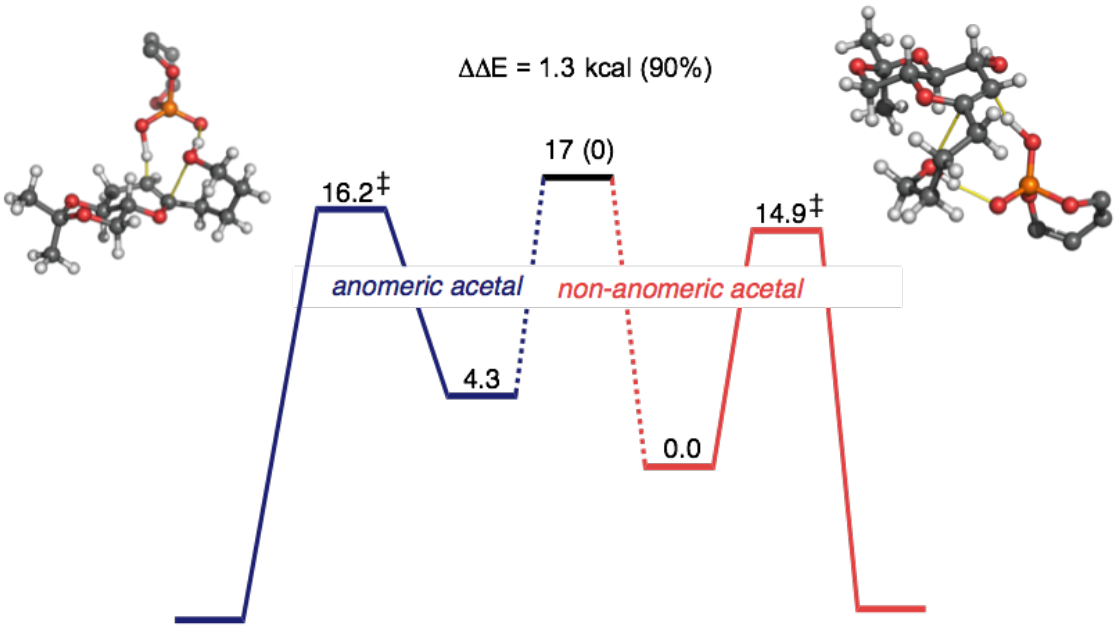

Figure 24. CPCM-M06-2X/TZVP//M06L/6-31g(d,p):UFF energy profile for the S-TRIP promoted glycal spiroketalization (kcal/mol).

The association energy of the substrate and catalyst is sufficiently favorable that we are left with a non-trivial energy barrier (17 kcal/mol) for the interconversion of the reactant complexes. Once entropy is taken into account this is much reduced, but still higlights the possibility for non-rapid interconversion of the two complexes leading to the different products. By comparing solely the TS energies we find that the non-anomeric TS is more stable by 1.3 kcal/mol, leading to a predicted product distribution of 93:7 (non-anomeric:anomeric). This is in agreement with the sense of experimental selectivity, although an overestimate of the 81:19 ratio. One possible source for this discrepancy is in the inherent CH assumption from using TS energies. When we calculate the rates by including the ground state effects, the selectivity for the non-anomeric drops by 14% leading to a product distribution that matches the experimental selectivity of 8:2 (Non-anomeric-Anomeric). If we assume that the reaction does not display classic CH behavior we can determine from the model that the phosphate catalyst promotes the anomeric product through ground-state de-stabilization while the non-anomeric is just the most stable ground state. This was also reflected in the simple phosphoric acid model studied in the Deslongchamps models. Just as before, we turned

to the distortion technique to derive the inherent driving forces for the non-anomeric formation.

The distortion-interaction (also known as activation-strain) approach analyzes the activation barrier in a bimolecular reaction in terms of unfavorable geometric distortion and favorable electronic interactions.[27] We applied the distortion-interaction technique to the study of the reaction above, in which the substrate geometry was retained by was separated from the catalyst at various points along the reaction coordinate. When we utilized this technique on the spiroketal reaction we found that the D-glycal with the acetonide protecting groups and substitute C-3 carbon showed a greater preference (1.7 kcal/mol) for the nucleophile to be positioned on the non-anomeric face (**Figure 25**). As the reaction progresses, the unfavorable distortion of the ring induced greater strain in the anomeric conformation then the non-anomeric, culminating in a difference of 2.9 kcal/mol between the conformations. This is offset by interactions with the catalyst, however, it can be seen that the substrate is able to adopt a more favorable conformation in forming the non-anomeric product.

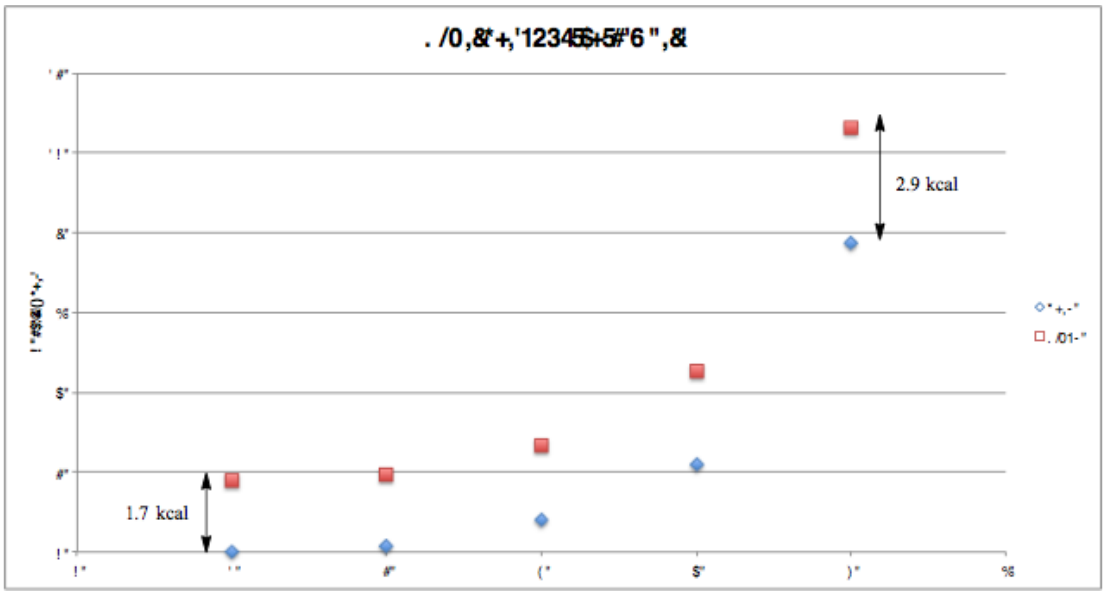

Figure 25. Substrate distortion energy M06L/6-31g(d,p) along the reaction coordinate approaching the TS. Beta and alpha refer to non-anomeric and anomeric configurations, respectively.

This trend that we find in our current study is different then what we expected from Deslongchamps' study, which showed that the anomeric distorted transition state, was more stable as a result of the half-chair like structure. The acetonide protecting group in this case rigidifies the ring, which potentially alters this conformational preference. As we had seen previously, the non-anomeric conformation is distorted from a half-chair to an envelope conformation which allows the adjacent acetonide protected 4,6 alcohols to maintain a chair conformation. The anomeric trajectory adopts a distorted half-chair conformation but still maintains the chair conformation of the acetonide ring. As the reversal of the prior trend was not the distortion of the acetonide ring we investigated possible interactions with the C-3 alcohol to induce the reversal. From the structural investigation we find in the anomeric trajectory the C-3 alcohol displays marginal staggered overlap with the C-4 hydrogen (35), as the reaction progresses this dihedral decreases to 25 which would lead to increased 1,3 di-axial strain. In the non-anomeric trajectory we find that the dihedral angle is 50 and there is no change in this overlap as the conformation is altered to the envelope. This could help explain the non-anomeric stability shown in the global trend found in the substrate distortion (**Figure 25**).

This increase in strain should result in the acceleration of the non-anomeric reaction resulting in only the non-anomeric product being formed. From the reaction profile (**Figure 26**) we can see that the anomeric trajectory has a lower activation barrier, which could only be attributed to a minimization of unfavorable contacts between the catalyst and reaction trajectory. When we investigated the intermolecular interactions between the catalyst and substrate, we could see that the favorable interactions at the initial ground state were intensified by 2.6 kcal/mol, culminating to the 4.3 kcal/mol difference between ground states. As the reaction commenced, interactions with the non-anomeric transition state either created greater unfavorable interactions or the catalyst reduced the unfavorable intermolecular interactions with the anomeric reaction trajectory. To investigate the possible interactions we compared the images generated from our computational investigation.

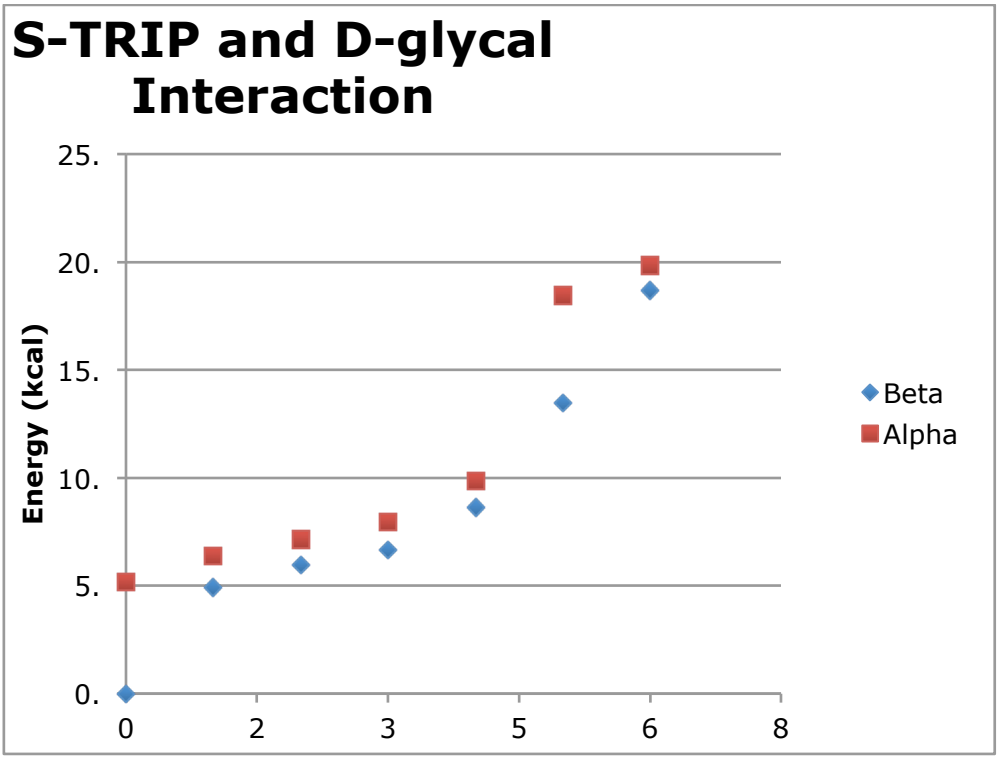

Figure 26. Reaction energy (M06L/6-31g(d,p)) along the reaction coordinate approaching the TS. Beta and alpha refer to non-anomeric and anomeric configurations, respectively.

The non-anomeric substrate shows strong steric interaction between the Pro-S C-11 and C-10 hydrogens in the substrate; with close contacts of 2.45 Å and 2.39 Å, respectively. The anomeric configuration displays greater steric interaction between the C-3 axial ring hydrogen and the catalyst in the substrate complex. These interactions are subsequently relieved when the substrate transverse to the TS. The steric interactions involved in the recognition of the anomeric face induced a conformational change resulting in the eclipsed interaction discussed previously between the C_3-OH and C_4-H. C-O formation is more advance in the anomeric TS, indicative of a later structure, which is consistent with the greater distortion energy of the substrate along this pathway as demonstrated earlier.

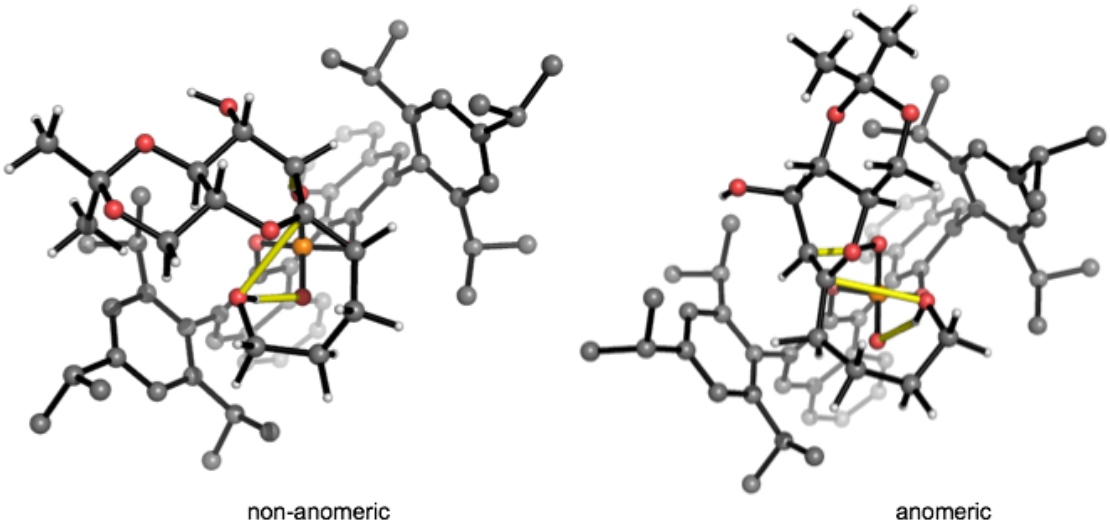

Figure 27. (S)-TRIP promoted spirocyclization TS structures.

3.3.3 Natural Product Motifs

To investigate the impact of the acetonide group in the above case, as well as a possible application to natural product synthesis we decided to focus on a substrate where this functionality has been replaced by an alkyl substituent. We computed the competing TS structures for three different subtrates, finding the opposite (anomeric) selectivity in each case. Based on these results we can deduce that glycal has a significant effect upon selectivity in the above case, presumably due to the large size which leads to steric interactions with the catalyst.

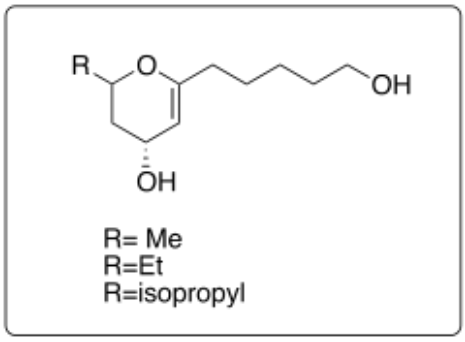

Substituent, R	Conformation	Selectivity

Me	Anomeric	99%
Et	Anomeric	81%
Isopropyl	Anomeric	97%

Figure 28. CPCM-M06-2X/TZVP//M06L/6-31g(d,p):UFF investigation of the TRIP application to the synthesis of Non-anomeric natural products.

3.3.4 D-Glycal Spiroketalization Promoted by (R)-TRIP

We found in this initial investigation that the population of the major product is correlated to the major intermediate. It is difficult to assess how quickly the reactant complexes interconvert, and it remains possible that a non-rapid equilibrium occurs. From our distortion calculations and structural investigation we could quantify and pinpoint the origins of selectivty as a direct result of conformational changes induced when the phosphate binds to the ring. I would argue that the C_3-OH and C_4-H eclipsed interactions are a direct result of introduction of the acetonide ring resulting in alterations to conformational landscape (Cremer-Pople projection).

To understand more about the origins of chiral recognition, we explored the spiriketalization of the same substrate promoted by the catalyst enantiomer. Experimentally this (R)-TRIP catalyzed glycal spiroketalization showed a 1:2 selectivity in favor of the anomeric product. From our previous model and our interpretation that the phosphate catalyst recognizes and stabilizes the non-anomeric conformation we envisaged that two scenarios could account for the experimental selectivity: firstly, (and more likely) the enantiomeric catalyst preferentially recognizes the anomeric TS and secondly, that ground state effects could affect the ability to interconvert between the two reactant complexes. When we modeled the reaction (**Figure 29**) we found the former case appeared to represent the experimental outcome the best, with the anomeric TS now being energetically favored. The selectivities for

the two catalyst enantiomers are opposite, but not equal since the substrate itself is chiral.

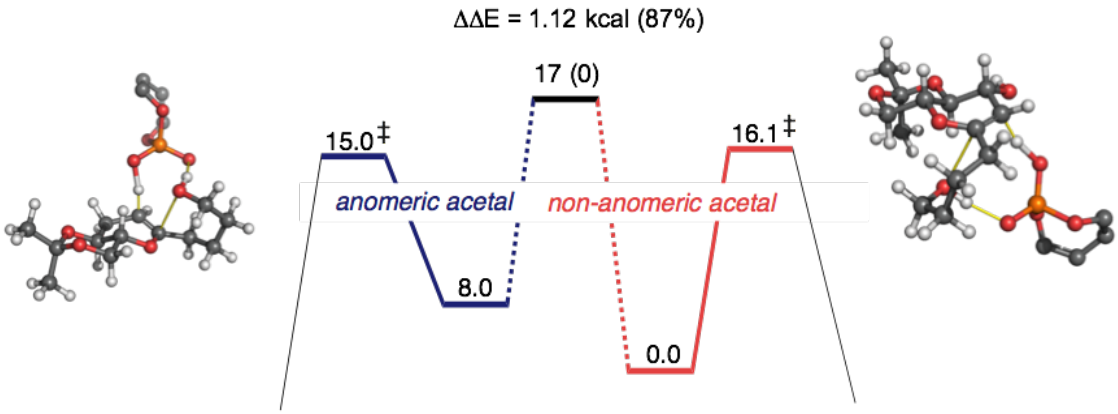

Figure 29. CPCM-M06-2X/TZVP//M06L/6-31g(d,p):UFF energy profile for the R-TRIP promoted glycal spiroketalization (kcal/mol).

The non-anomeric reaction course displayed a more stable catalyst complex by 8 kcal/mol, which alone means that the recognition of the ground state has improved by 3.7 kcal/mol and the anomeric activation barrier has decreased by 4.9 kcal/mol relative to the S-TRIP ligand. As discussed earlier, if we can assume interconversion of the reactant complexes (i.e. the CH principle) then it is possible to compute selectivity for the anomeric product, which is 7:1. This overestimates the experimentally observed selectivity of 2:1 although agrees with the sense of selectivity. If the reaction profile were treated as being in a non-rapid equilibrium we would find that the predicted selectivity would be 75% or 3:1 for (Ano :NA) which is more accurate then the C-H model.

Investigating the structural characteristics of the ring we find that the conformation has not drastically changed relative to the S-catalyst case. The only change worth noting is the decrease in the 1,3 strain in the anomeric trajectory. The diaxial strain that we had noted previously has decreased (40-30) *versus* (35-25) for the S-Catalyst. When we investigated the non-anomeric GS and TS structure it became apparent that the 1.1

kcal/mol increase could be from the non-favorable interaction between the carbon chain of the nucleophile and the catalyst (**Figure 30**). For the interactions highlighted, the proximity between the substrate and catalyst increases by 0.15 Å as the reaction proceeds to the TS.

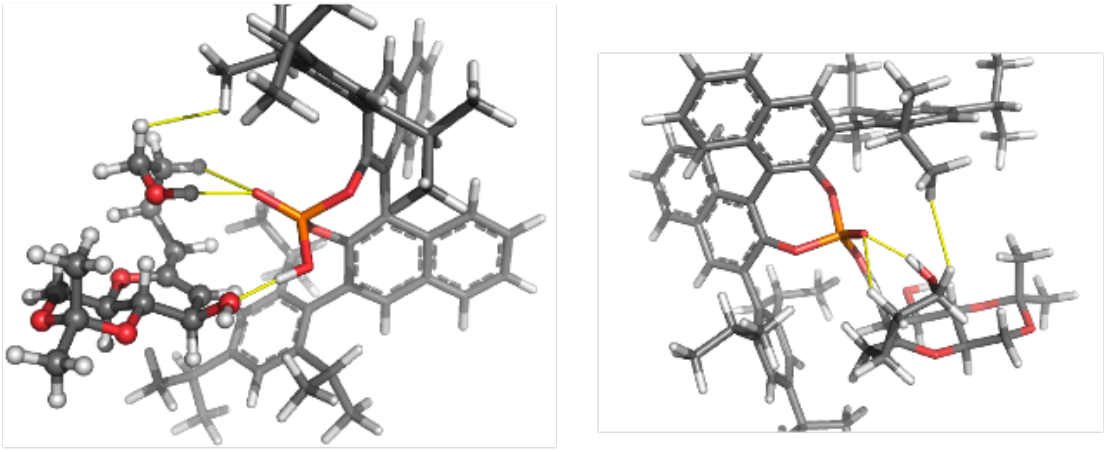

Figure 30. Left hand side, substrate complex; Right hand side, TS for the non-anomeric product.

This increase in steric interactions could help explain the relative acceleration of the anomeric reaction course. To obtain a better structural understanding for the selectivity changes with the R-catalyst we decided to investigate the anomeric structure to determine if there is any intermolecular strain relief as the TS is approached. The structure highlights that there are three steric intermolecular interactions with the GS that are < 2.4 Å away. As the reaction course transpires these unfavorable interactions are relieved resulting in the acceleration of the pathway through ground-state destabilization (**Figure 31**).

Substituent	**GS-Cat Dist. (Å)**	**TS-Cat Dist (Å)**

Me (1)	2.40	2.50
C-3 H (2)	2.39	2.43
C-3 OH (3)	2.40	2.80

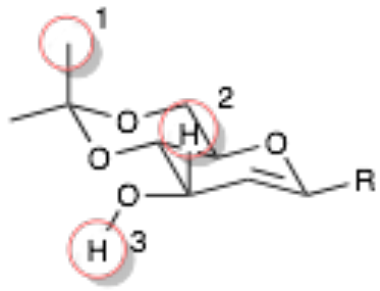

Figure 31. A decrease in the interactions with the substrate led to an acceleration of the reaction to promote the anomeric reaction course.

3.3.5 D-Glycal Spiroketalization Conclusions

The (*R*) and (*S*)-TRIP promoted spiroketalization from the glycal substrate highlights the impact of the ground-state and transition state recognition. As we have seen previously, the initial recognition of the ground state is able to modulate the kinetics of the catalyst leading to either a co-operative effect, GS and TS, both stabilized and accelerated or a negative impact where the ground state is recognized but not the geometry of the transition state. These classical issues for the case of non-rapid equilibrium kinetics is seen in enzyme catalyst where the ultimate impact has been correlated to the "catalytic competence" where the correlation between activity and recognition helps determine which form of the catalyst will dominate in a mixture. The D-glycal system we studied was restricted in the number of conformations that the substrate could adopt. If these restrictions were removed then one would expect to find that the selectivity of the reaction would be complicated by number of binding interactions that the catalyst-substrate can adopt (**Figure 31**). By studying the enantioselective spiroketalization of the enol ether by (S)-TRIP, (S)-9-Anthryl-

substituted CPA and (*R*)-VAPOL we sought to understand more fully the interactions controlling the product distribution.

3.3.6 Enantioselective Spiroketalization promoted by TRIP

As we have seen from our D-glycal model the rate-determining step was the proton transfer from the phosphate and the predicted selectivity was heavily dependent on the discrimination of the substrate. The D-glycal though is special as the iso-acetonide protecting group froze the structure resulting in a restriction in the conformational distribution. In contrast, the enantioselective substrate can adopt two different ground-state conformations that we have subsequently labeled **(R/S)-Ano** and **(R/S)-NAno** (Figure **32**), which denotes the product chirality and conformational outcome respectively.

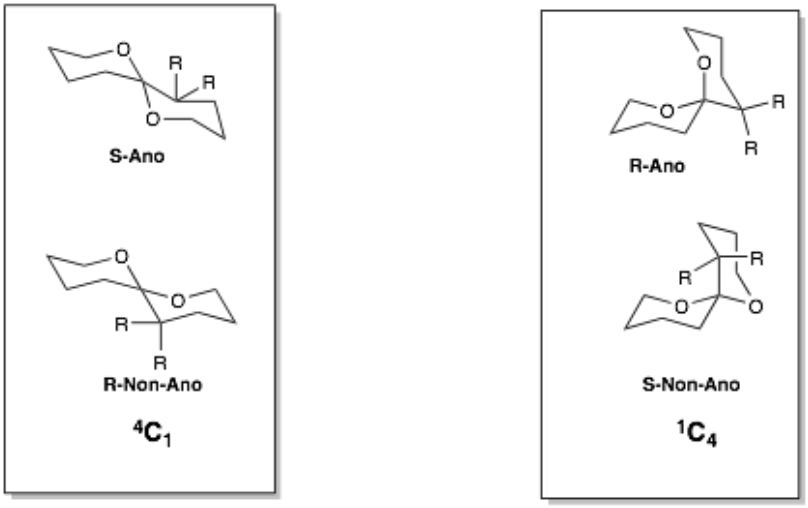

Figure 32. The conformations that can be adopted during the spiroketalization process.

Classically this ring flipping should only have a limited effect on the selectivity outcome but as we have seen thus far the phosphate catalytic behavior appears not to follow the rapid equilibrium model. The initial coordination of the catalyst has a significant outcome on the predicted selectivity. We would expect that multiple conformations of substrate could have drastic results on the predicted

enantioselectivity. In this current model, the steric bulk has shifted from the glycal to the nucleophile, which has been shown to have greater steric interactions with the catalyst. We believed that this steric bulk increase could result in different catalyst conformations being adopted. The most prominent competitor would be the S_Ni mechanism that we had discussed earlier, subsequently known as mono-pathway and the traditional mechanism of the discrete separation of the general acid/base acidity is subsequently known as the bi-pathway (**Figure 33**).

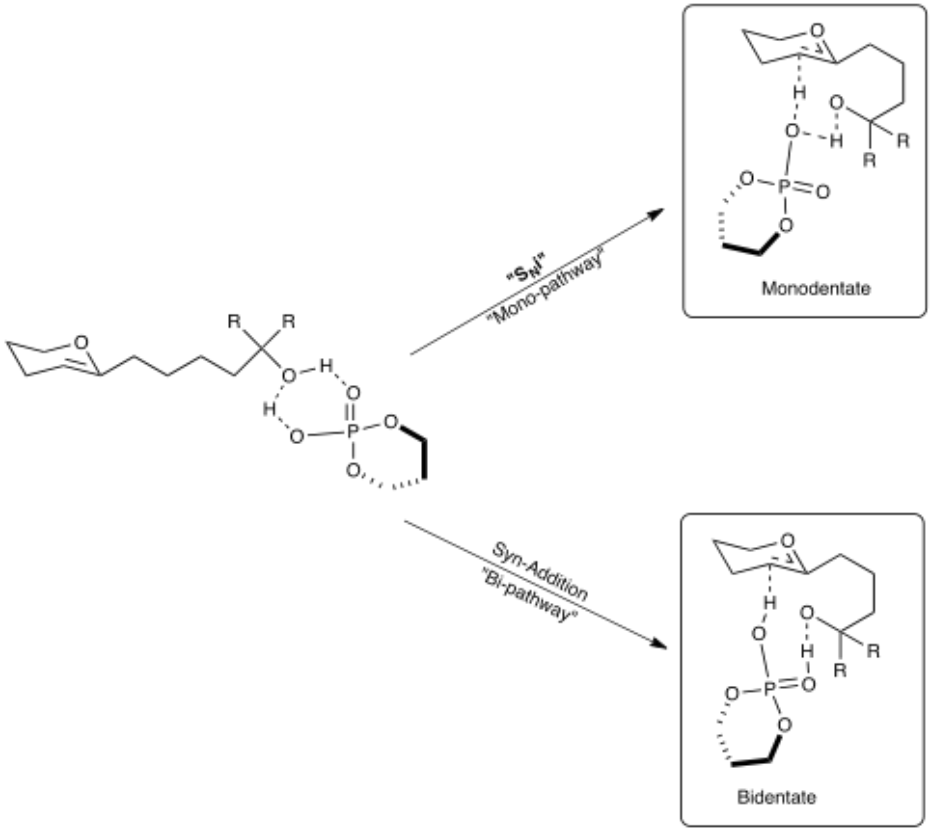

Figure 33. The different conformations the catalyst can adopt which can show different outcomes.

One would expect that the S_Ni mechanism could accommodate the increased steric bulk of the substrate while providing a similar general acid/base activity in the transition state. The benefit of the alternate pathway could be extended to include possible increase in the Brønsted acidity, which should result in an earlier transition state. As it would be difficult to experimentally determine the Brønsted acidity changes of such a

pathway we can utilize the transition state structure to determine whether the extent of proton transfer has qualitatively increased or decreased.

From our previous calculations we found that the TRIP phosphate is discriminating between the enantiofaces based on ground state recognition. With the S-TRIP catalyst, Nagorny and co-workers found that the spiroketalization displayed a 92% ee for the S enantiomer. From the reaction profile we are able to see that the TRIP ligands are again discriminating between the pro-R and pro-S ground states, promoting a more stable interaction with pro-S complex by 1.1 kcal/mol (**Figure 34**) resulting in a predicted 97% ee for the S enantiomer.

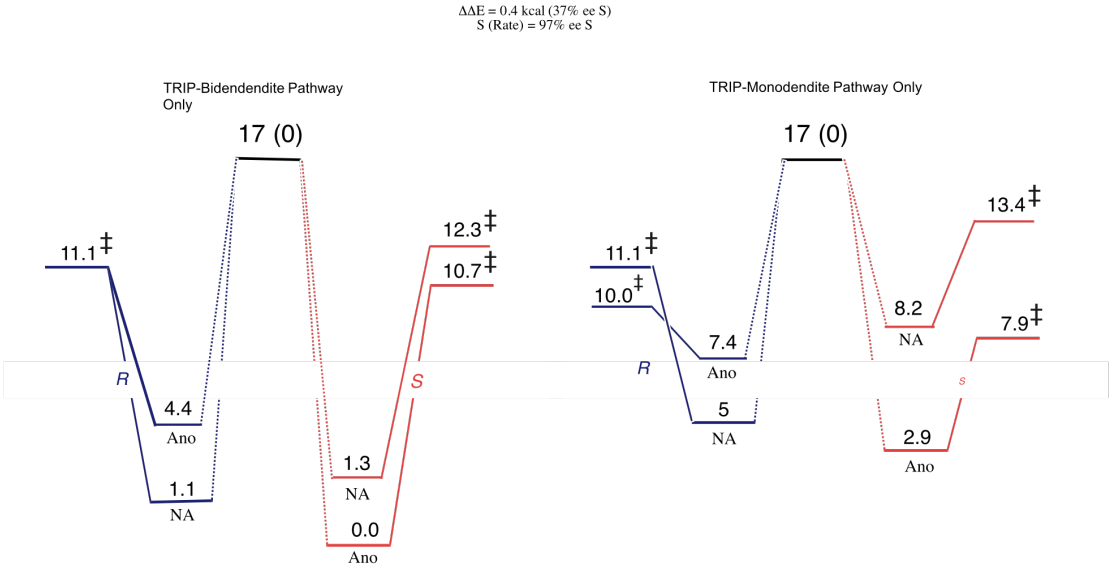

Figure 34. Activation barrier in Red and Substrate energy difference with S-Ano Bi in Blue. NA= Non-anomeric, Ano=Anomeric, Bi=Bidentate pathway, and Mono= Monodentate pathway.

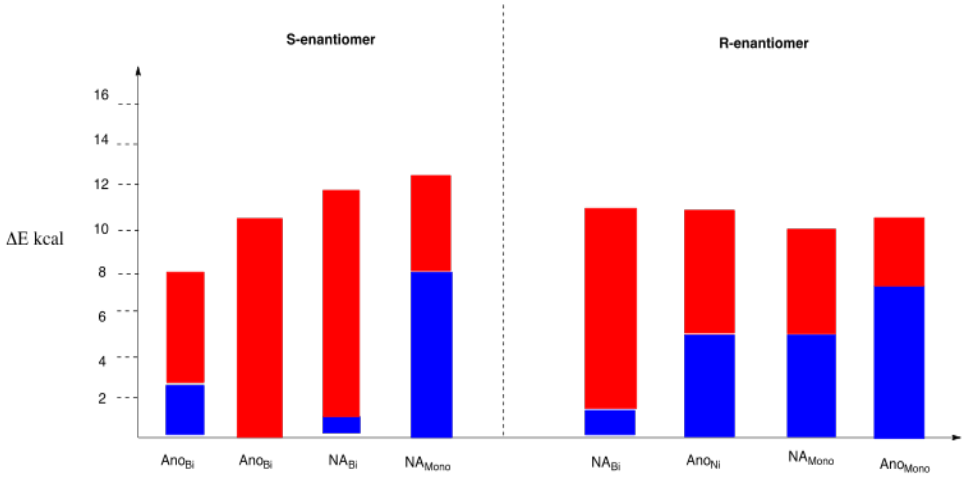

Figure 35. A simple representation of the Figure above. Blue bar represents the difference in ground state energy and the red bar represents the activation barrier for that reaction course.

If the reaction was under a rapid-equilibrium we would expect that the mono$_{Anomeric}$-pathway in the both the *R* and *S* case to be the dominate catalytic species resulting in a difference of 3.6 kcal/mol for the enantiomers or a selectivity factor of 2248. This would be significantly greater then the observed selectivity of 97% ee. As the mono-pathway is highly selectivity for the *S* enantiomer we could expect that our initial proposal for the mono-pathways existence could lead to erroneous results. To reassure ourselves of a possible existence we compared; The Bi-pathway predictions alone and the S Bi and Mono structures.

As there is no current structural information or kinetic data our best course of determining the validity of our proposal is to use competitive models correlating the observed competitive kinetics (e.e). The competitive argument against our model is the Bi-pathway structures are the dominant active catalytic species in the solution. Based on this model we would find that the enantioselectivity for the reaction under rapid equilibrium would be 37% for the *S*-enantiomer and under non-rapid equilibrium 11% for the *S*-enantiomer (Figure **35**). In the *S* enantiomeric Bi pathway we find that the transition state leading the anomeric product is 1.51 kcal/mol more stable then the non-anomeric pathway and anomeric ground state is more stable by 1.3 kcal/mol. In comparison the *R*-enantiomer Bi-pathway doesn't show drastic discrimination between the anomeric and non-anomeric pathways.

When investigating the interactions between the catalyst and the substrate we found that the mono pathway became more favorable by 1.6 kcal/mol (4.2-2.6) as the reaction transitioned. The inherent substrate preference was 0.2 kcal/mol in favor of the mono-pathway meaning that phosphate catalyst induced 1.6 kcal/mol more unfavorable interactions between the bi-anomeric transition state and the catalyst then that of the mono-pathway (Figure **36**).

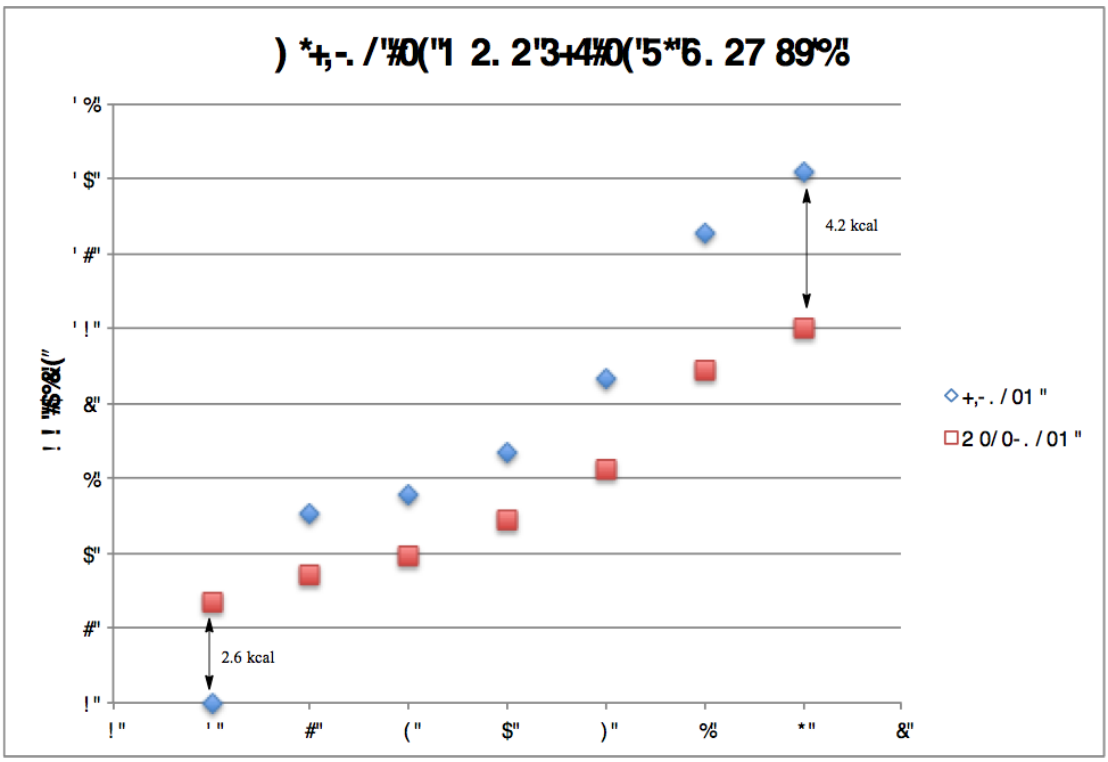

Figure 36. Difference in the interactions between the catalyst and substrate as the reaction progresses to the transition state.

By investigating the substrate structures we can see that a prominent contribution to the 2.6 kcal/mol (DH) difference is caused by the different hydrogen bonding interactions in the ground state (Figure **37**).

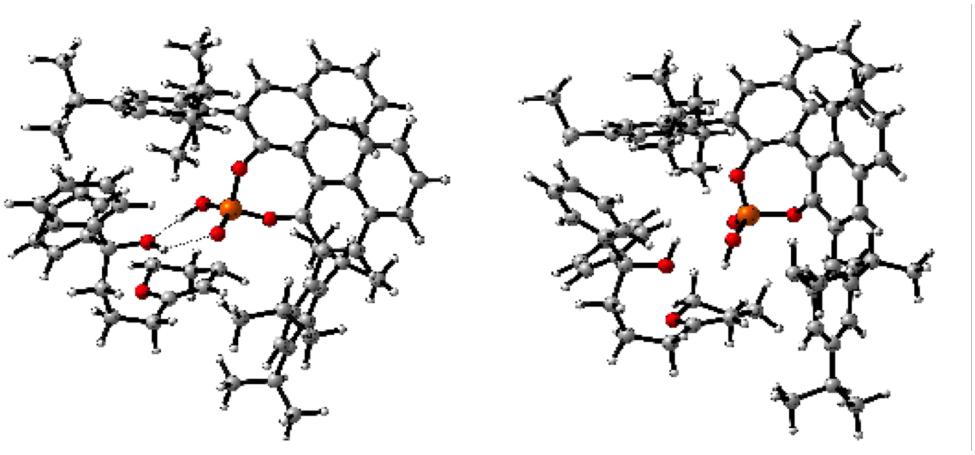

Figure 37. Substrate binding in the S-Ano Bidentate and monodentate conformations.

The bidentate pathway is able to induce two hydrogen bonds with its substrate while monodentate is unable to replicate this interaction. In the transition state though, both binding modes have the same number of hydrogen bonds. The bidentate complex on the other hand needs to break one hydrogen bond leading to the dramatic change in the energy of the reaction trajectory as seen in the (Figure **37**). As we reach the transition state we find that mono-pathway is able to replicate the hydrogen bonding network and minimizes unfavorable interactions because the substrate doesn't need to penetrate into the active site as far as in the bidentate case. We believe that the 1.3 kcal/mol (2.8 kcal/mol including ZPE correction) change in favor of the mono-pathway is caused by the dissolving contacts with the catalyst.

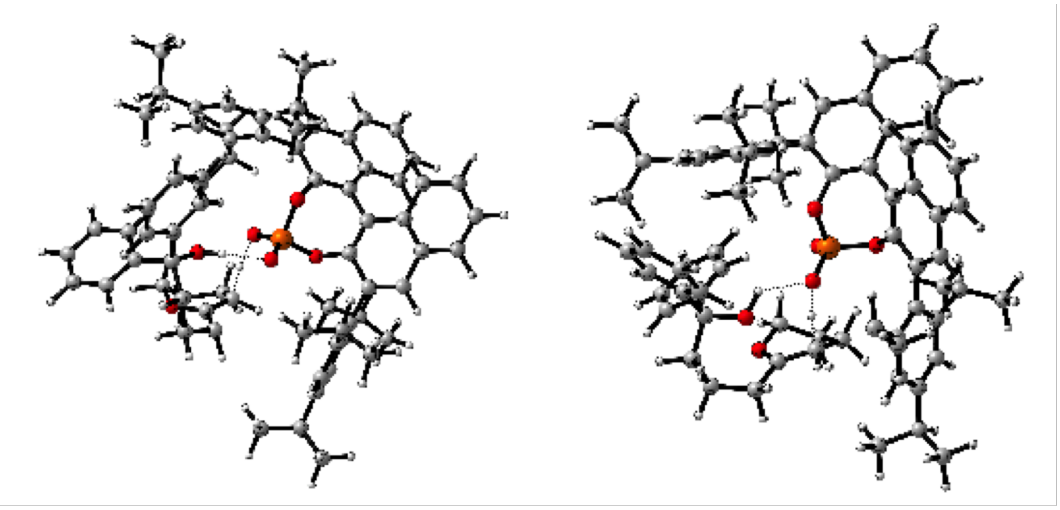

Figure 38. Transition states in S-Ano bidentate and monodentate pathway (portions removed for clarity).

The classical technique to deconvolute a complex mechanism is to utilize a labeled substrate that can act as a marker in the products to help determine a plausible movement of the electrons. Another route is to introduce a chiral center to abrogate some of the reaction trajectories or to determine RDS order; scrambling of chiral centers and match/mismatched pairing.

In the catalyst case, kinetic resolution is very useful as the introduction of chiral centre will lead to matched and mismatched interactions with the active catalyst complex. The effect of this mismatch pairing results in either a raising of the ground state and/or the raising of the transition state for the non-complementary pairs. With the aid of the structural models generated from the computational investigations the researcher can be more judicious with the functionalization of the substrate to perturb the more sensitive portions of the catalyst. In our case we would expect that pre-functionalization would not only promote a matched and mis-matched model, but more importantly we could expect that the conformational population to alter. As we demonstrated in our previous model for the bi-pathway case, the *R*-enantiomer would be unaffected by substitutions that altered the conformation population of the substrate while the S-enantiomer

pathway would be more sensitive. Based on the structural analysis of the transition state we would expect that alterations at C-5 would induce the conformational perturbation without introducing steric interactions that could lead to a substantial erroneous result. .

Thus far, we have seen that the interactions at the ground state will not only change the kinetics of the reaction but as well the possible binding interactions/activation models. As we have seen the drastic changes in the reaction selectivity's as the catalyst have change has been caused by subtle shifts in the ground state recognition. To understand this effect further we investigated the reaction again but promoted by a different the 9-Anthracenyl-phosphate catalyst.

3.3.7 Enantioselective Spiroketalization promoted by 9-Anthracenyl-substituted CPA

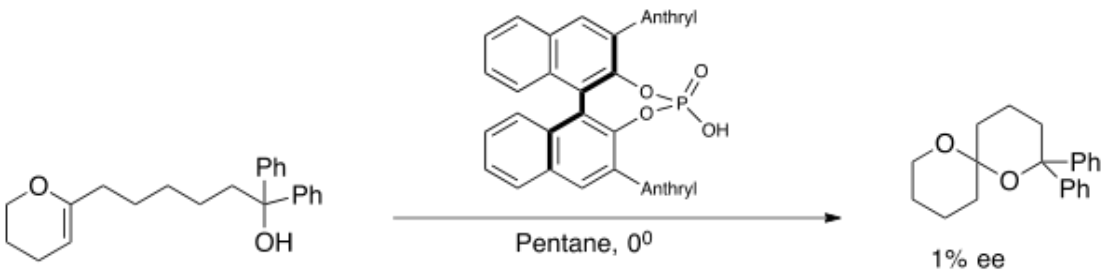

Figure 46: Reaction outcome of the 9-Anthryl phosphate promoted spiroketalization.

The erosion of the enantioselectivity or even the flipping of the selectivity induced by simple alterations of the ligands has always been perplexing. From our models we believe that the selectivity shifts could be induced by changes in the stability of the catalyst substrate complexes. To establish the interactions that induce the erosion of the ee from 90% to 1% we modeled the reaction for (S) 9-Anthracenyl, (1% ee under un-optimized conditions). From the reaction profile that we calculated, we predicted that the enantioselectivity would be 10% for the *R* enantiomer. Our calculations were able to predict and reflect the significant erosion shown experimentally, 1% ee.

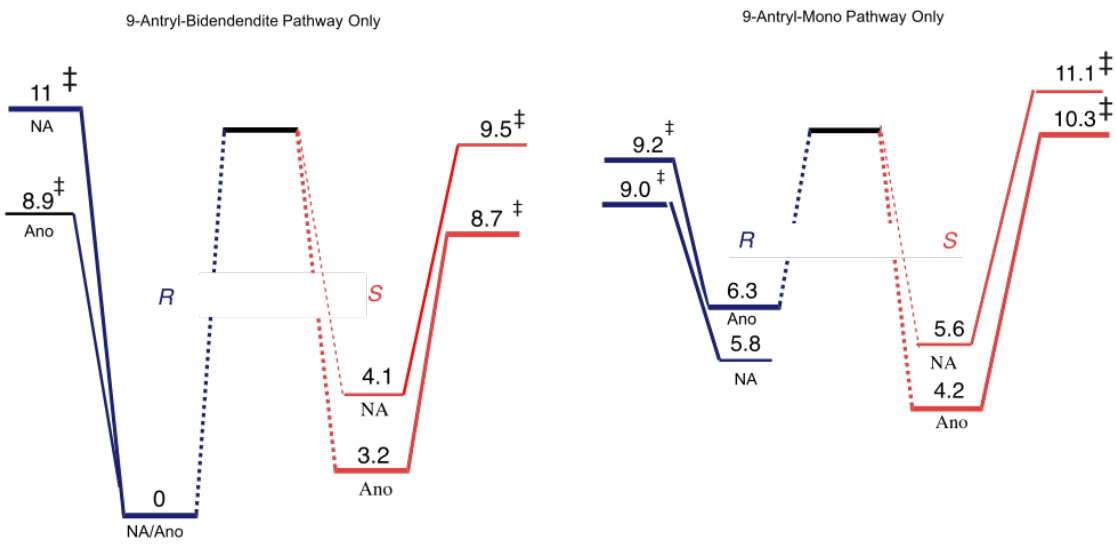

Figure 47. Reaction outcome for the S-9-Anthracenyl Phosphate promoted spiroketalization.

In this case, the *S*-9-Anthracenyl catalyst recognizes pro-R substrate and forms a 3.2 kcal/mol more stable complex then with the Anomeric pro-Si substrate. The catalytic mechanism using *S*-9-Anthracenyl seems to have altered as well. In this model, the Mono-dendrite pathway has a limited effect on the selectivity of the reaction. This could have been derived from the 9-Anthracenylcatalyst having greater a greater spatial opening but limited protrusion into the active site. This limited protrusion would allow the spiroketal to penetrate deeper into the active site while mitigating the steric interactions seen in the TRIP acid case.

With these two catalysts we can now investigate the modeling effects of comparing just the transition state versus the rates. If we were comparing just the transition states, we would find that the predicted enantioselectivity only changes by 15 % when we change the ligand from TRIP (35% ee) to 9-Anthracenyl. One could argue that alterations of the steric environment coupled to shifts in the transition state position could result in the 1kcal/mol shift in favor of the R enantiomer. With an earlier transition state we would believe that the discrimination between the enantiomers would decrease since they are further away from the steric interactions with the ligands. This effect coupled to the new steric environment would result in the seen erosion. For this case to hold we would expect that the 9-Anthryl is more acidic resulting in a lowering of the activation

barrier causing the transition state to shift earlier. For our theory we are assuming that the catalyst only effects the intrinsic barrier and not the thermodynamic difference as the shift in the thermodynamic difference itself would induce a change in the transition state position (Figure **48**).

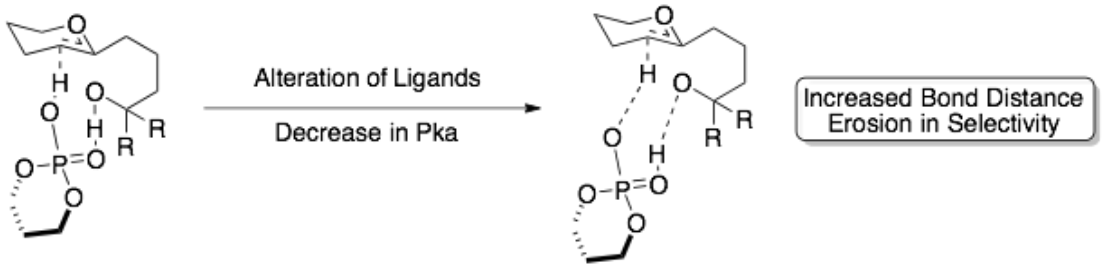

Figure 48. The impact of ligand alteration of the pKa of the catalyst and the possible erosion in the transition state.

The position of the transition state was shifted later by 0.02 Å when the *S*-TRIP ligand was switched to the *S*-9-Anthracenyl. Since the transition state stayed roughly the same we could conclude that the erosion of the enantioselectivity was not directly correlated to changes in the transition state. An alternate explanation that follows this trend is that the enantioselectivity is not only linked to the difference in the activation barriers, but as well the to initial ground state distribution. The results from our models highlight support an argument that the reaction is in a non-equilibrium situation resulting in the most stable species dominating the product distribution. As we have highlighted previously, the myriad of reactions that phosphoric acids catalysts could result from an even more complex number of mechanisms that the acid could support. In this instance we found that the enantioselectivity was derived manly from a combination of catalyst-substrate and transition state interactions. This type of mechanism and the subsequent kinetics (non C-H behavior) could help to explain some of the difficulty in predicting the outcome of phosphoric acid reactions as the substrate begins to deviate from the control study. To investigate this further we decided to remove a control present in this study (the intramolecular reaction) and study an intermolecular reaction where not only kinetics, order vs. non-ordered, can play a role but as well the number of binding conformers can impact the selectivity of the reaction.

3.3.8 Enantioselective Spiroketalization Conclusions

Based on extensive study of the spiroketalization reaction we have found that within bulk solvent, the reaction is promoted through a *syn*-addition involving a general acid mechanism. The phosphate catalyst replicates this effect but because of the bulky structure another possible interaction that can be characterized as Sn_i is able to dominate the reaction course. The general base mechanism promotes the reaction to resemble an S_n2-like reaction course resulting in a very low activation barrier as compared to the ground state equilibrium. This relatively slower equilibrium results in the phosphate catalyst displaying non-CH behavior. This has been highlighted in all three catalyst cases where the dominant product or the erosion of selectivity could be explained through the recognition of one ground state over another.

The kinetic effects of phosphate enantioselective synthesis have not been explored in the literature to the same extent as qualitative transition state recognition. The extent and impact of the kinetic effects surrounding the control of enantioselectivity will be further explored in the more complicated intermolecular desymmetrization of meso-epoxides.

3.4 References

1. (a) Navarro, G.; Cheng, A.T.; Peach, K.C.; Bray, W.M.; Bernan, V.S; Yildiz, F.; Linington, R.G. *Antimicrob. Agents Ch.,* **2014**, 1092.; (b) Peach, K.; Bray, W.M.; Winslow, D.; Linington, P.; Linington, R. *Mol. Biosyst.* **2013**, 9, 1837.
2. Pereira, M.; Blanchard, J,; Murphy, C.; Roderick, S.; Brown, E. *Antimicrob. Agents Ch.,* **2009**, 6, 2306
3. Tan, X.; Hu, L.; Luquette, L.; Gao, G.; Liu, Y.; Qu, H.; Xi, R.; Lu, X.; Park, P.; Elledge, S. *Nat. Biotechnol.* **2012**, 11, 1125.
4. Geysen, M.; Schoenen, F.; Wagner, D.; Wagner, R. *Nat. Rev. Drug Discov.,* **2003**, 2, 222.

5. (a) Perez, M.; Baig, I.; Brana, A.; Salas, J.; Rohr, J.; Mendez, C. *ChemBioChem,* **2008**, 9, 2995; (b) Choi, K.; Brimble, M. *Org. Biomol. Chem.,* **2009**, 7, 1424; (c) Kulkarni, B.; Roth, G.P.; Lobkovsky, E.; Porco, J. *J. Comb. Chem.* **2002**, 4, 56.
6. Aho, J.; Pihko, P.; Rissa, T. *Chem. Rev.,* **2005**, 105, 4406
7. Aho, J.; Piisola, A.; Krishnan, S.; Pihko, P. *Eur. J. Org. Chem.* **2011**, 1682
8. Liu, G.; Wurst, J.M.; Tan, D.S. *Org. Lett.,* **2009**, 11, 3670.
9. Zhang, T. *Chem. Rev.,* **2006**, 106, 2583.
10. (a) Rodriguez, R.; Steed, D.; Kawamata, Y.; Su, S.; Smith, P.; Steed, T.; Romesberg, F.; Baran, P. *J. Am. Chem. Soc.* **2014**, 136, 15403; (b) Villaume, M.; Sella, E.; Saul, G.; Borziller, R.; Fargnoli, J.; Johnston. K.; Zhang, H.; Fereshteh, M.; Dhar, T.; Baran, P. *ACS Cent. Sci.*, **2016**, 2, 27; (c) See, Y.; Herrmann, A.; Alhara, Y.; Baran, P. *J. Am. Chem. Soc.* **2015**, 137, 13776; (d) Jin, Y.; Yeh, C.; Kuttruff, C.; Jorgensen, L.; Dunstl, G.; Felding, J.; Natarajan, S.; Baran, P. *Angew. Chem. Int. Ed.*, **2015**, 54, 14044.
11. (a) Beans, E.; Fournogerakis, D.; Gauntlett, C.; Heumann, L.; Kramer, R.; Marsden, M.; Murray, D.; Chun, T.; Zack, J.; Wender, P. *Proc. Nat. Acad. Sci.*, **2013**, 110, 11698; (b) DeCristopher, B.; Loy, B.; Marsden, M.; Schrier, A.; Zack, J.; Wender, P. *Nat. Chem.* **2012**, 4, 705.
12. (a) Seeman, J. *J. Chem. Ed.* **1986**, 42; (b) Perrin, C.; Seeman, J. *J. Org. Chem.,* **1984**, 49, 2887.
13. (a) Bures, J.; Armstrong, A.; Blackmond, D. *J. Am. Chem. Soc.* **2012**, 134, 6741. (b) Bures, J.; Armstrong, A.; Blackmond, D. *Acc. Chem. Res.,* **2016**, 49, 314 (c)Blackmond, D.; *J. Am. Chem. Soc.* **2015***, 137, 10852.*
14. Jencks, W.P. *Catalysis in Chemistry and Enzymology*, Dover Publications. New York (1986)
15. (a) Vaclavik, J.; Sot, P.; Vilhanova, B.; Pechacek, J.; Kuzma, M.; Kacer, P. *Molecules*, **2013**, 18, 6804; (b) Knowles, W.; Sabacky, M.; Vineyard, B.; Weinkauff, D. *J. Am. Chem. Soc.* **1975**, 97, 2567; (c) Stults, B.; Friedman, R.; Koening, K.; Knowles, W.; Greegor, R.; Lytle, F. *J. Am. Chem. Soc.* **1981**, 103, 3235; (d) Kiamura, M.; Tsukamoto, M.; Bessho, Y.; Yoshimura, M.; Kobs, U.; Widhalm, M.; Noyori, R. *J. Am. Chem. Soc.* **2002**, 124, 6649.
16. Daley, C.; Bergens, S. *J. Am. Chem. Soc.* **2002**, 124, 3680
17. Seeman, J. *Chem. Rev.,* **1983**, 83, 83.

18. Akiyama, T.; Morita, H.; Fuchibe, K. *J. Am. Chem. Soc.,* **2006**, 128, 13070
19. Wu, J.; Wang, Y.; Drljevic, A.; Rauniyar, V.; Phipps, R.; Toste, D. *Proc. Nat. Acad. Sci.*, **2013**, 110, 13729.
20. (a) Khomutnyk, Y.; Arguelles, A.; Winschel, G.; Sun, Z.; Zimmer, P.; Nagorny, P. *J. Am. Chem. Soc.* **2016**, 138, 444; (b) Sun, Z.; Winschel, G.; Borvika, A.; Nagorny, P. *J. Am. Chem. Soc.* **2012**, 134, 8074.
21. Pothier, N.; Goldstein, S.; Deslongchamps, P. *Helv. Chim. Acta*, **1992**, 75, 640.
22. (a) Stoddart, J. F. *Stereochemistry of Carbohydrates*, John Wiley and Sons Inc. New York (1971); (b) Deslongchamps, P. *Stereoelectronic effects in organic chemistry*, John Wiley and Sons Inc. (1983)
23. (a) Mahlau, M.; List, B. *Angew. Chem. Int. Ed.,* **2013**, 52, 518; (b) Mayer, S.; List, B. *Angew. Chem. Int. Ed.,* **2006**, 45, 419; (c) Jindal, G.; Sunoj, R. *J. Org. Chem.*, **2014**, 79, 7600
24. Wurst, J.; Liu, G.; Tan, D. *J. Am. Chem. Soc.* **2011**, 133, 7916
25. (a) Thompson, A.; Speciale, G.; Fernandez, J.; Hakki, Z.; Belz, T.; Cartmell, A.; Spears, R.; Chandler, E.; Temple, M.; Stepper, J.; Gilbert, H.; Rovira, C.; Williams, S.; Davies, G. *Angew. Chem. Int. Ed.* **2015**, 54, 5378; (b) Thompson, A.; Dabin, J.; Fernandez, J.; Ardevol, A.; Dinev, Z.; Williams, S.; Bande, O.; Siriwardena, A.; Moreland, C.; Hu, T.; Smith, D.; Gilbert, H.; Rovira, C.; Davies, G. *Angew. Chem. Int. Ed.* **2013**, 51, 10997.
26. Paton, R.; Kim, S.; Ross, A.; Danishefsky, S.; Houk, K. *Angew. Chem. Int. Ed.* **2011,** 50, 10366.
27. (a) Zeist, W.; Bikelhaupt, F. *Org. Biomol. Chem.*, **2010**, 8, 3118; (b) Green, A.; Liu, P.; Merlic, C.; Houk, K. *J. Am. Chem. Soc.* **2014,** 136, 4575
28. (a) Mollanen, S.; Potuzak, J.; Tan, D. *J. Am. Chem. Soc.* **2006**, 128, 1792; (b) Sharama, I.; Wurst, J.; Tan, D. *Org. Lett.* **2014**, 16, 2474.
29. (a) Lee, S.; Hong, S.; Errey, A.; Izumi, A.; Davies, G.; Davis, B. *Nat. Chem. Biol.* **2011**, 7, 631; (b) Trnka, T.; Kozmon, S.; Tvaroska, I.; Koca, J. *Plos Comp. Bio.,* **2015**,
30. (a) Hu, H.; Yang, W., *Ann. Rev. Phy. Chem.,* **2007**, 59, 573; (b) Lawan, N.; Ranaghan, K.; Manby, F.; Mulholland, A. *Chem. Phy. Lett.*, **2014**, 380; (c) Luk, L.; Pernia, J.; Dawson, W.; Roca, M.; Loveridge, E.; Glowacki, D.; Harvey, J.; Mulholland, A.; Tunon, I.; Moliner, V.; Allemann, R. *Proc. Nat. Acad. Sci.*, **2013**, 110, 16344.

31. (a) Paton, R. S.; Goodman, J. M. *J. Chem. Inf. Model.,* **2009**, *49*, 944-955; (b) Grimme, S.; Ehrlich, S.; Goerigk, L. *J. Comp. Chem.,* **2011**, 32, 1456.

Chapter 4. Chiral Phosphoric Acid-Mediated Desymmetrization of Meso-compounds

4.1 Introduction

4.1.1 Introduction

Our previous computations of the phosphoric acid promoted spiroketalization showed a strong correlation between the lowest energy ground state and chirality of the product. This type of behaviour could suggest a non-rapid equilibrium between ground state structures leading to enantiomeric products, where the catalyst would discriminate between the TS and the GS. This should cause us to approach the comparison of TS structures alone with caution (as in the standard Curtin-Hammett scenario) in computing levels of catalytic enantioselectivity. The effects of the pre-equilibrium, or lack thereof, can have a significant impact on the observed selectivity in experiment. As an example, while asymmetric metal-catalyzed hydrogenations often exhibit Curtin-Hammett type behaviour, it is also well known there is a strong correlation between hydrogen gas pressure and the efficacy of Noyori Asymmetric hydrogenation.[1] The subsequent slowing of the hydrogen splitting has a global effect on the observed enantioselectivity by resulting in a slowing of the rapid equilibrium.[2]

Focusing on catalysis with chiral phosphoric acids (CPAs), a limited number of contacts (i.e. steric or Van der Waals interactions) occur between catalyst and substrate and this may result in rapid pre-equilibrium. As we have seen with the spiroketalization, binding orientations that were initially not investigated had a significant impact on the kinetics of the enantiomer pathways. As the complexity of the mechanism increases i.e ordered vs. non-ordered kinetics, we could expect the correlation between calculated behavior and observed kinetics would be to complex to derive. What we could find if we choose an inappropriate reaction is that the pre-equilibrium kinetics will dominate the observed behavior of the catalyst.

To investigate enantioselective catalysis with CPAs we decided to focus on the asymmetric kinetic desymmetrization of cyclohexene-oxide. Here, a meso compound (the epoxide) can undergo ring-opening with benzoic acid acting as nucleophile, with the CPA acting as the source of enantioinduction. This reaction is attractive for computational study due to the relative rigidity of both reactants, which decreases the computational cost by restricting the number of possible conformations.[3] Prior experiments reported by List and co-workers have established that the initial binding event is the complexion of benzoic acid and phosphoric acid to form an active dimer, which acts as a chiral nucleophile.[4] As this reaction operates with an excess of benzoic acid we can be confident that this chiral dimer is the catalyst resting state of the asymmetric transformation, as shown in (**Figure 1**).[5] Based on the bifunctional nature of the catalyst, and computational precedent for catalytic modes of action, we generated a working hypothesis that both nucleophile and electrophile would be activated in the stereodetermining TS.

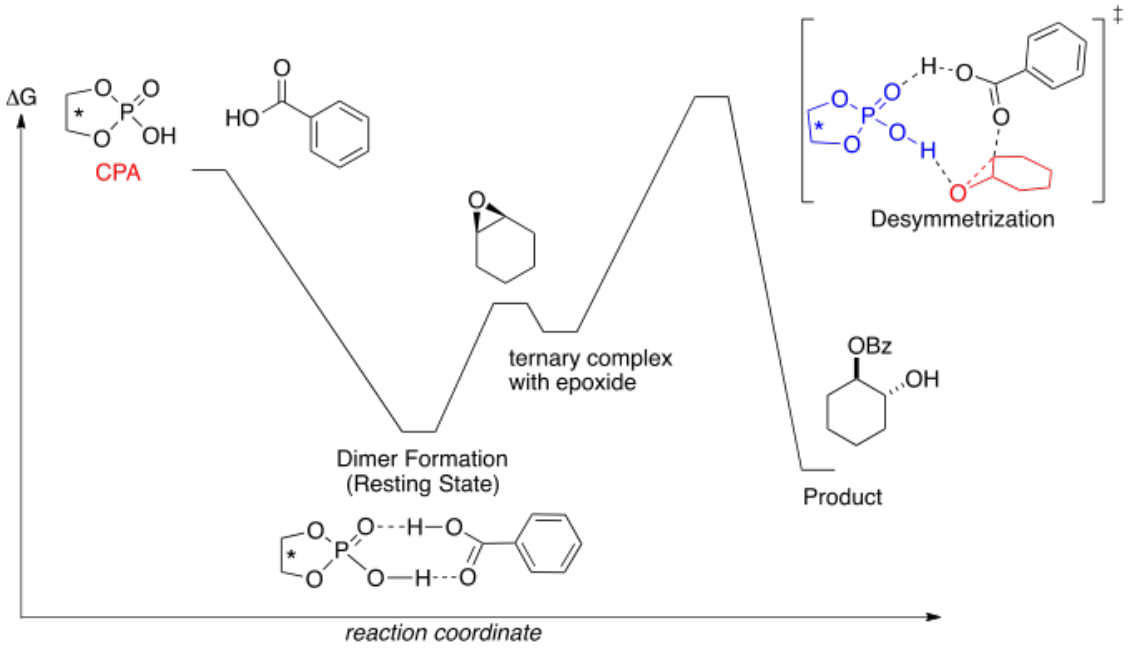

Figure 1: Qualitative reaction profile showing that in the catalytic process the most stable intermediate (Dimer Formation) is the resting state of the catalyst.

4.1.2 CPA Bi-functional Activity

Earlier computational studies performed separately by Terada, Simón and Goodman and Himo have highlighted that for many reactions the CPA interacts with both nucleophile and electrophile by hydrogen bonding interactions.[6] The net result is the

creation of a well-ordered TS structure with a defined environment to ensure chiral discrimination occurs. The general acid/base activity of the catalyst promotes a controlled transition state which has enabled these researchers to make accurate models to predict the stereochemical outcome from the reaction (**Figure 2**). These have been applied to a broad class of reactions, and as we shall discuss in this chapter, we too have been able to summarize the results of our computations in a similar fashion, which is presented below.

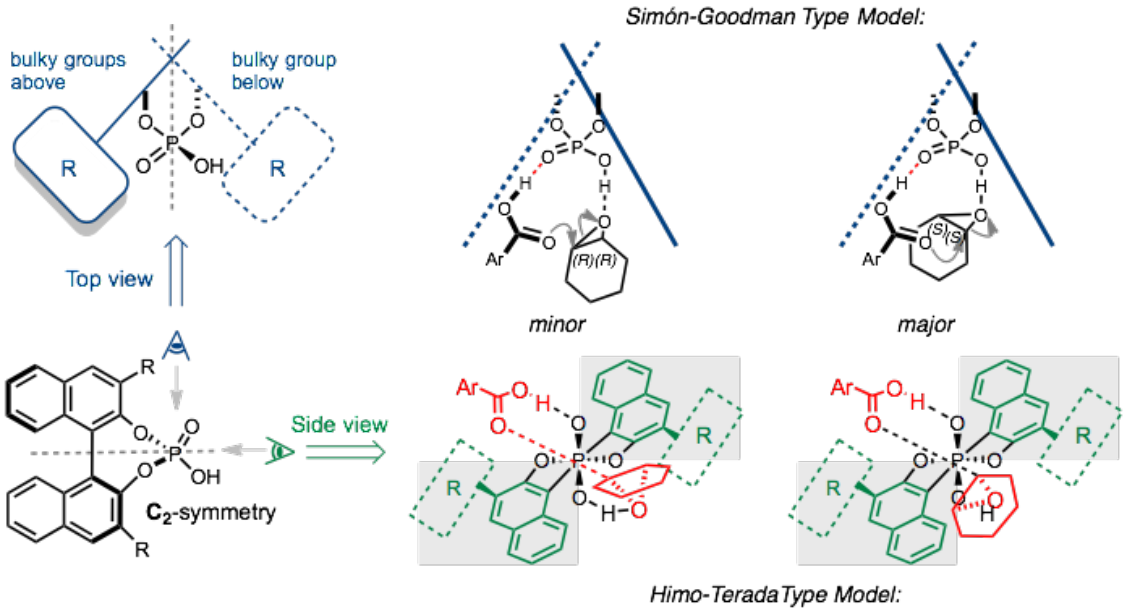

Figure 2. Qualitative models originally developed for imine reduction, applied by us to epoxide desymmetrization following computational investigation.

Our previous calculations with CPAs had highlighted that a pathway involving a single oxygen atom of the catalyst forming two contacts with the substrate was competitive with the bifunctional pathway involving two oxygen atoms. Prior, CPA promoted desymmetrizations have suffered from reproducibility issues as salt contamination caused the C.P.A act as a chiral ligand instead of an acid catalyst.[7] In our current study we have focused on work performed by groups who had investigated the possibility that metal leaching had resulted in a competing mechanism.[8] If the C.P.A is acting as a general acid and not coordinating a salt we theorize that the mechanism will follow the traditional bifunctional activation mode as suggested by **Figure 1**.

4.1.3 Computational Methods

Most methodological details for the calculations in this chapter have already been discussed in chapter 2, so we do not repeat those details. We have used a QM/MM approach to study the phosphoric acids as has been shown to lead to successful agreement between computation and experiment for several CPA-catalyzed transformations in the literature.[9] Specifically, we adopt the ONIOM implementation in Gaussian, using the M062x density functional as the high level of theory, with the universal force field (UFF) as the lower level, described by M062x/6-31G(d,p):UFF. Optimizations were performed at this level. Single point energy calculations were performed using M062x and a triple-zeta valence polarized basis set (TZVP) with a toluene solvent correction (CPCM). While we have studied TRIP catalysts, for which the structures are well known both computationally and from X-ray crystal structures we have also studied newer variants of the CPA catalysts for which experimental structures were not available. Since comparison with solid-state structures is impossible, we believe that the accuracy of our method will be reflected in the predictions of selectivity from the models. Our earlier benchmarking studies for CPA models did not include thiol-based compounds, which we study in this chapter. A benchmarking study has been performed (section 3.3.1) and the results are discussed accordingly.

4.2 CPA-mediated meso-epoxide desymmetrization with benzoic acid

4.2.1 TRIP promoted mechanism and selectivity

List *et al.* have reported the stereoselective opening of cyclohexene-oxide by benzoic acid: using the (*R*)-atropisomer of the TRIP catalyst results in a 75% ee in favor of the (*S,S*) enantiomer. Since the epoxide ring-opening is a stereospecific transformation the two possible products are the (*R,R*) and (*S,S*)-enantiomers. No diastereomers are seen experimentally, consistent with opening of the epoxide with inversion. In this chapter, we refer to (*R*) and (*S*) selectivity to discuss the formation of the (*R,R*) and (*S,S*) products.

We computed the competing GS and TS structures for the ring-opening. From our calculations S-selectivity is observed for the TS (although not GS), which is consistent with the sense of selectivity observed in experiment. If ones assumes that Curtin-Hammett type interconversion can occur between the two GS complexes, then the resulting enantioselectivity is computed as an er of 75:25, which compares well with the experimental value of 79:21 (**Figure 3**).

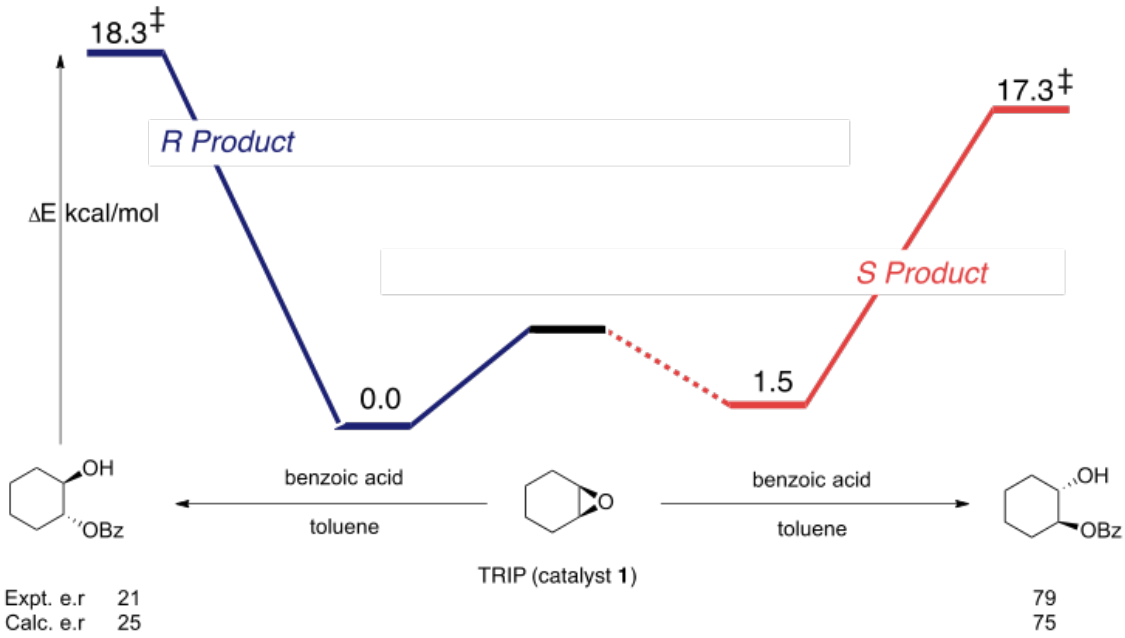

Figure 3. M062x/TZVP//M062x/6-31G(d,p):UFF energy profile for the TRIP-promoted desymmetrization of a meso-epoxide by benzoic acid.

From our computed reaction profile it is evident that major product is derived from the least stable reactant complex, implying a rapid equilibrium prior to the epoxide opening step. This also illustrates specific transition state recognition occurring along the S-enantiomeric pathway which preferentially stabilizes this over the competing R-pathway. In contrast to our previous calculations the difference in the ground state energies only represent a 8% contribution to the activation barrier while it represented a 40% contribution to the activation barrier of the spiroketalization.

Analysis of the ground state-structures (i.e. reactant complexes) in the pro-R and pro-S case highlights the different initial approach angles, 70° and 93°, respectively. In the pro-R case the nucleophilic oxygen atoms is 0.16 Å further away from the reaction center, the electrophilic carbon carom. In the diastereomeric TS structures (**Figure 4**)

the approach trajectory for both enantiomeric products is identical, 103°. This suggests that the enantioselectivity arises not from steric effects which alter the nucleophilic trajectory, but rather non-covalent interactions which preferentially stabilize the S-TS structure. For comparison, the ideal approach trajectory we computed using a water promoted reaction showed a trajectory in the TS of 100°.

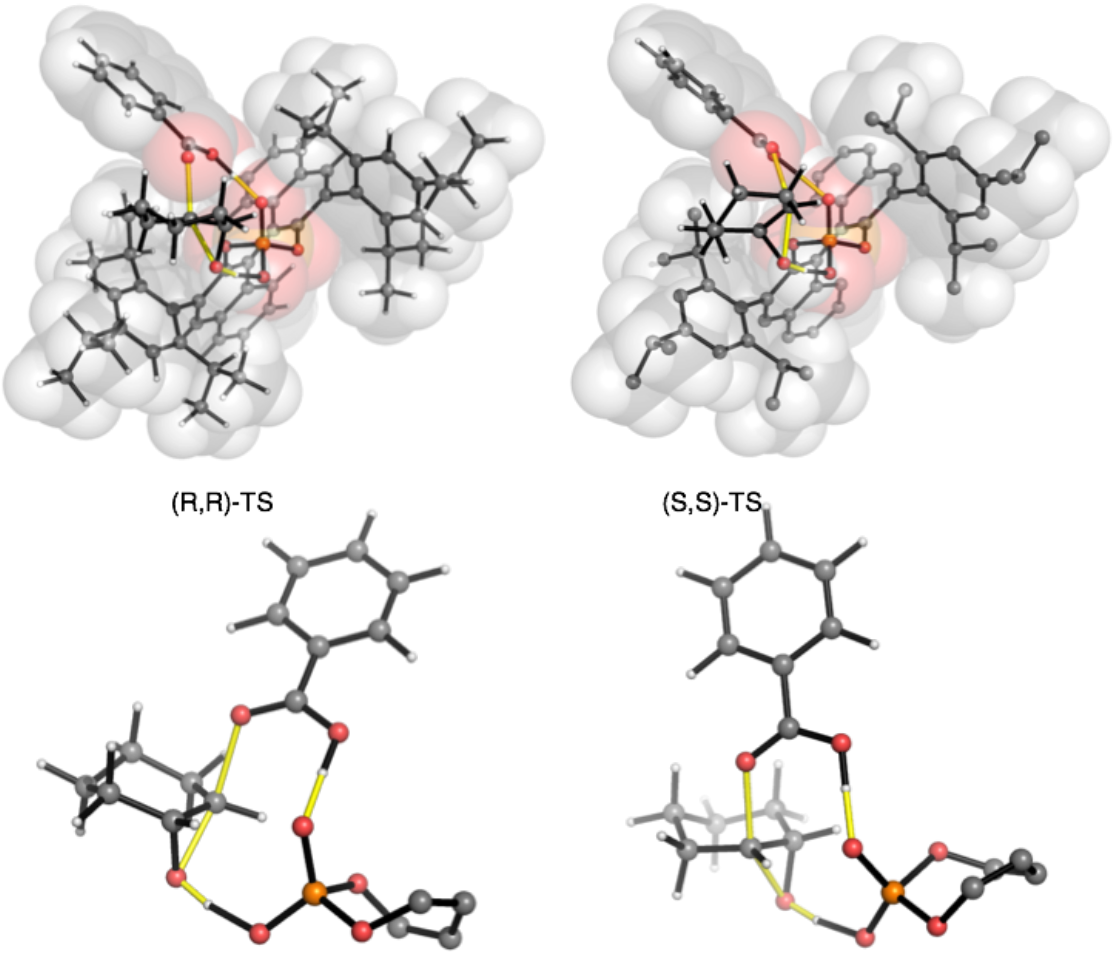

Figure 4. M062x/6-31G(d,p):UFF optimized TS structures leading to enantiomeric products Top: Full TS structures, Bottom: geometries with the CPA backbone/substituents removed for clarity.

The initial 23° differences for the pro-R complex and the subsequent unfavorable interactions with BINOL catalysts force the pro-R complex to adopt a conformation that does not display a productive NAC.[10] The initially less-productive binding event would help explain the difference in observed selectivity but without probing the shifts in the ground state and transition state position this conclusion would be speculative. A

way for the catalyst to control a reaction outcome where there is a stereoelectronically well-defined pathway, as in this case, is to perturb the reagents' approach away from ideality.[7] Essentially, this could be achieved either through electronic perturbation of the reactants to alter the stereoelectronic trajectories, or through increased steric interactions between catalyst and substrate, forcing a change in approach.

4.2.2 Modified CPA-mediated kinetic desymmetrization

Presented in List's initial paper was the first utilization of a novel 3,3'-substituted BINOL ring (**Figure 5**, catalyst **2**). The increased steric bulk over the TRIP catalyst was hypothesized to increase non-specific interactions with the substrate. Unlike the TRIP catalyst (**Figure 5**, catalyst **1**) that can bind a substrate/TS by an "induced fit" binding mode as the rotatable isopropyl groups can either protrude a methyl or hydrogen towards the chiral pocket, the modified catalyst is assumed to project fixed steric interactions towards the substrate.

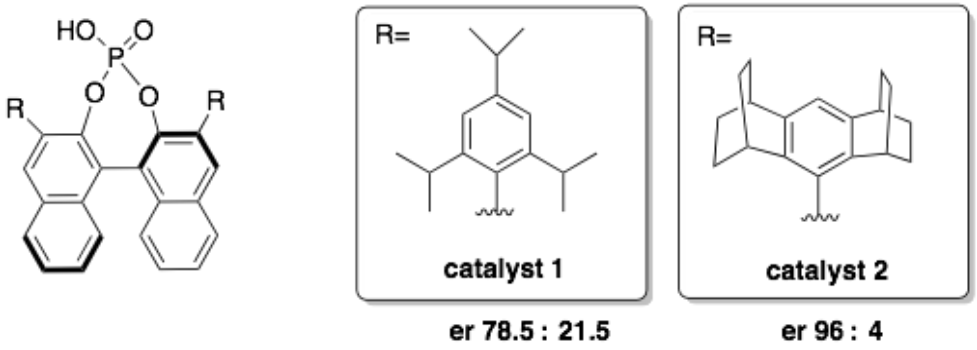

Figure 5. Catalyst structures reported for CPA-catalyzed epoxide desymmetrization.

With this new catalyst, List found that the enantioselectivity (ee) of the reaction increased from 57% to 92% ee as shown in **Figure 5**. From the structure of the modified catalyst **2** we would not expect the structural alterations to affect the overall mechanism of the transformation, or the stability of the dimeric resting catalyst species. The modified catalyst reduces the size of the chiral pocket created by the 3,3'-substituents: from a visual comparison we could expect that the effect of this alteration is more pronounced in the TS than in GS structures. In fact, the geometric difference is relatively subtle: Figure 5 shows a space-filling CPK representation of the two

catalysts, extracted from the corresponding TS structure (**Figure 6**). It is noticeable that the TRIP catalyst undergoes an opening of the chiral pocket, while this does not occur for catalyst **2**, presumably because of the greater bulk.

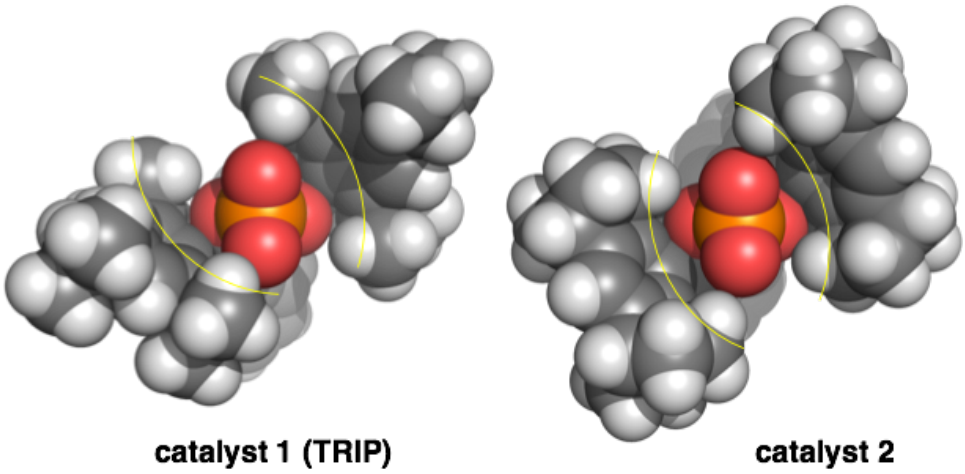

Figure 6. Optimized ONIOM geometric comparison of the two catalyst pockets (the CPA is shown in conjugate base form for clarity).

We obtained the analogous reaction profile with this modified catalyst for the epoxide desymmetrization. Pleasingly, as was seen experimentally, the computed selective rose for catalyst **2**. The sense and level of enantioinduction (97:3) was in superb agreement with the experimental value of (96:4). Although such quantitative agreement can be fortuitous, reproduction of the experimental trend, namely an increase in selectivity, suggests that the calculations describe the reaction well. The resulting energy profile is show in in **Figure 7**. There is little discrimination between the reactant complexes, and 1.9 kcal/mol between the competing TS structures.

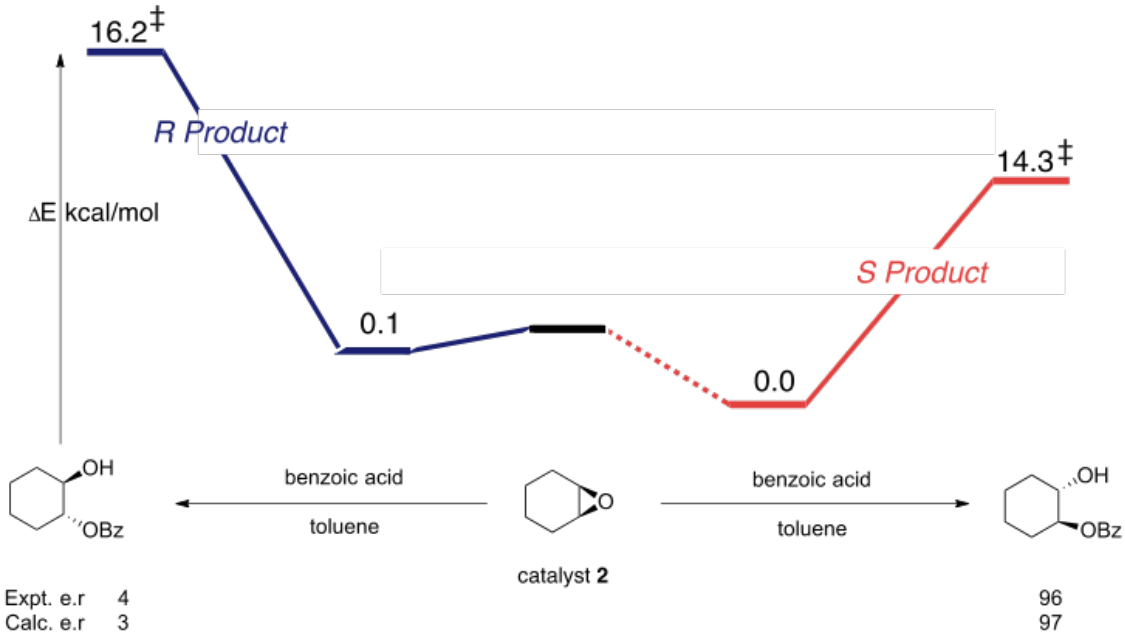

Figure 7. M062x/TZVP//M062x/6-31G(d,p):UFF energy profile for the catalyst **2**-promoted desymmetrization of a meso-epoxide by benzoic acid.

From our reaction profile, **Figure 7**, there are two qualitative differences relative to TRIP. Firstly, there is no discrimination between the reactant complexes, and secondly, the preferential stabilization of the S enantiomeric pathway has increased. This is consistent with the greater levels of enantioselectivity observed experimentally for this catalyst. The effects of the catalyst structure on the TS may be studied from the optimized structures below (**Figure 8**). From the structural analysis the most prominent feature that we are able to decipher is the significant distortion of the benzoic acid as a result of unfavorable contact with the catalysts. When compared to TRIP, with this catalyst in the GS, the S enantiomer's NAC has been decreased by 6° with an increase in the trajectory distance to 2.7 Å while the R-enantiomer's trajectory has nearly stayed the same while the distance from the reaction center has increased by 0.04 Å as a result of the unfavorable interactions.

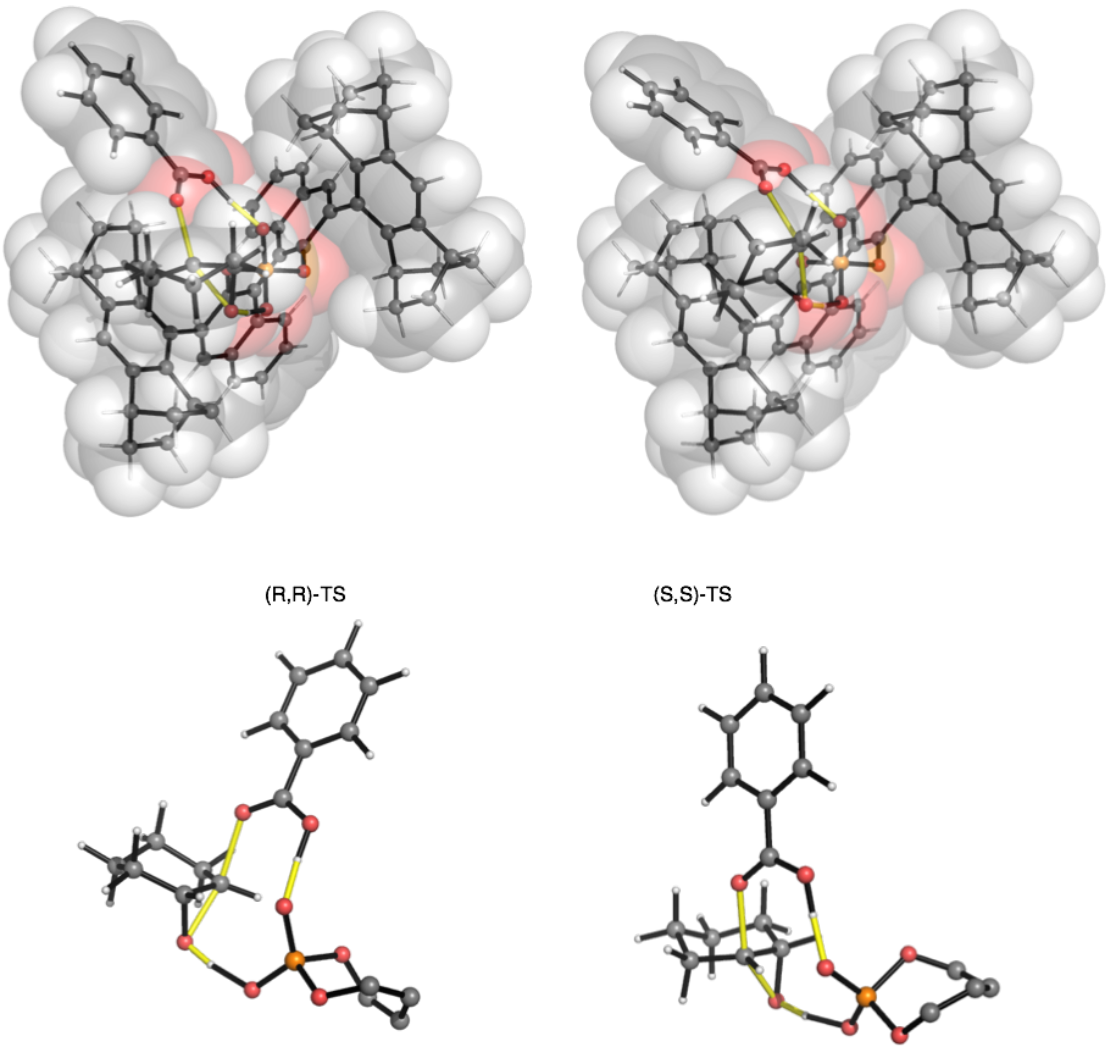

Figure 8: M062x/6-31G(d,p):UFF optimized TS structures with catalyst **2** leading to enantiomeric products Top: Full TS structures, Bottom: geometries with the CPA backbone/substituents removed for clarity.

4.2.3 Brønsted Correlation

A classic physical-organic technique to test the sensitivity of the reaction center to either the nucleophile/leaving group is to utilize a Brønsted plot.[11,12] Such linear free energy relationships (LFERs) correlate shifts in GS thermodynamics with changes in kinetic reactivities. In our case, shifts in the thermodynamic state, the catalyst reservoir, could convolute the outcome. The deviation from the ideal Brønsted acid model, investigated computational, would help highlight kinetic changes not correlated with the rate-determining step. This would provide a way of correlating the ideal shift

(computational) and the experimental outcome to detect possible deviations as a result of shift in the stability of the catalyst-reservoir.

Ultimately, the best way to probe the reaction center would be to alter the electronics of the catalyst as this would provide the most direct information on the effect of the catalyst on the reaction center. Utilizing different phosphoric acid catalyst would be uninformative, however, as the necessary alterations to the catalysts to induce the pKa shift would also result in a new chiral pocket with different steric interactions. A more subtle way to measure this effect, but still informative, is to alter the benzoic acid nucleophile. We explored the same reaction with three different benzoic acids to investigate the correlation between selectivity and the nature of the *para*-substituent (CF_3, H, MeO) (**Figure 9**).

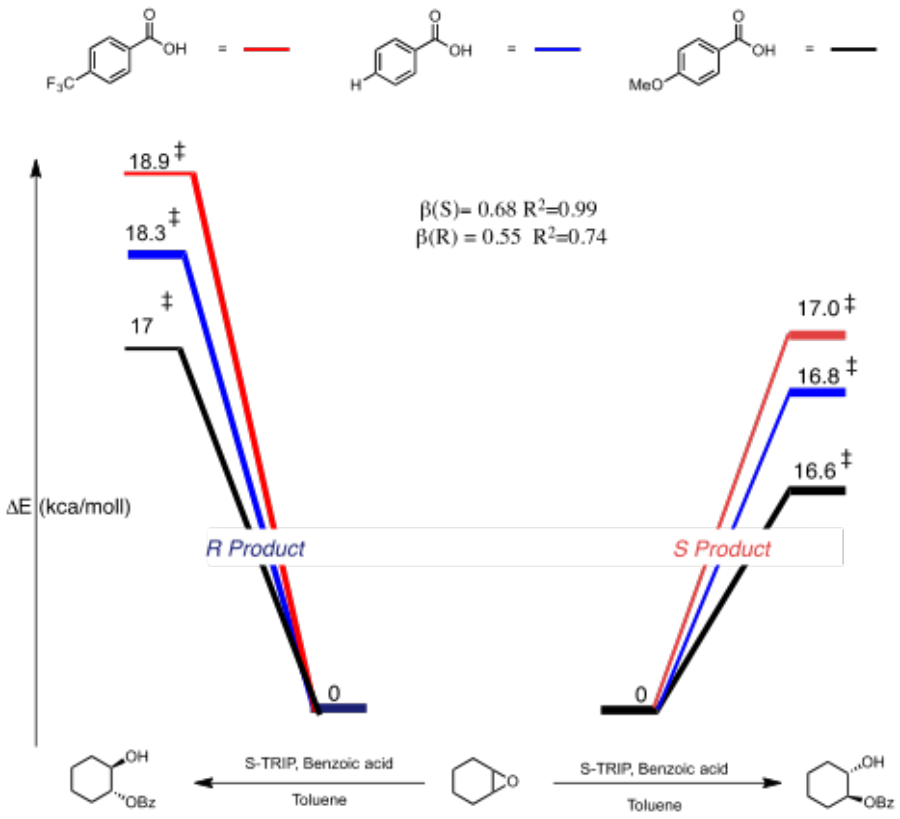

Figure 9: M062x/6-31G(d,p):UFF computed Brønsted analysis of the rate- and selectivity-determining step in the epoxide desymmetrization.

Our computational Brønsted analysis, illustrates the role of electronics in the stereodetermining step: the activation barrier for the major pathway shows lower

sensitivity to the change in nucleophile than the minor pathway. As a result the enantioselectivity is computed to rise with an electron-deficient benzoic acid nucleophile as the minor pathway becomes more unfavorable. In turn this gives us information about differences between the TS structures for the two pathways. One argument consistent with this is that there is an unfavorable increase in sterics along the R-reaction coordinate, which becomes increasingly severe as a less nucleophilic (i.e. more acidic) requires a closer approach to the epoxide.

4.3 Meso-Epoxide desymmetrization with Thiobenzoic acids

The implication of the stability of the benzoic catalyst reservoir can be explored through the alteration of the nucleophile. In a related transformation to that discussed above, List and co-workers disclosed that thiobenzoic acid could desymmetrize the meso-epoxide with 81:19 er, marginally higher than with benzoic acid (**Figure 10**).[13,14] While the sense of selectivity is unsurprisingly the same as with a benzoic acid nucleophile, less information was available about the nature of the catalyst:nucleophile complex and so we investigated the reaction computationally. Additional considerations such as the tautomerization state of the nucleophile add to the complexity of this reaction.

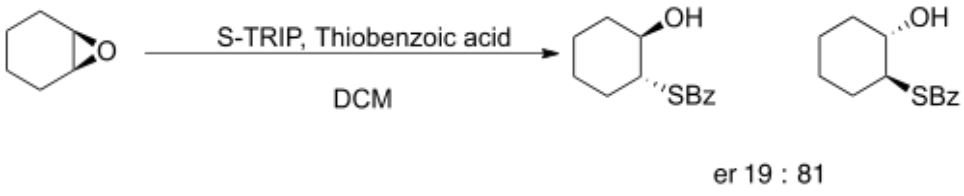

Figure 10: Experimental outcome when using thiobenzoic acid as the nucleophile in CPA-promoted epoxide desymmetrization.

Thiobenzoic acid is only marginally more acidic than benzoic acid (by around 0.6 pKa units), although sulfur nucleophiles are generally superior than oxygen for nucleophilic substitution. In the light of our computed Brønsted information we might anticipate a slight reduction in enantioselectivity, which we observed with the more electron rich –

MeO substituted benzoic acid. To understand the structural differences of TS structures with a thiobenzoic nucleophile in relation to those established already, we decided to investigate the desymmetrization of cyclohexene oxide with thiobenzoic acid.

4.3.1 TRIP promoted desymmetrization

List *et al.* published the desymmetrization of the meso-epoxide by thio-benzoate using several different organocatalysts, but the two we have focused on is S-TRIP (**1**) and R-**2** (Figure 3) developed by their group. To first consider the nature of the nucleophilic species, we investigated the tautomerism of thiobenzoic acid. In the free monomeric form of thiobenzoic acid we found a modest thermodynamic preference for the S-H (carbonyl) tautomeric form over the alternative O-H (thiocarbonyl) form by 0.9 kcal/mol. We also studied the homodimeric form of thiobenzoic acid to explore how this tautomeric preference is affected by hydrogen-bonding. A preference now emerges for the thione O-H tautomer over the S-H form by 3.8 kcal/mol. The thiocarbonyl form is more acidic (by definition, as the less stable tautomer this is by 0.9 kcal/mol), and forms stronger hydrogen bonding interactions. This implies that while in the free form, the S-H form may be marginally favored, in the context of hydrogen-bonded assemblies the O-H form is preferred completely. This of course has consequences for the CPA-catalyzed desymmetrization, where the catalyst engages in dual hydrogen-bonding interactions.

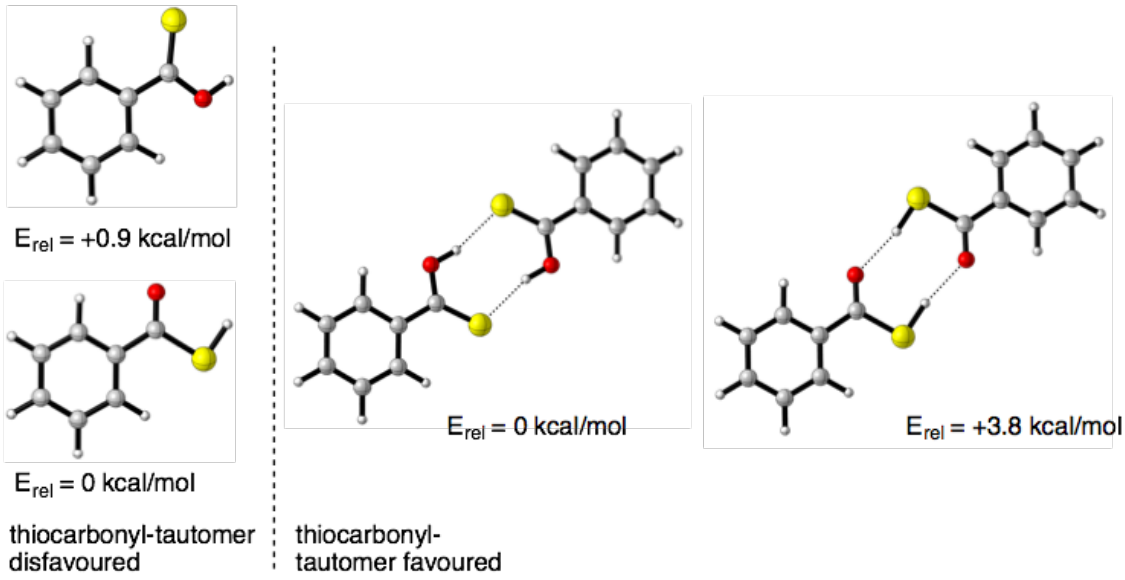

Figure 11. Tautomerism of thiobenzoic acid computed at the M062x/6-31G(d,p) level of theory.

The computational methodology that we had used previously had only previously considered the presence of C, H, O and N atoms while the introduction of an S atom may result in erroneous results utilizing the current methodology. To test other methods we explored the computed enantioselectivity-using previously established functional and basis sets by other groups.[15,16] Due to the system size we still were reliant upon the ONIOM approach for geometry optimizations, however, we considered a variety of Minnesota functionals in reproducing the experimental selectivity.

Functional	Basis Set	Computed er (S:R)
M062x:UFF (ONIOM)	6-31G(d,p)	98:2
M062x	TZVP	92:8
M06-HF	TZVP	99:1
M062x	6-31++G(2d,2p)	98:2
M06-HF	6-31++G(2d,2p)	98:2

Table 1: Functional and Basis Set screening in the calculation of enantioselectivity with a thiobenzoic acid nucleophile.

There is relatively little variation in the quantitative outcome of computations performed at different levels of theory and with different sizes of basis set, and all levels give the same absolute sense of enantioselectivity. All overestimate the experimental values, while M062x/TZVP single point calculations utilizing ONIOM geometries appeared to estimate the reaction outcome with greatest quantitative accuracy. From our calculations, the computed enantioselectivity was 92:8 in favor of the S enantiomer (c.f. 81:19 experimentally). (**Figure 12**).

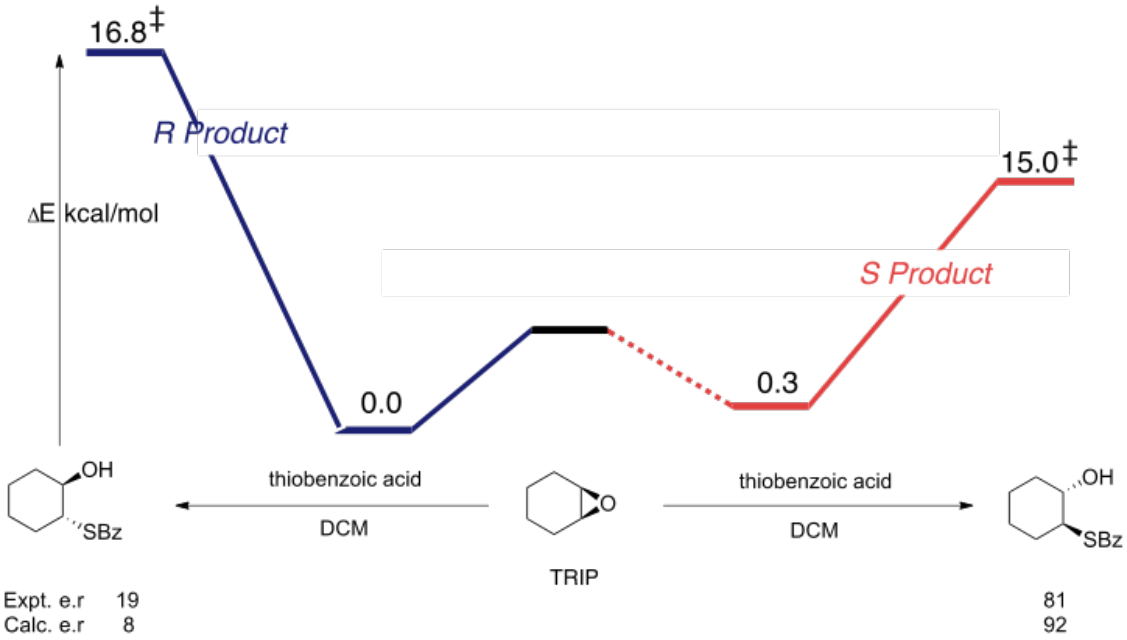

Figure 12. M062x/TZVP//M062x/6-31G(d,p):UFF energy profile for the TRIP-promoted desymmetrization of a meso-epoxide by thiobenzoic acid.

From our reaction profile we find that the catalyst displays a rapid equilibrium resulting in the major product being derived from the slightly less stable reactant complex, the S-enantiomer. Our results predict that the enantioselectivity will be 21% higher then that

observed experimentally. It is worth noting that the conditions that this reaction was performed under were non-optimized: List and co-workers had found that by running the reaction under-cryogenic conditions the enantioselectivity could increase by 12%. Based on these observations and results we believe that our model accurately reflect the behavior of the catalyst in the reaction and we can utilize the structures generated to derive the behavioral differences found in this catalyst.

Based on previous Brønsted-analysis (Figure **9**) it was unexpected that the more nucleophilic thione is able to display such greater enantioselectivity then the benzoic acid. To glean some useful information on the mechanism we investigated the structures of both ground state and transition state to determine if destabilization of the ground state was still controlling the enantioselectivity of the reaction. The R and S trajectory display similar approach trajectories; starting 4 Å away with very poor overlap with the epoxide orbital, 56º and 59º respectively. In the transition state the S enantiomer is 0.09 Å further way but it displays a similar favorable trajectory as the R-enantiomer. The critical difference between these two conformations can be seen in the structures. In the S enantiomer case we find that the substrate is making T-stacking with the catalyst while the R-enantiomer is projected out into space (**Figure 13**).[17]

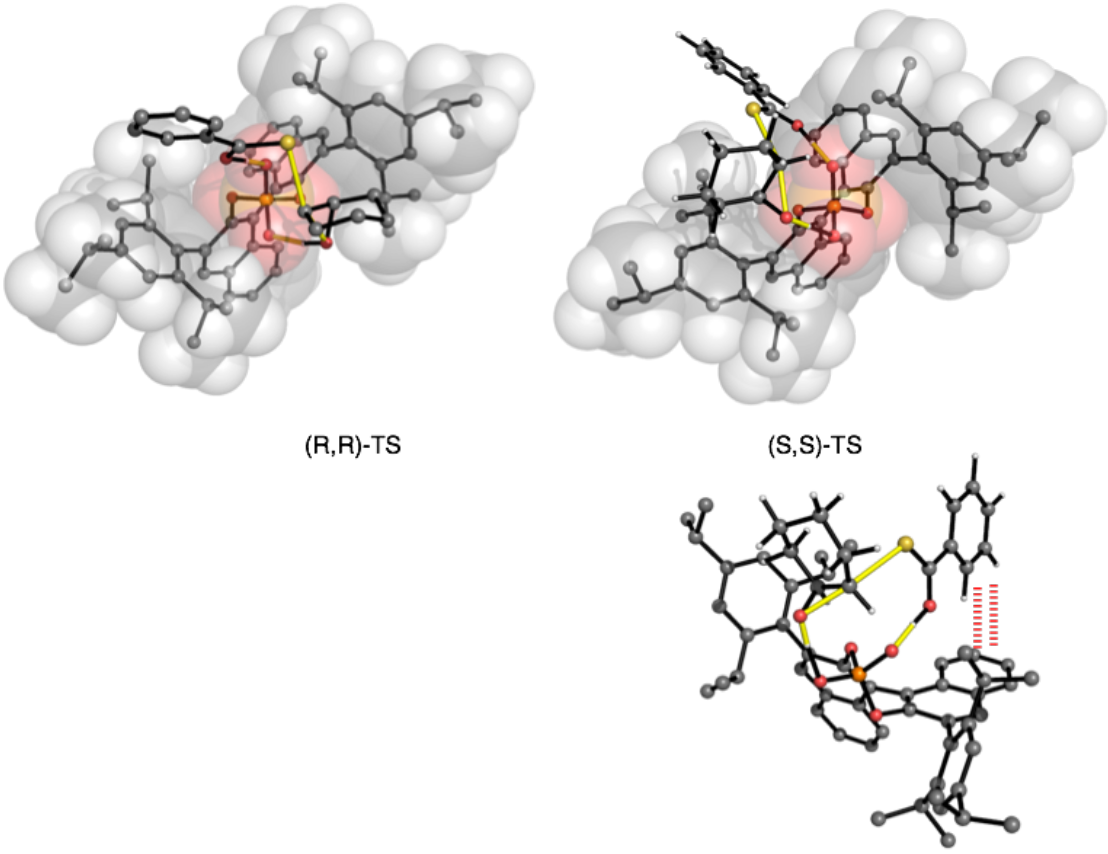

Figure 13: M062x/6-31G(d,p):UFF optimized TS structures with TRIP and a thiobenzoic acid nucleophile leading to enantiomeric products.

The deviation from the trend that we would expect from the benzoic acid case is directly contributed to the T-stacking only seen for the S-enantiomer pathway. In the Benzoic acid case, the S-enantiomer is too far away, 7 Å, from the BINOL-backbone to make any productive nonbonding contacts. In the thione case though we could expect that the longer C-S bond as well as the larger 3p orbitals could increase the redundancy for the approach trajectory allowing for the deviation shown by the thiobenzoic acid which could make strong contacts with the BINOL 3.5 Å away.

The discrimination between R and S enantiomers is largely enthalpic in origin, rather than due to entropic effects. This would be consistent with an increase in selectivity at lower temperatures. Under the cryogenic conditions we could expect the catalytic population of the S-enantiomer to increase leading to an improvement in the enantioselectivity, as this reaction is not under-rapid equilibrium control.

To optimize the enantioselectivity List and Co-workers used their CPA catalysts in which the BINOL has been partially-hydrogenated. This is proposed to lead to an increase in the torsion angle between the two phenyl rings, potentially opening the chiral cavity around the phosphoric acid. Additionally, we anticipated that this would also destroy the potential for a T-shaped stacking interaction that we had computed previously (**Figure 14**).

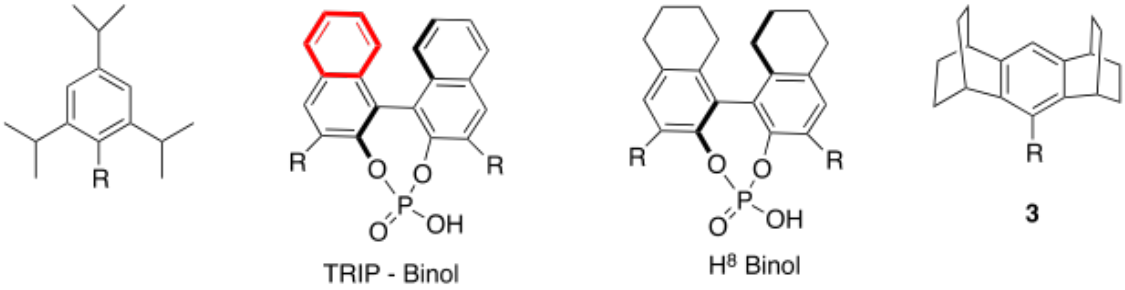

Figure 14. T-Stacking region highlighted in red for TRIP and the H^8 BINOL has these interactions removed.

4.3.2 H_8-TRIP promoted desymmetrization

As we have seen thus far, the increased nucleophilicity decreases the demand on the reactant to be positioned in such a conformation that there is a proper trajectory overlap. Previously, we had seen that the T-Shape stacking had contributed to the discrimination between the two competing transition states but with this novel catalyst this C-H–π interaction would presumably be destroyed. The increased steric interaction could result in further discrimination between the transition states, but we would expect that without significant steric interactions this effect would be mitigated as the nucleophile is further away from the reaction center and the thiobenzoic acid is less sensitive to trajectory modulation.

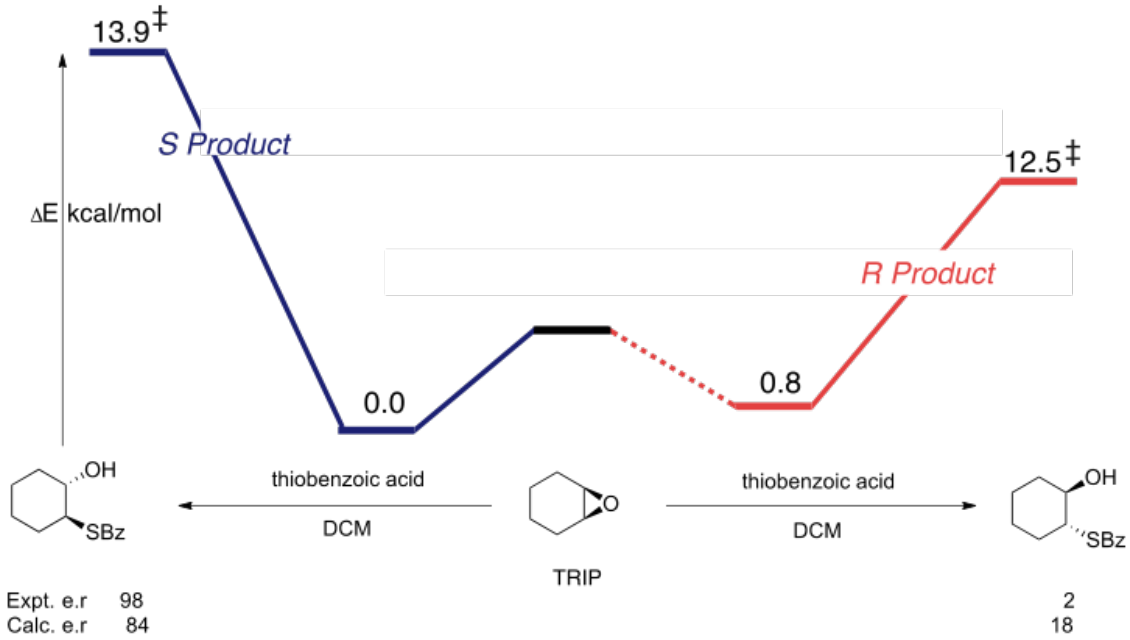

Figure 13: M062x/TZVP//M062x/6-31G(d,p):UFF energy for the H^8-BINOL CPA catalyst promoted meso-epoxide desymmetrization by thiobenzoic acid.

Based on our prior structural analysis for the fully aromatic backbone, it should come as no surprise that the enantioselectivity is eroded with the removal of the aromatic ring. From structural analysis of the optimized catalyst structures, we find that dihedral angle between the two phenyl rings of the catalyst's backbone increased to 56° which would result in a more open pocket. This compares with a value of 51° for the fully-aromatized backbone CPA. In the transition state the trajectory for the S-enantiomer has become more favorable, 101°, while the bond distances have not changed drastically (Figure **14**). This should result in a increase in the overlap in the orbital lowering the intrinsic barrier for the reaction. We would expect that such an outcome would result in the a lowering of the activation barrier for the S-enantiomer pathway and subsequently, lower the enantioselectivity of the reaction. Based on our results it is difficult to determine the origin of the enatioselectivity increase with the introduction of the novel norbornane-functionalized catalysts.

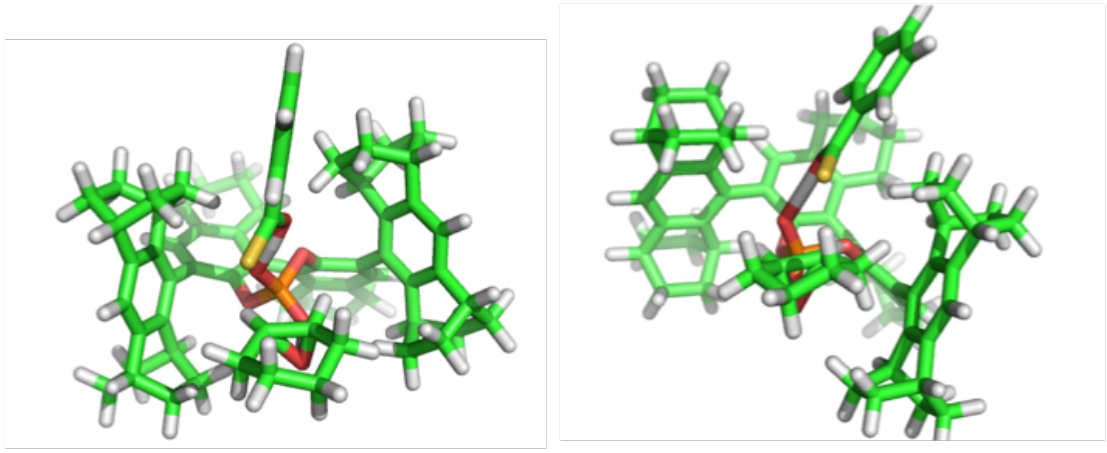

Figure 14. M062x/6-31G(d,p):UFF optimized TS structures with H_8-TRIP and a thiobenzoic acid nucleophile leading to enantiomeric products.

4.4 Aziridine Desymmetrization

4.4.1 Aziridine Desymmetrization

CPA catalysis has also been used in the desymmetrization with meso-aziridines. Interestingly, the relative loading of the nucleophile (benzoic acid) has an effect upon the observed enantioselectivity. The nature of the nitrogen protecting group (benzoyl derivatives were examined) is also critical: catalyst degradation becomes a competing pathway, presumably through complete proton transfer and addition of the phosphate to the aziridinium for the more basic derivatives (**Figure 15**).[18]

Derivative	Conversion
R_1= H , R_2= H	0% (TRIP Degration)
R_1= NO_2 , R_2= H	23%
R_1, R_2 = NO_2	98%

Benzoic acid Loading	Enatioselectivity
1.8x	89% ee
3x	92% ee
5x	94% ee
10x	>99% ee

Figure 15: Impact of electronics of the protecting group acid and loading of the nucleophile upon the reaction outcome in CPA-promoted aziridine desymmetrizations.

This abrupt shift in the product distribution could come about if the mechanism of the reaction changed. The results for the epoxide supported an ordered mechanism where the benzoic acid first binds to the catalyst, to create a bifunctional species which is capable of both nucleophilic attack and protonation of the epoxide. As the epoxide's capacity to act as a hydrogen bond acceptor is limited, as compared to the benzoic acid, we would be more inclined to believe that the active phosphate catalyst ground state is the phosphoric acid:benzoic acid dimer. With the increased hydrogen bond-accepting capacity of the aziridine, it is tempting to speculate that the mechanism may not proceed via this same sequence as earlier. An alternative resting state becomes the phosphate catalyst:substrate dimer. As the complexity of the mechanism may be changing based on the substrates' physical properties, we needed to investigate how the selectivity would change when the order of the reagent binding changes. To mimic this effect we investigated both the unsubstituted benzamide, where the phosphate addition was a significant side reaction and the 2,4-dinitrobenzamide where phosphate addition was avoided.

Sun and co-workers investigated the initial binding event by characterizing the intermediates that had arisen through phosphorus NMR.[19] Based on the comparison of phosphorus chemical shifts obtained for control species; catalyst alone, catalyst:aziridine, and catalyst:nucleophile, the NMR analysis of the reaction mixture of all three components did not show any peaks which were readily indentifiable. This

could highlight that the catalyst reservoir has shifted away from the catalyst:nucleophile complex which operates in epoxide desymmetrizations. It is possible that the activation mode of the catalyst is via coordination to the subtrate nitrogen atom, or alternatively to the carbonyl oxygen atom. It has been argued that a rapid equilibrium arises between both coordination modes, and that the preferred reaction pathway is via coordination to nitrogen (**Figure 16**).

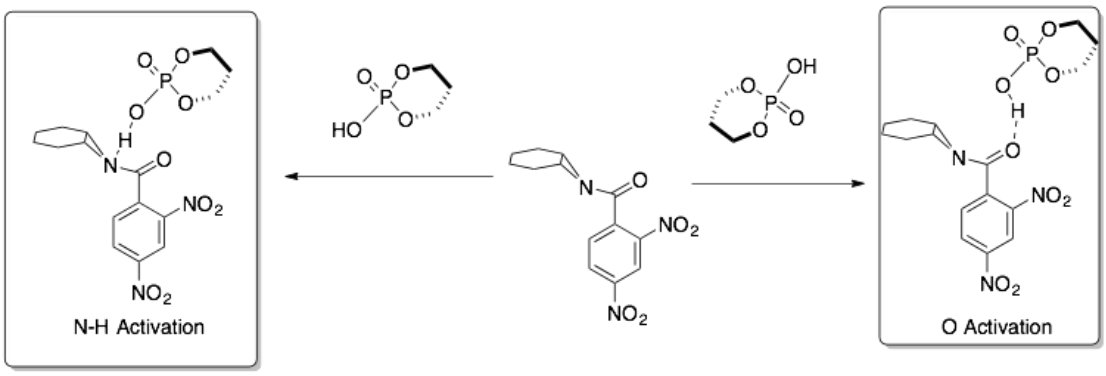

Figure 16: The two discrete protonation/hydrogen-bond activation modes that could be involved in the phosphate promoted desymmetrization of aziridines.

We began our investigation into what we term the N--H activation mechanism, which involves catalyst coordination to the aziridine nitrogen atom, while the P=O bond activates the acid nucleophile to attack. From our calculations the difference in the TS energies between the two enantiomeric pathways is 1.8 kcal/mol. However, for this activation mode, the computed stereochemical preference is in the opposite sense with respect to the experiments. From our initial results the reaction course was expected to give the opposite enantiomer with 98:2 e.r (**Figure 17**). As far as possible we confirmed that the original stereochemical assignment of the product was correct.

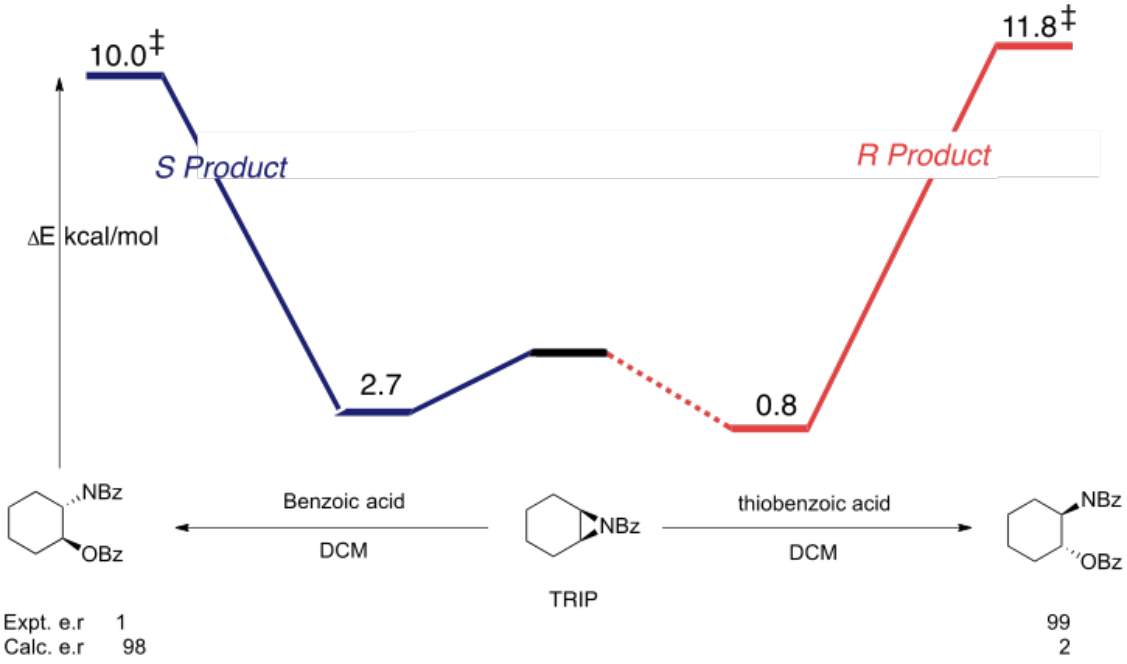

Figure 17. M062x/TZVP//M062x/6-31G(d,p):UFF energy for the TRIP-promoted aziridine desymmetrization via a modelled N-H activation mode.

For N---H activation we find that both R and S reaction pathways display transition states with a trajectory of 97°. The structure of the transition state points to T-Stacking as the critical interaction between the R and S trajectories and the catalyst. When we compare the distances in the structures we find that the S transition state is 0.7 Å closer to the BINOL backbone resulting in the favorable interactions that help promote the S-enantioselectivity. It is striking to note that the epoxide and aziridine desymmetrization reactions proceed to give opposite enantioselectivities with the same catalyst enantiomer and nucleophile (**Figure 18**). This clearly sugested to us that an alternative TS model would be required to explain the reversal of selectivity seen in experiment.

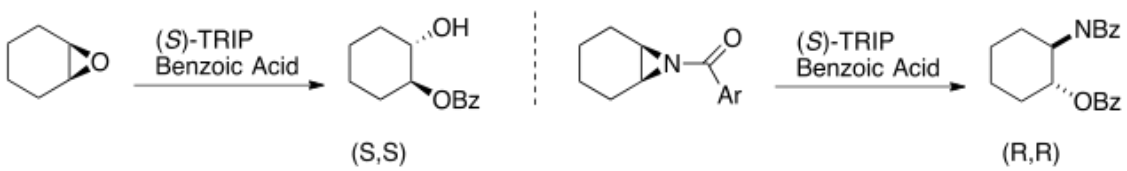

Figure 18. Comparison of the experimentally determined enantioselectivities in epoxide and aziridinium CPA-promoted desymmetrizations (major enantiomer of the product shown in each case).

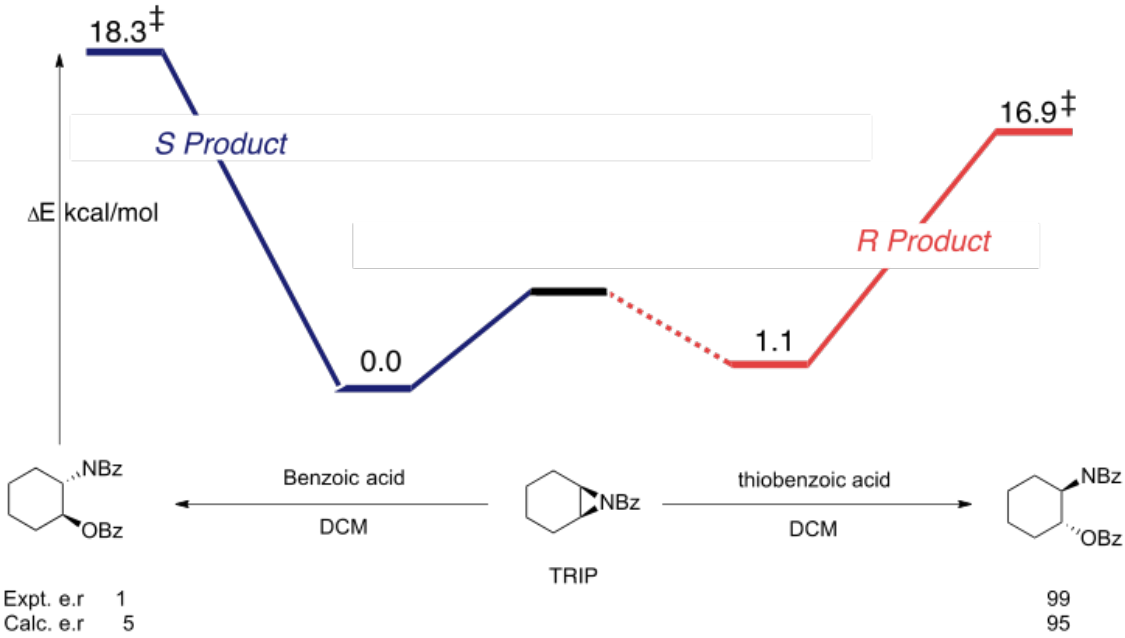

Figure 19: M062x/TZVP//M062x/6-31G(d,p):UFF energy for the TRIP-promoted aziridine desymmetrization via a modelled O-H activation mode.

For the carbonyl activation trajectory, which we refer to as "O-activation", **Figure 19** we find that the unlike in previous cases, the approach trajectory for the favored reaction course is 107º, which is more favorable as compared to the to the S enantiomer trajectory at 97º. In both transition states, we again find that T-stacking is a dominant interaction with the substrate. Unlike the N-activation pathway, the trajectories in the carbonyl activation pathway are 1 Å closer to the BINOL catalysts. In the S-enantiomer case though, the aromatic ring of the benzoic acid must sit over the face of the cyclohexane ring resulting in steric interactions with the axial hydrogen (**Figure 20**). As expected, to accommodate the hydrogen bond with the carbonyl group, the susbtrate orientation is very different from the epoxide case. Now, the substrate lies closer to the quadrant occupied by the catalyst substituent, and in the disfavored TS it is pushed closer to this group. We have summarized the conformations qualitatively in the Noyori-style quadrant cartoon in **Figure 20**.

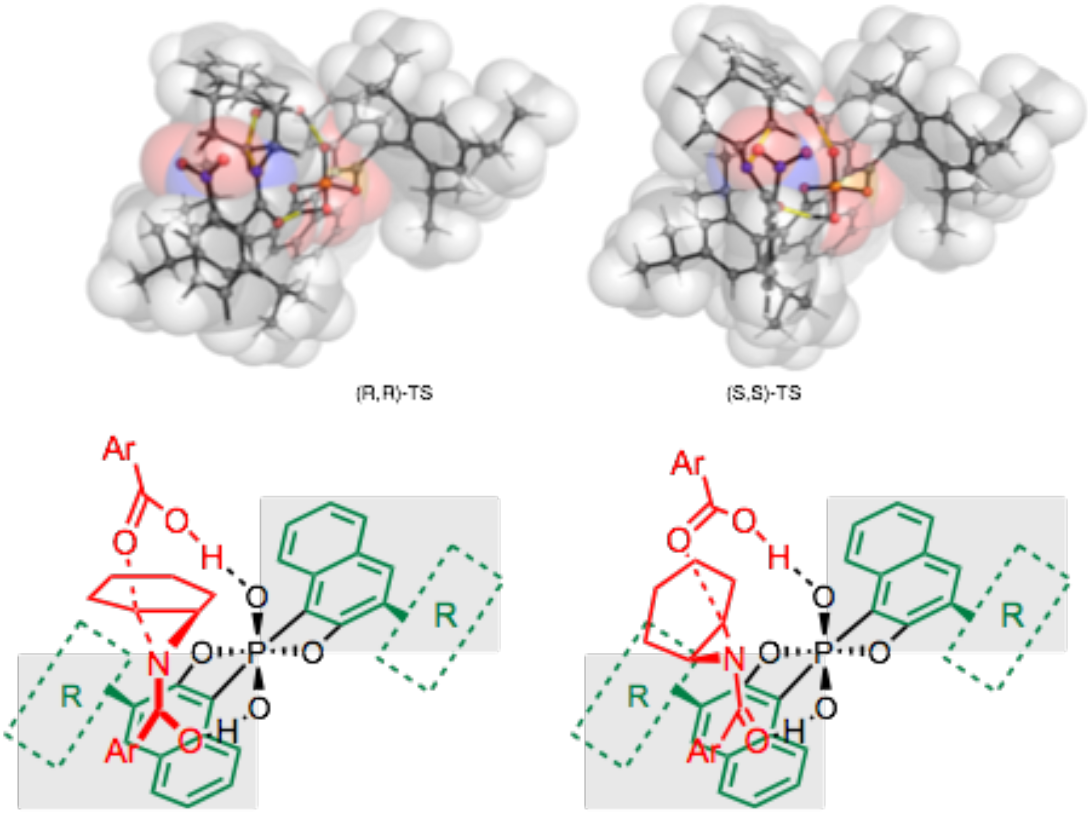

Figure 20: M062x/6-31G(d,p):UFF optimized TS structures for azirine desymmetrization with TRIP and a benzoic acid nucleophile leading to enantiomeric products, via the O---H activation mode.

From the structural analysis it would appear that the chiral acids influences the reaction trajectory through beneficial T-stacking. Unlike the R-enantiomer trajectory, the S-enantiomer trajectory requires the benzoic acid to sit over the face of the ring. If this were the origin of the control, we would expect to find that comparing the reactants alone would result the R-enantiomer being more stable, which would account for the origin of the enantioselectivity.

4.5 Conclusions

We have used QM/MM calculations to uncover the mode of catalysis and origins of stereoselectivity in desymmetrizations mediated by chiral phosphoric acids. In the case

of epoxides reacting with benzoic acids, the electrophilic and nucleophilic reactants are simultaneously activated by the catalyst in a well-ordered transition state which enables discrimination between the enantiomeric products. In the case of a thiobenzoic acid nucleophile, the thione tautomer is found to be less stable as a monomer, but preferentially formed once hydrogen bonding interactions are important. In the nucleophilic reaction, attach by sulfur is mediated by hydrogen-bond activation by the catalyst and stereoselectivity is consistent with that observed for benzoic acids. For the case of aziridine electrophiles, two alternative activation modes were considered and the O-H activation successfully accounted for the observed sense of enantioselectivity. The resulting selectivities in each case could be rationalized in terms of a qualitative model which should be useful to predict the outcome of future asymmetric reactions of related catalysts and substrates.

4.6 References

1. Verzijl, G.K.M.; Vries, A.; Vries, J.; Kapitan, P.; Dax, T.; Helms, M. Nazir, Z.; Skranc, W.; Imboden, C.; Stichler, J.; Ward, R.; Abele, S.; Lefort, L. *Org. Process Res. Dev.* **2013**, 17, 1531.
2. Sun, Y.; LeBlond, C.; Wang, J.; Blackmond, D.G.; Laquidara, J.; Sowa, J.R. *J. Am. Chem. Soc.,* **1995**, 117, 12647
3. Desimoni, G.; Faita, G.; Jorgensen, K.A. *Chem. Rev.*, **2006**, 106, 3561-3651.
4. Monaco, M.R.; Prevost, S.; List, B. *Angew. Chem. Int. Ed*. **2014**, 53, 8142
5. Monaco, M.R.; Poladura, B.; Bernardos, M.; Leutzsch, M.; Goddard, R.; List, B. *Angew. Chem. Int. Ed.* **2014**, 53, 7063
6. (a) Marcelli, T.; Hammer, P.; Himo, F. *Chem. Eur. J.* **2008**, 14, 8562; (b) Simón, L.; Goodman, J.M.; *J. Org. Chem.* **2011**, 76, 1775; (c) Parmar, D.; Sugiono, E.; Raja, S.; Rueping, M. *Chem. Rev.* **2014**, 114, 9047.
7. (a) Larson, S.; Baso, J.; Li, G.; Antilla, J. *Org. Lett.* **2009**, 11, 5186; (b) Ingle, G.; Mormino, M.G.; Antilla, J.C. *Org. Lett.* **2014**, 16, 5548; (c) Larson, S. PhD. Dissertation, University of Southern Florida, 2012.
8. Klussmann, M.; Ratjen, L.; Hoffmann, S.; Wakchaure, V.; Goddard, R.; List, B. *SYNLETT,* **2010**, 14, 2189.
9. (a) Kanomata, K.; Toda, Y.; Shibata, Y.; Yamanaka, M.; Tsuzuki, S.; Gridnev, I. D.; Terada, M. *Chem. Sci.* **2014**, 5, 3515; (b) Jindal, G.; Sunoj, R. *Angew. Chem. Int. Ed.* **2014**, 53, 4432; (c) Li, N. Chen, X; Luo, S.; Fan, W.; Gong, L. *J. Am. Chem. Soc.* **2009**, 131, 1530.
10. Jencks, W.P. Catalysis in Chemistry and Enzymology. Dover Publications. New York (1986)
11. Anslyn, E.V.; Dougherty, D.A. Modern Physical Organic Chemistry. University Science Books, New York (2006)
12. Williams, A. Free Energy Relationships in organic and bio-organic chemistry. The Royal Society of Chemistry, London (2006).
13. Monaco, M. R.; Pré vost, S.; List, B. *J. Am. Chem. Soc* . **2014** , 136 , 16982
14. Wang, Z.; Law, W.K.; Sun, J. *Org. Lett.*, **2013**, 5, 5964
15. (a) Mintz, B.J.; Parks, J.M. *J. Phys. Chem. A,* **2012**, 1086; (b) Weigend, F.; Ahlrichs, R. *Phys. Chem. Chem. Phys.*, **2005**, 3297; (c) Petersson, G. A. Petersson; Al-Laham, M. A. *J. Chem. Phys.*, **1991**, 6081.

16. Zhao, Y.; Truhalr, D.G. *Theor. Chem. Acc*. **2008**, 120, 215.
17. Bissantz, C.; Kuhn, B.; Stahl, M. *J. Med. Chem*. **2010**, 53, 5061
18. Monaco, M.R.; Poladura, B.; Bernardos, M.D.; Leutzsh, M.; Goddard, R.; List, B. *Angew. Chem. Int. Ed.* **2014**, 53, 7063
19. Wang, Z.; Sheong, F.; Sung, H.; Williams, I.; Lin, Z.; Sun, J. *J. Am. Chem. Soc*., **2015**, 137, 5895
20. Simon, L. ; Goodman, J.M. *J. Am. Chem. Soc*., **2008**, 4070.

Appendix

Chapter 1:

1.1.4

Water position Screen (Figure 9)

Scheme #	Name	Enthalpy (Hartrees)	Z.P.E (Hartrees)	Frequency (cm^{-1})
1A	6 TS	-730.7515131	0.300017	-590.03
2A	6 TS	-730.7496983	0.297419	-591.55
3A	6 TS (Twist)	-730.7515131	0.300017	-552.99
4A	6 TS (Twist)	-807.1469969	0.323992	-552.94
1B	5 TS	-730.7446296	0.299459	-523.52
2B	5 TS	-730.7459184	0.297516	-506.86
3B	5 TS	-730.7351746	0.297306	-531.78
4B	5 TS	-807.1425804	0.321024	-486.28

Solvent Isotope Effect

Name	Z.P.E
6TS –water bridge heavy	0.250386
6TS –water bridge	0.299516
6TS –no water bridge heavy	0.249175
6TS –no water bridge	0.296578

Section 1.2.1

4,5 trans Neutral

Name	Enthalpy (Hartrees)	Z.P.E (Hartrees)	Frequency (cm^{-1})
6-*endo*-TS	-538.8692736	0.229546	-612.22
6-*endo*-Prod	-538.96414	0.232885	-
5-*exo*-TS	-538.8690209	0.229128	-549.22
5-*exo*-prod	-538.9583049	0.231851	-

4,5 trans Acid

Name	Enthalpy (Hartrees)	Z.P.E (Hartrees)	Frequency (cm^{-1})
6-*endo*-TS	-386.514307	0.19011	-457.60
6-*endo*-Prod	-386.5575253	0.194482	-
5-*exo*-TS	-386.5151971	0.190482	-437.90
5-*exo*-prod	-386.5479326	0.193607	-

4,5 trans Base

Name	Enthalpy (Hartrees)	Z.P.E (Hartrees)	Frequency (cm^{-1})
6-*endo*-TS	-385.5497128	0.162636	-649.94
6-*endo*-Prod	-385.6173854	0.165686	-
5-*exo*-TS	-385.5520371	0.162523	-619.17
5-*exo*-prod	-385.6069262	0.165165	-

Section 1.2.2

Nicoalou Unsaturated

Name	Enthalpy (Hartrees)	Z.P.E (Hartrees)	Frequency (cm^{-1})
6-*endo*-TS	-424.573472179	0.194906	-300.50
6-*endo*-Prod	-424.610872587	0.198847	-
5-*exo*-TS	-424.567944561	0.195237	-443.33
5-*exo*-prod	-424.606318105	0.198733	-

Nicoalou Ester

Name	Enthalpy (Hartrees)	Z.P.E (Hartrees)	Frequency (cm^{-1})
6-*endo*-TS	-652.364387773	0.239663	-384.44
6-*endo*-Prod	-652.404434491	0.2432	-
5-*exo*-TS	-652.361746196	0.239056	-443.04
5-*exo*-prod	-652.400769781	0.24343	-

Nicoalou Template Ester

Name	Enthalpy (Hartrees)	Z.P.E (Hartrees)	Frequency (cm^{-1})
6-*endo*-TS	-844.24576621	0.300017	-333.03
6-*endo*-Prod	-844.293067778	0.309562	-
5-*exo*-TS	-844.241309339	0.309801	-447.08
5-*exo*-prod	-844.274313021	0.313348	-

1.2.3

Jamison Bronsted

Name	Enthalpy (Hartrees)	Z.P.E (Hartrees)	Frequency (cm^{-1})
6-*endo*-TS	-795.095131163	0.292108	-588.92
6-*endo*-Prod	-794.192550946	0.267351	-
5-*exo*-TS	-795.091373387	0.292201	-608.92
5-*exo*-prod	-794.1817455	0.266783	-

Jamison Bronsted Template

Name	Enthalpy (Hartrees)	Z.P.E (Hartrees)	Frequency (cm^{-1})
6-*endo*-TS	-986.015692832	0.334653	-578.44
6-*endo*-Prod	-986.078141168	0.338186	-
5-*exo*-TS	-986.012504413	0.335155	-608.92
5-*exo*-prod	-986.06022938	0.337923	-

Jamison BF_3

Name	Enthalpy (Hartrees)	Z.P.E (Hartrees)	Frequency (cm^{-1})
6-*endo*-TS	-1119.15860533	0.295683	-540.93
5-*exo*-TS	-1119.1496532	0.295148	-515.21

Section 1.3.1

Tetrahydro-template

Name	Enthalpy (Hartrees)	Z.P.E (Hartrees)	Frequency (cm^{-1})
6-*endo*-TS	-730.7515131	0.300017	-590.33
6-*endo*-Prod	-730.8475898	0.30269	-
5-*exo*-TS	-730.7459184	0.297516	-506.86
5-*exo*-prod	-730.8341608	0.302196	-

Bi-Template

Name	Enthalpy (Hartrees)	Z.P.E (Hartrees)	Frequency (cm^{-1})
6-*endo*-TS	-922.6343354	0.36999	-588.91
6-*endo*-Prod	-922.730676	0.373466	-
5-*exo*-TS	-922.6284033	0.367974	-494.56
5-*exo*-prod	-922.7097741	0.37078	-

1.3.3

Carbon Template

Name	Enthalpy (Hartrees)	Z.P.E (Hartrees)	Frequency (cm^{-1})
6-*endo*-TS	-922.6343354	0.36999	-595.11
6-*endo*-Prod	-922.730676	0.373466	-
5-*exo*-TS	-922.6284033	0.367974	-524.21
5-*exo*-prod	-922.7097741	0.37078	-

1.3.4

Dioxane Template Netural

Name	Enthalpy (Hartrees)	Z.P.E (Hartrees)	Frequency (cm^{-1})
6-*endo*-TS	-766.6405359	0.276392	-580.72
6-*endo*-Prod	-766.7311035	0.277706	-
5-*exo*-TS	-766.6310534	0.281454	-478.76
5-*exo*-prod	-766.7266766	0.278935	-

Dioxane Template Acid

Name	Enthalpy (Hartrees)	Z.P.E (Hartrees)	Frequency (cm^{-1})
6-*endo*-TS	-614.2832602	0.237058	-445.12
6-*endo*-Prod	-614.3204991	0.240581	-
5-*exo*-TS	-614.2816894	0.24	-446.24
5-*exo*-prod	-614.3100545	0.240368	-

1.3.5

Cycloheptane Template

Name	Enthalpy (Hartrees)	Z.P.E (Hartrees)	Frequency (cm^{-1})
6-*endo*-TS	-770.0355553	0.328641	-608.93
6-*endo*-Prod	-770.1346897	0.331393	-
5-*exo*-TS	-770.0356602	0.326056	-556.08
5-*exo*-prod	-770.1188916	0.329588	-

Chapter 2

2.2.1

Bronsted Analysis

Name	Description	Enthalpy (Hartrees)	Z.P.E (Hartrees)	Frequency (cm^{-1})
⟨ HCl	TS	-963.57884871	0.250578	-754.25
⟨ HCl	GS	-963.58031216	0.253143	-
® HCl	TS	-963.578737245	0.250639	-826.13
® HCl	GS	-963.579689678	0.253155	-
⟨ Phosphate	TS	-1146.82964093	0.291721	-924.45
⟨ Phosphate	GS	-1146.84792157	0.296456	-
® Phosphate	TS	-1146.82942158	0.291784	-1019.94
® Phosphate	GS	-1146.84723643	0.296724	-

2.2.2

Tan Model – No Solvent Bridge

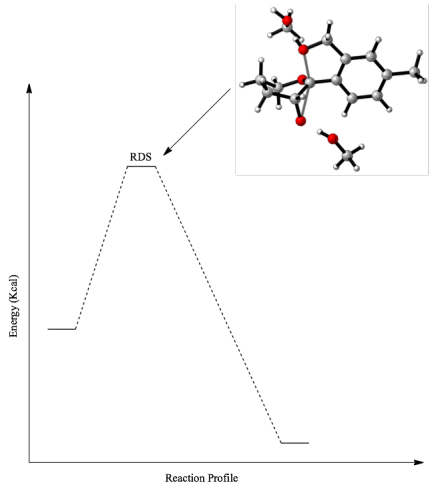

Name	Description	Enthalpy (Hartrees)	Z.P.E (Hartrees)	Frequency (cm^{-1})
R=H	GS	961.7305259	0.382024	-
R=H	TS	-961.697622	0.377778	-101.62
R=OME	GS	-1036.928106	0.386694	-
R=OME	TS	-1036.878826	0.383661	-181.01
R=ME	TS	-961.6957755	0.377778	-180.70
R=ME	GS	-961.7449119	0.382024	-
R=CF_3	TS	-1259.334901	0.355405	-192.29
R=CF_3	GS	-1259.38391	0.358968	-

Tan Model-Solvent Bridge

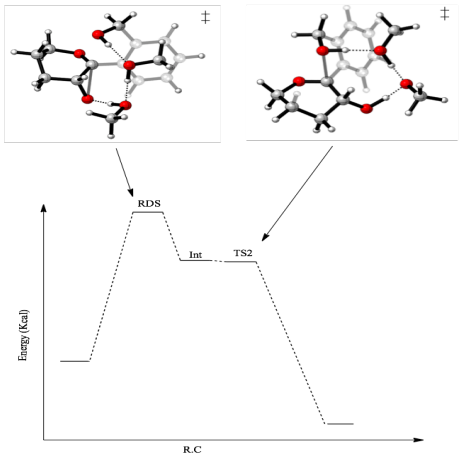

Name	Description	Enthalpy (Hartrees)	Z.P.E (Hartrees)	Frequency (cm^{-1})
R=H	GS	-922.4475884	0.353542	-
R=H	TS	-922.4095459	0.351445	-119.00
R=OME	GS	-1036.92981	0.38649	-
R=OME	TS	-1036.892608	0.384352	-162.22
R=ME	TS	-961.7469713	0.381061	-135.94
R=ME	GS	-961.7092885	0.378995	-
R=CF_3	TS	-1259.386657	0.35883	-104.88
R=CF_3	GS	-1259.347182	0.3564	-

Tan Model-Cyclohexane Model

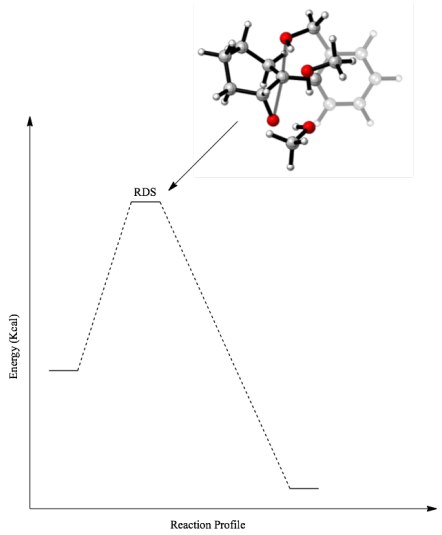

Name	Description	Enthalpy (Hartrees)	Z.P.E (Hartrees)	Frequency (cm^{-1})
Cyclohexane	GS	-886.5287217	0.377561	-
Cyclohexane	TS	-886.4727995	0.375133	-503.21
Cyclohexane	Prod	-886.5491545	0.379988	-

Tan Model- Explicit Solvent Model

Name	Description	Enthalpy (Hartrees)	Z.P.E (Hartrees)	Frequency (cm^{-1})
R=H	GS	-1.354836419	0.84924	-

R=H	TS	-1.341800631	0.848577	-259.29
R=OME	GS	-1.425052232	0.877777	-
R=OME	TS	-1.412904595	0.876664	-261.94
R=Cl	GS	-1.455773516	0.885785	-
R=Cl	TS	-1.442651666	0.884459	-276.58
R=CF_3	GS	-1.613586827	0.855304	-
R=CF_3	TS	-1.59925635	0.854376	-269.69

2.3.1

In this section I use the Carbohydrate nomenclature ⟨ and ® to describe to conformation of the product; ⟨ is anomeric while ® is non-anomeric.

Functional Exploration – TRIP C.P.A Glycal Cyclizaiton

Name	Description	Enthalpy (Hartrees)	Z.P.E (Hartrees)	Frequency (cm^{-1})
⟨ – B97D3	GS	-3464.999248	1.276896	-
⟨ – B97D3	TS	-3464.991094	1.272528	-1184.93
® – B97D3	GS	-3464.999259	1.276744	-
® – B97D3	TS	-3464.98831	1.272076	-1150.87
® – B3LYP	TS	-3466.89934	1.294953	-1119.83
⟨ – B3LYP	TS	-3466.902126	1.294954	-987.23
® – M06L	TS	-3466.379022	1.304161	-1349.60
⟨ – M06L	TS	-3466.378074	1.306077	-1365.89

Single Point Exploration (TZVP basis set) – TRIP C.P.A Glycal Cyclizaiton

Name	Description	Enthalpy (Hartrees)	Z.P.E (Hartrees)
⟨ – B97D3	TS	-3465.880296	1.272528
® – B97D3	TS	-3465.877264	1.272076
® – M06L	TS	-3467.345292	1.304161
⟨ – M06L	TS	-3467.345209	1.306077
® – M062x	TS	-3466.482458	1.304161
⟨ – M062x	TS	-3466.480597	1.306077

Section 2.3.2

S-TRIP Glycal Cyclization

Name	Description	Enthalpy (Hartrees)	Z.P.E (Hartrees)	Frequency (cm^{-1})
⟨ – Acetal	GS	-1682.154671	1.353965	-
⟨ – Acetal	TS	-1682.137932	1.349088	-1365.89
® – Acetal	GS	-1682.165073	1.3549	-
® – Acetal	TS	-1682.137986	1.348938	-1349.60
⟨ – Acetal S.P.C	GS	-3466.503971	-	-

⟨ – Acetal S.P.C	TS	-3466.480597	-	-
® – Acetal S.P.C	GS	-3466.512234	-	-
® – Acetal S.P.C	TS	-3466.482458	-	-

R-TRIP Glycal Cyclization

Name	Description	Enthalpy (Hartrees)	Z.P.E (Hartrees)	Frequency (cm^{-1})
⟨ – Acetal	GS	-1682.152998	1.351785	-
⟨ – Acetal	TS	-1682.136854	1.346796	-1241.67
® – Acetal	GS	-1682.166036	1.352013	-
® – Acetal	TS	-1682.135962	1.347703	-1428.56
⟨ – Acetal S.P.C	GS	-3466.505269	-	-
⟨ – Acetal S.P.C	TS	-3466.482046	-	-
® – Acetal S.P.C	GS	-3466.516454	-	-
® – Acetal S.P.C	TS	-3466.483044	-	-

Section 2.3.2

TRIP (S) Enatioselective Cyclization (Bi-functional Activity)

Name	Description	Enthalpy (Hartrees)	Z.P.E (Hartrees)	Frequency (cm^{-1})
⟨ – S enant.	(Bi) GS	-1762.572669	1.408397	-
⟨ – S enant.	(Bi) TS	-1762.551252	1.402977	-1288.53
® – S enant.	(Bi) GS	-1762.571193	1.408806	-
® – S enant.	(Bi) TS	-1762.549994	1.403654	-1358.46
⟨ – S enant. S.P.C	(Bi) GS	-3546.874415	-	-
⟨ – S enant. S.P.C	(Bi) TS	-3546.851847	-	-
® – S enant. S.P.C	(Bi) GS	-3546.872669	-	-
® – S enant. S.P.C	(Bi) TS	-3546.850113	-	-

TRIP (S) Enatioselective Cyclization (Mono-functional Activity)

Name	Description	Enthalpy (Hartrees)	Z.P.E (Hartrees)	Frequency (cm^{-1})
⟨ – S enant.	(Mono) GS	-1762.572669	1.408397	-
⟨ – S enant.	(Mono) TS	-1762.555615	1.404972	-1339.41
® – S enant.	(Mono) GS	-1762.571193	1.408806	-
® – S enant.	(Mono) TS	-1762.548465	1.403569	-1331.29
⟨ – S enant. S.P.C	(Mono) GS	-3546.874415	-	-
⟨ – S enant. S.P.C	(Mono) TS	-3546.858424	-	-
® – S enant. S.P.C	(Mono) GS	-3546.872669	-	-
® – S enant. S.P.C	(Mono) TS	-3546.848195	-	-

TRIP (R) Enatioselective Cyclization (Bi-functional Activity)

Name	Description	Enthalpy (Hartrees)	Z.P.E (Hartrees)	Frequency (cm^{-1})
⟨ – R enant.	(Bi) GS	-1762.56316	1.409769	-
⟨ – R enant.	(Bi) TS	-1762.551259	1.406096	-1345.31
® – R enant.	(Bi) GS	-1762.570225	1.410186	-
® – R enant.	(Bi) TS	-1762.549998	1.404164	-1345.01
⟨ – R enant. S.P.C	(Bi) GS	-3546.868725	-	-
⟨ – R enant. S.P.C	(Bi) TS	-3546.854367	-	-
® – R enant. S.P.C	(Bi) GS	-3546.874415	-	-
® – R enant. S.P.C	(Bi) TS	-3546.852431	-	-

TRIP (R) Enatioselective Cyclization (Mono-functional Activity)

Name	Description	Enthalpy (Hartrees)	Z.P.E (Hartrees)	Frequency (cm^{-1})
⟨ – R enant.	(Mono) GS	-1762.563399	1.410749	-
⟨ – R enant.	(Mono) TS	-1762.552599	1.40696	-1330.19
® – R enant.	(Mono) GS	-1762.554091	1.411543	-
® – R enant.	(Mono) TS	-1762.545312	1.407759	-1235.01
⟨ – R enant. S.P.C	(Mono) GS	-3546.868725	-	-
⟨ – R enant. S.P.C	(Mono) TS	-3546.856963	-	-
® – R enant. S.P.C	(Mono) GS	-3546.855349	-	-
® – R enant. S.P.C	(Mono) TS	-3546.86582	-	-

Section 2.3.3

Antraquinone (S) Enatioselective Cyclization (Bi-functional Activity)

Name	Description	Enthalpy (Hartrees)	Z.P.E (Hartrees)	Frequency (cm^{-1})
⟨ – S enant.	(Bi) GS	-1762.544047	1.09002	-
⟨ – S enant.	(Bi) TS	-1762.534481	1.086228	-1303.69
® – S enant.	(Bi) GS	-1762.543979	1.090674	-
® – S enant.	(Bi) TS	-1762.534537	1.085981	-1276.69
⟨ – S enant. S.P.C	(Bi) GS	-3453.824459	-	-
⟨ – S enant. S.P.C	(Bi) TS	-3453.811854	-	-
® – S enant. S.P.C	(Bi) GS	-3453.823663	-	-
® – S enant. S.P.C	(Bi) TS	-3453.810425	-	-

Antraquinone (S) Enatioselective Cyclization (Mono-functional Activity)

Name	Description	Enthalpy (Hartrees)	Z.P.E (Hartrees)	Frequency (cm^{-1})
⟨ – S enant.	(Mono) GS	-1762.562023	1.081033	-
⟨ – S enant.	(Mono) TS	-1762.680044	1.086703	-1355.71
® – S enant.	(Mono) GS	-1762.546938	1.091943	-
® – S enant.	(Mono) TS	-1762.534031	1.086287	-1147.29
⟨ – S enant. S.P.C	(Mono) GS	-3453.811853	-	-
⟨ – S enant. S.P.C	(Mono) TS	-3453.811785	-	-
® – S enant. S.P.C	(Mono) GS	-3453.825134	-	-
® – S enant. S.P.C	(Mono) TS	-3453.809754	-	-

Antraquinone (R) Enatioselective Cyclization (Bi-functional Activity)

Name	Description	Enthalpy (Hartrees)	Z.P.E (Hartrees)	Frequency (cm^{-1})
⟨ – R enant.	(Bi) GS	-1762.567819	1.082526	-
⟨ – R enant.	(Bi) TS	-1762.555984	1.077552	-1249.87
® – R enant.	(Bi) GS	-1762.569853	1.082159	-
® – R enant.	(Bi) TS	-1762.555422	1.077495	-1253.92
⟨ – R enant. S.P.C	(Bi) GS	-3453.822023	-	-
⟨ – R enant. S.P.C	(Bi) TS	-3453.802731	-	-
® – R enant. S.P.C	(Bi) GS	-3453.821714	-	-
® – R enant. S.P.C	(Bi) TS	-3453.799547	-	-

Antraquinone (R) Enatioselective Cyclization (Mono-functional Activity)

Name	Description	Enthalpy (Hartrees)	Z.P.E (Hartrees)	Frequency (cm^{-1})
⟨ – R enant.	(Mono) GS	-1762.566139	1.081734	-
⟨ – R enant.	(Mono) TS	-1762.556388	1.078159	-1292.37
® – R enant.	(Mono) GS	-1762.565007	1.082942	-
® – R enant.	(Mono) TS	-1762.556404	1.077897	-1283.30
⟨ – R enant. S.P.C	(Mono) GS	-3453.811853	-	-
⟨ – R enant. S.P.C	(Mono) TS	-3453.803716	-	-
® – R enant. S.P.C	(Mono) GS	-3453.813602	-	-
® – R enant. S.P.C	(Mono) TS	-3453.803214	-	-

Chapter 3

3.2.1

(S)-TRIP Benzoic Desymmerization

Name	Description	Enthalpy (Hartrees)	Z.P.E (Hartrees)	Frequency (cm^{-1})
R-Pathway	TS	-1527.765706	1.275315	-568.20
R-Pathway	GS	-1527.794773	1.277605	-
S-Pathway	TS	-1527.766988	1.275156	-539.32
S-Pathway	GS	-1527.794608	1.277528	-

3.2.2

(S)-Custom Benzoic Desymmerization

Name	Description	Enthalpy (Hartrees)	Z.P.E (Hartrees)	Frequency (cm^{-1})
R-Pathway	TS	-1527.57172522	1.309391	-542.72
R-Pathway	GS	-1527.5994509	1.31142	-
S-Pathway	TS	-1527.56888415	1.309268	-563.63
S-Pathway	GS	-1527.59974291	1.311942	-

3.2.3

(S)-TRIP Bronsted Analysis

Name (OMe)	Description	Enthalpy (Hartrees)	Z.P.E (Hartrees)	Frequency (cm^{-1})
R-Pathway	TS	-1642.251705	1.308668	-551.44
R-Pathway	GS	-1642.280565	1.311036	-
S-Pathway	TS	-1642.248852	1.308877	-554.83
S-Pathway	GS	-1642.279895	1.310441	-

Name (CF_3)	Description	Enthalpy (Hartrees)	Z.P.E (Hartrees)	Frequency (cm^{-1})
R-Pathway	TS	-1864.706121	1.280511	-551.41
R-Pathway	GS	-1864.735566	1.282545	-
S-Pathway	TS	-1864.703284	1.280814	-557.48
S-Pathway	GS	-1864.735539	1.282923	-

3.3.1

(R)-TRIP promoted resolution Functional Screen

Name	Description	Enthalpy (Hartrees)	Z.P.E (Hartrees)	Frequency (cm^{-1})
R-Pathway	TS	-1850.70222145	1.269473	-550.53
R-Pathway	GS	-1850.73244846	1.273051	-
S-Pathway	TS	-1850.70897496	1.270416	-490.67
S-Pathway	GS	-1850.7352285	1.272851	-

3.3.2

(R)-H^8 Custom List Thiobenzoate desymmerization

Name	Description	Enthalpy (Hartrees)	Z.P.E (Hartrees)	Frequency (cm^{-1})
R-Pathway	TS	-1850.55460825	1.397108	-516.98
R-Pathway	GS	-1850.57858303	1.398694	-
S-Pathway	TS	-1850.55855518	1.39728	-530.69
S-Pathway	GS	-1850.58698929	1.399998	-

3.4.1

(R)-TRIP N-Activation Course

Name	Description	Enthalpy (Hartrees)	Z.P.E (Hartrees)	Frequency (cm^{-1})
R-Pathway	TS	-1852.1760715	1.379533	-440.26
R-Pathway	GS	-1852.19595674	1.380293	-
S-Pathway	TS	-1852.17437112	1.379134	-493.27
S-Pathway	GS	-1852.19863353	1.380792	-

(R)-TRIP O-Activation Course

Name	Description	Enthalpy (Hartrees)	Z.P.E (Hartrees)	Frequency (cm^{-1})
R-Pathway	TS	-2056.580673	1.379569	-353.49
R-Pathway	GS	-2056.61410014	1.384722	-
S-Pathway	TS	-2056.58846348	1.380751	-441.5
S-Pathway	GS	-2056.61852742	1.384771	-